Spring 5-15-2023

Using In Situ Single-Particle Imaging to Understand the Role of Structural Distortions during Anion Exchange in Cesium Lead Halide Perovskite Nanocrystals

Dongyan Zhang

WASHINGTON UNIVERSITY IN ST. LOUIS

Department of Chemistry

Dissertation Examination Committee:
William E. Buhro, Chair
Bryce F. Sadtler, Co-Chair
Joseph A. Fournier
Richard A. Loomis
Rohan Mishra

Using In Situ Single-Particle Imaging to Understand the Role of Structural Distortions during Anion Exchange in Cesium Lead Halide Perovskite Nanocrystals

by

Dongyan Zhang

A dissertation presented to
Washington University in St. Louis
in partial fulfillment of the
requirements for the degree
of Doctor of Philosophy

May 2023
St. Louis, Missouri

Table of Contents

List of Figures iv

List of Tables vi

Acknowledgments vii

Abstract of the Dissertation viii

Chapter 1: Introduction 1

1.1 Overview 1

1.2 Lead Halide Perovskite Semiconductors 7

1.2.1 Crystal Structure 7

1.2.2 Properties and Applications of Lead Halide Perovskites 9

1.3 Size Effects in Semiconductor Nanocrystals 11

1.4 Single-Particle Fluorescence Microscopy 14

1.5 Dissertation Outline 17

1.6 References 18

Chapter 2: Irreversibility in Anion Exchange Between Cesium Lead Bromide and Iodide Nanocrystals Imaged by Single-Particle Fluorescence 21

2.1 Introduction 22

2.2 Experimental 25

2.3 Results 33

2.4 Model for asymmetry in anion exchange 47

2.5 Conclusions 54

2.6 Appendix A 55

2.6.1 Tables 55

2.6.2 Figures 61

2.7 References 81

Chapter 3: Size-Dependent Miscibility Controls the Kinetics of Anion Exchange in Cesium Lead Halide Nanocrystals 86

3.1 Introduction 87

3.2 Experimental 91

3.3 Results 101

3.4 Model for size-dependent reactivity 110
3.5 Conclusions 113
3.6 Appendix B 114
3.6.1 Tables 114
3.6.2 Figures 115
3.7 References 127
Chapter 4: Conclusions and Perspectives 133
4.1 Conclusions 133
4.2 Perspectives 135
4.3 References 137

List of Figures

Figure 1.1: Scheme of excitation and recombination 3
Figure 1.2: Crystal structure of $CsPbBr_3$ 7
Figure 2.1: PL spectra during anion exchange of $CsPbBr_3$ NCs to $CsPbI_3$ 34
Figure 2.2: Schemes and snapshots showing transformation of $CsPbX_3$ NCs 39
Figure 2.3: Fluorescence intensity trajectories for $CsPbX_3$ NCs undergoing anion exchange.....40
Figure 2.4: Experimental mean waiting and switching times for anion exchange 43
Figure 2.5: Change in free energy and probability with the number of exchange events 49
Figure 2.6: Time evolution PL spectra of $CsPbI_3$ NCs adding TBAB 61
Figure 2.7: TEM images of $CsPbX_3$ NCs before and after anion exchange.....62
Figure 2.8: Size distributions of $CsPbX_3$ NCs shown in **Figure 2.7** 63
Figure 2.9: XRD patterns of $CsPbX_3$ NCs before and after anion exchange 65
Figure 2.10: Comparison between experimental XRD patterns with simulated patterns.....66
Figure 2.11: Normalized PL spectra of different batches of $CsPbBr_3$ and $CsPbI_3$ NCs.....67
Figure 2.12: Comparison of the mean value and the FWHM of single-NC waiting times 68
Figure 2.13: Waiting and switching time as a function of particle position 69
Figure 2.14: Comparison of the ensemble rise times to the mean single-NC switching times 70
Figure 2.15: Representative trajectories and intermittency histograms of single particles 71
Figure 2.16: Representative trajectories and intermittency histograms of clusters 72
Figure 2.17: Histograms of waiting times of $CsPbBr_3$ NCs to $CsPbI_3$ 73
Figure 2.18: Histograms of waiting times of iodide-rich $CsPbBr_{3-x}I_x$ NCs to $CsPbBr_3$.....74
Figure 2.19: Histograms of waiting times of $CsPbI_3$ NCs to $CsPbBr_3$ 75
Figure 2.20: Histograms of waiting times of bromide-rich $CsPbBr_{3-x}I_x$ NCs to $CsPbI_3$ 76
Figure 2.21: Gaussian fits to the distribution of waiting times.....77
Figure 2.22: Simulated ensemble and single-particle trajectories 78
Figure 2.23: Plot of the waiting time vs. switching time for individual particles.....79
Figure 2.24: The slopes from linear fits to scatter plots shown in **Figure 2.23**.....80
Figure 3.1: TEM images of $CsPbBr_3$ NCs with different sizes 102
Figure 3.2: PL spectra of $CsPbBr_3$ NCs showing size dependence 104
Figure 3.3: Scheme and snapshots showing transformation of $CsPbBr_3$ NCs.....106
Figure 3.4: Representative single-particle fluorescence trajectories during anion exchange.....107
Figure 3.5: Comparison of experimental and simulated switching times.....109
Figure 3.6: Size distributions of the $CsPbBr_3$ NCs shown in **Figure 3.1** 115
Figure 3.7: UV-Vis absorption spectra of $CsPbBr_3$ NCs showing size dependence 116
Figure 3.8: XRD patterns of $CsPbBr_3$ NCs with different sizes.....117
Figure 3.9: Titration PL spectra of $CsPbBr_3$ NCs with different sizes 118
Figure 3.10: Transmittance spectra of filter sets.....119
Figure 3.11: Representative trajectories and intermittency histograms of single particles 120
Figure 3.12: Representative trajectories and intermittency histograms of clusters 121

Figure 3.13: Representative switching times as a function of NC position.....122
Figure 3.14: Expanded **Figure 3.5(a)** at low TMSI concentrations 123
Figure 3.15: Simulated ΔG_i and probability with varied number of exchange events 124
Figure 3.16: Simulated ensemble and single-particle trajectories 125
Figure 3.17: Simulated switching time for different δ and k_0.....126

List of Tables

Table 2.1: Additional details for the fluorescence spectra shown in **Figure 2.1(a)**.....55
Table 2.2: Additional details for the fluorescence spectra shown in **Figure 2.1(b)**.....56
Table 2.3: The $CsPbBr_3$ and $CsPbI_3$ NCs samples characterized in figures.....57
Table 2.4: Fitting parameters for the curves shown in **Figure 2.4**.....58
Table 2.5: Parameters for the linear fits shown in **Figure 2.23**.....59
Table 2.6: Tilt angles for PbX_6 octahedra based on the bulk crystal structures.....60
Table 3.1: Maximum in the PL spectra and FHWM for $CsPbBr_3$ NCs with different sizes.....114

Acknowledgments

I feel grateful when I come so far in my PhD career with the support of so many people. I would like to give special thanks to them.

First, I would like to thank my advisor, Prof. Bryce Sadtler. In the past five years, I learnt a lot from him, not only scientific skills, but also useful experience in communication, writing and being a good scientist. I appreciate his help and advice, which lead to my progress in my research and career.

I would like to thank my colleagues in Sadtler group. Dr. Dong Wang gave me support and worked with me when I stepped in a new field of research. Dr. Meikun Shen guided me with a lot of useful suggestions since the day I joined the group. Xinyi (Sarah) Wu worked with me in my last project; she put much effort in research, and I learnt plenty of new ideas from her. Dr. Bo Yin and Jiang Luo helped me to characterize samples and shared their research experience with me. Dr. Che Tan and Dr. Chu Qin gave me helpful suggestions in career progress and job search. I also want to give my thanks to William Rackers, Ashlynn Berry, and other undergraduate students had a good time with me in our lab.

I would like to thank Chemistry Department, Art & Science School and Washington University to provide all resources for graduated students.

I would like to thank my parents, my girlfriend and my entire family for their strong support and love to me.

My research in doctoral program is supported by National Science Foundation.

Dongyan Zhang

Washington University in St. Louis

May 2023

ABSTRACT OF THE DISSERTATION

Using In Situ Single-Particle Imaging to Understand the Role of Structural Distortions during Anion Exchange of Cesium Lead Halide Perovskite Nanocrystals

by

Dongyan Zhang

Doctor of Philosophy in Chemistry

Washington University in St. Louis, 2023

William E. Buhro, Chair

Bryce F. Sadtler, Co-Chair

Joseph A. Fournier

Richard A. Loomis

Rohan Mishra

Colloidal cesium lead halide ($CsPbX_3$, X = Cl, Br, I) perovskite nanocrystals are being investigated as promising materials for light-emitting devices and fluorescence probes due to their strong absorption and emission (1.55 eV – 3.05 eV) of visible light. Anion exchange is a facile, post-synthetic method to tune the bandgap emission of $CsPbX_3$ nanocrystals, covering most of the spectrum of visible light. However, structural heterogeneities in nanocrystals formed during anion exchange will lead to lower photoluminescence quantum yield and a broader range of emission wavelengths. A single batch of nanocrystals will contain a distribution of sizes, shapes, surface structures, and defect concentrations. These variations will lead to heterogenous reactivity during chemical transformations such as anion exchange. To enhance the brightness and color purity of

light-emitting devices that incorporate $CsPbX_3$ nanocrystals, the factors that control heterogeneous reactivity need to be understood.

In this dissertation, we performed research on anion exchange between $CsPbBr_3$ and $CsPbI_3$ nanocrystals using in situ single-particle fluorescence imaging. This method can probe differences in the reactivity of hundreds of nanocrystals undergoing anion exchange at the same time. As the emission from each nanocrystal shifts to longer wavelengths during anion exchange, they turn on and appear as bright spots during the fluorescence video, which indicates their transformation. By analyzing different single-particle reaction trajectories, we assign a switching time, which is a measure of the time it takes the nanocrystal to complete anion exchange. For the transformation of $CsPbBr_3$ nanocrystals to $CsPbI_3$, the average switching time of individual nanocrystals is longer than the reverse transformation of $CsPbI_3$ nanocrystals to $CsPbBr_3$. To understand the kinetics during anion exchange, we performed experiments using different concentrations of substitutional halide anions. We observed a stronger concentration dependence in the average switching times for the forward reaction of $CsPbBr_3$ nanocrystals to $CsPbI_3$ than in the reverse reaction (i.e., $CsPbI_3$ to $CsPbBr_3$). We developed different models using Monte Carlo simulations to rationalize the experimental results. We attribute the difference in switching times to a more abrupt change in structure for the transformation of $CsPbI_3$ nanocrystals to $CsPbBr_3$, arising from a larger change in the tilting angle of PbX_6 octahedra. These results indicate that $CsPbI_3$ nanocrystals synthesized by the hot injection method have a different structure than $CsPbI_3$ nanocrystals synthesized by anion exchange.

We also studied the size dependence of anion exchange from $CsPbBr_3$ nanocrystals to $CsPbI_3$ using single-particle imaging. We observed a longer average reaction time and a stronger dependence of the average switching time on the concentration of substitutional halide anions for

smaller nanocrystals (< 8 nm), compared to nanocrystals with a larger size (> 8 nm). Comparison to ensemble fluorescence spectroscopy indicates we are probing a critical stage of the reaction after anion exchange has initiated on the surface of the nanocrystals. We developed different kinetic models using Monte Carlo simulations to understand this size-dependent reactivity. We attribute the size dependence to a larger structural reorganization that must occur in larger nanocrystals during anion exchange, which leads to a more abrupt transformation compared with smaller nanocrystals. Our results indicate that size-dependent miscibility between $CsPbBr_3$ and $CsPbI_3$ at the nanoscale controls the reaction kinetics. Smaller nanocrystals maintain a homogenous structure during the entire transformation. As the nanocrystal size increases, variations in the tilting patterns of PbX_6 octahedra in the perovskite crystals lead to different structures for $CsPbBr_3$ and $CsPbI_3$. Thus, a new iodide-rich phase must first nucleate within larger $CsPbBr_3$ nanocrystals, which is then followed by their rapid transformation. Cumulatively, these results indicate that there are intrinsic variations in the reactivity of nanocrystals undergoing the same transformation. This heterogeneity imposes a limit on the narrowness of emission wavelengths for $CsPbX_3$ nanocrystals prepared by anion exchange. Synthetic methods that maintain a high and uniform concentration of substitutional halide anions during anion exchange will minimize variations in the composition and will maximize the color purity of the resulting $CsPbX_3$ nanocrystals for applications in light-emitting devices.

Chapter 1: Introduction

1.1 Overview

The energy crisis has become a worldwide challenge in recent decades along with the environmental issues that come with the usage of nonrenewable fossil fuels. While alternative renewable energy sources are being developed, such as solar and wind energy, non-renewable fossil fuels still make up 80% of the total worldwide energy supply.[1] Besides waiting for a breakthrough in new energy, reducing energy consumption is another important component in minimizing the emission of greenhouse gases. Illumination occupies 15% of global electric power consumption and produces 5% of greenhouse gas emissions.[2] One solution to reduce electricity use is to replace incandescent lightbulbs with energy-saving light-emitting diodes (LED) in millions of homes and public buildings. LED lights exhibit much higher luminous efficacy (up to 223 lumens/W) and longer lifetime (10000 – 25000 hours), compared to traditional incandescent lights (10–17 lumens/W, 1000 - 2000 hours).[3] A higher portion of efficient lighting will lead to more energy saving. Thus, basic science research is needed to increase the emission efficiency of the next generation of LEDs.

Semiconductors are the active material responsible for emitting light in LED devices. In order to identify and develop new semiconductors for these devices, it is important to understand the basic properties of semiconductors. Semiconductors are materials that possess electrical conductivities that are intermediate between that of conductors and insulators. The conductivity of different crystalline solids depends on their electronic structure. For single isolated atoms, electrons occupy atomic orbitals. When atoms form molecules, the orbitals from each atom will interact and hybridize to form new molecular orbitals that are delocalized over the molecule; these

molecular orbitals create new energy states in which the electrons occupy. In a crystalline solid the number of atoms is very large (i.e., on the order 6.02×10^{23} atoms). In this case the spacing between energy states is so small that the distribution of energies can be approximated as a continuum, which is referred to as an energy band. The Fermi-Dirac distribution, $f(\varepsilon)$, gives the probability that a state with a certain energy ε will be occupied by an electron:

$$f(\varepsilon) = \frac{1}{e^{(\varepsilon - \mu)/k_B T} + 1} \tag{1.1}$$

Where T is the absolute temperature, and k_B is the Boltzmann constant. The Fermi level (μ) is the energy state that has a 50% probability of being occupied by an electron ($\varepsilon = \mu$).

Conductors like metals, have a partially filled energy band, and the Fermi level lies within the band. This leads to a high density of electronic states near the Fermi level. In contrast, the Fermi level in semiconductors and insulators falls in between two different energy bands (at $T = 0\ K$). The valence band is completely filled at $T = 0\ K$ while the conduction band is empty. The energy gap between the conduction band and valence bands is called the bandgap. In an ideal semiconductor or insulator, there are no electronic states in the bandgap where the Fermi level resides. The bandgap energy is large for insulators (usually > 5 eV) but smaller for semiconductors (0.2 to 3.5 eV). The orbital interaction for different semiconductors will depend on the valence atomic orbitals used in bonding and the crystalline structure. While detailed calculations of band structure are beyond the scope of this thesis, these factors will affect the band structure of different semiconductor materials, leading to different bandgaps. Thus, it is of significant interest to identify and develop semiconductors of a specific bandgap and band structure for the desired application. For LEDs, semiconductors with band gaps between 1.77 eV and 3.26 eV enable the emission of visible light.

With an energy input (e.g., heat, light, electricity, etc.) that is greater than the bandgap of a semiconductor, it is possible to excite electrons from the valence band (VB) to the conduction band (CB). This process makes the semiconductor more conductive as the electrons are now in an electronic state with higher mobility. Furthermore, holes are left in the VB (i.e., the absence of an electron in the valence band), that also act as mobile charge carriers. Electrons will remain in an excited state for a finite period of time; they will eventually recombine with holes to release energy in the form or heat or light, or they can be extracted through an external circuit to generate electricity. Under an external electrical bias, electrons can be injected into a semiconductor; when electrons recombine with holes, this process can release energy in the form of light, which is electroluminescence (EL). The emission wavelength of EL is determined by the bandgap of the semiconductor.

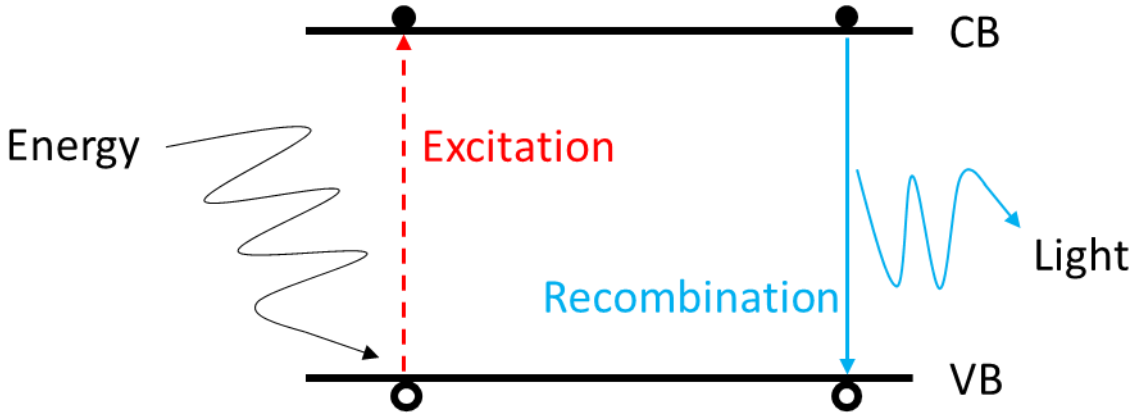

Figure 1.1. Schematic of the excitation (red arrow) of electrons (solid circles) from the valence band (VB) to the conduction band (CB) with an energy input that is greater than the bandgap energy. This process leaves a hole (hollow circle) in the valence band. Schematic showing the radiative recombination of electrons and holes (blue arrow) with the emission of a photon.

Trace amounts of impurity atoms containing a different number of valence electrons relative to that of the host semiconductor can significantly alter the resulting electrical conductivity of the semiconductor. The process of intentionally adding controlled amounts of these impurities is known as doping. Pure semiconductors without dopants are called intrinsic semiconductors; in this case the number of excited electrons (n) and the number of holes (p) are equal (n = p). Semiconductors with dopants are called extrinsic semiconductors, including n-type and p-type semiconductors. Specifically, n-type semiconductors are produced by doping with an electron donor, while p-type semiconductors are produced by doping with an electron acceptor. Both n-type and p-type doping increase the conductivity of the semiconductor. When an n-type semiconductor is connected to a p-type semiconductor, the interface between them is called p-n junction. Current can only easily pass through the p-n junction in one direction, where it flows from the p-type semiconductor to the n-type semiconductor. P-n junctions are the fundamental component of a diode used in most semiconductor devices, like transistors and LEDs.

LED devices are designed based on their EL properties. In the 1960s, early LED devices were constructed with gallium arsenide, GaAs. Limited by its small bandgap (1.4 eV), GaAs LEDs only emit near-infrared light. Later, ternary gallium arsenide phosphide, GaAsP, was used in LEDs; because of its larger bandgap, this semiconductor emits red light.[4] However, these LED lights were not bright enough to illuminate a large area. They were first used in indicators as an early commercial application of LED lights. Since the 1970s, the fabrication process has been improved through better control of crystal growth and assembly of the devices. The emitted light intensity of LEDs increased to the level that was sufficient for illumination, but the commercial application in displays was still limited to semiconductors with small bandgaps, which only emitted red,

orange, yellow and green light.[4] In the 1980s, blue-violet LEDs were first made using Mg-doped GaN, followed by Zn-doped GaN, InGaN, and SiC. Finally, full-color and white LED lights joined the family of light emitting.[4] Along with the improvement in brightness, semiconductors LEDs have been broadly used in displays and lamps. In recent ten years, lead halide perovskite semiconductors have become a promising material for LEDs, thanks to their high EL quantum yield (QY, i.e., the ratio of the number of photons emitted to the number of photons absorbed or electrons injected) and facile preparation methods that produce materials with low defects. More importantly, the development of nanoscale materials like semiconductor nanocrystals (NCs) helps us to miniaturize LED components for better use in flexible and portable electronic devices.

Besides an electric field, incident light with a photon energy higher than the bandgap of the semiconductor can excite electrons to the conduction band. Excited electrons can radiatively recombine with holes in the valence band to emit light. This process is called photoluminescence (PL). Both EL and PL contribute to the broad application of semiconductors as light emitters like LED lights, quantum dot LED (QLED) displays, photosensitive detectors, and biosensors. Higher quantum yield and electron to photon conversion efficiency (EPCE) of semiconductors lead to better energy efficiency in illumination. After decades of development, semiconductor NCs with different compositions can be easily produced with high uniformity in size and morphology at low cost.[5] This material is promising in light-emitting field now and in the future.

However, in real cases, not all excited electrons will relax radiatively leading to photon emission. Traps may be their destination, which consist of impurities or imperfections of the semiconductor lattice. Electrons or holes could be captured by trap states whose energies typically fall within the bandgap of the semiconductor; this process promotes non-radiative recombination where the electrons and holes recombine to produce heat rather than light. Thus, a better control

of semiconductor NC synthesis and assembly is desired to reduce the density of trap states in the semiconductor.

Additionally, the application of semiconductors in indicators and display devices requires monochromaticity in emission (i.e., emission of a narrow range of wavelengths). Compared to bulk semiconductors, semiconductor NCs show a narrower emission wavelength range and higher color purity. Especially, $CsPbX_3$ NCs are promising materials for use in solid-state lighting, and anion exchange is a facile method to tune the bandgap emission.[6, 7] Anion exchange at the ensemble level has been studied in recent years; the control of emission wavelength using a known amount of substitutional anions is understood.[6, 8, 9] However, the mechanism of this reaction and how NCs behave during anion exchange is not clear. For example, compared with pure NCs, mixed-halide perovskite NCs with a special ratio of halide anions exhibit a dark state where the emission is quenched.[10] Understanding the mechanism is the key to control heterogeneity in the composition and structure of NCs produced by anion exchange. Homogeneous $CsPbX_3$ NCs exhibit better performance with higher color purity and QY. The projects in this thesis will focus on studying the mechanism of anion exchange in $CsPbX_3$ NCs with in situ single-particle imaging.

1.2 Lead Halide Perovskite Semiconductors

1.2.1 Crystal Structure

The group of materials with same crystal structure as $CaTiO_3$ are referred to as perovskites. For the general formula of a perovskite, ABX_3, the A sites and B sites are occupied by cations while the X sites are occupied by an anion. The A site and B site have coordination numbers of 12 and 6 by the anions, respectively. Each B-site cation is coordinated by 6 nearest neighbor X-site anions to form a BX_6 octahedron. The BX_6 octahedra connect at their corners by sharing an X-site anion. The A-site cation is surrounded by 8 BX_6 octahedra. Based on these coordination geometries, there is an ideal ratio between the A–X and B–X bond lengths as described further below. For example, in lead halide perovskites, the B-site is occupied by a Pb^{2+} cation, and the X-site is occupied by a halide anion (Cl^-, Br^-, I^-). Cations with appropriate size to occupy the A-site in lead halide perovskites include $CH_3NH_3^+$ and Cs^+ (**Figure 1.2)**.

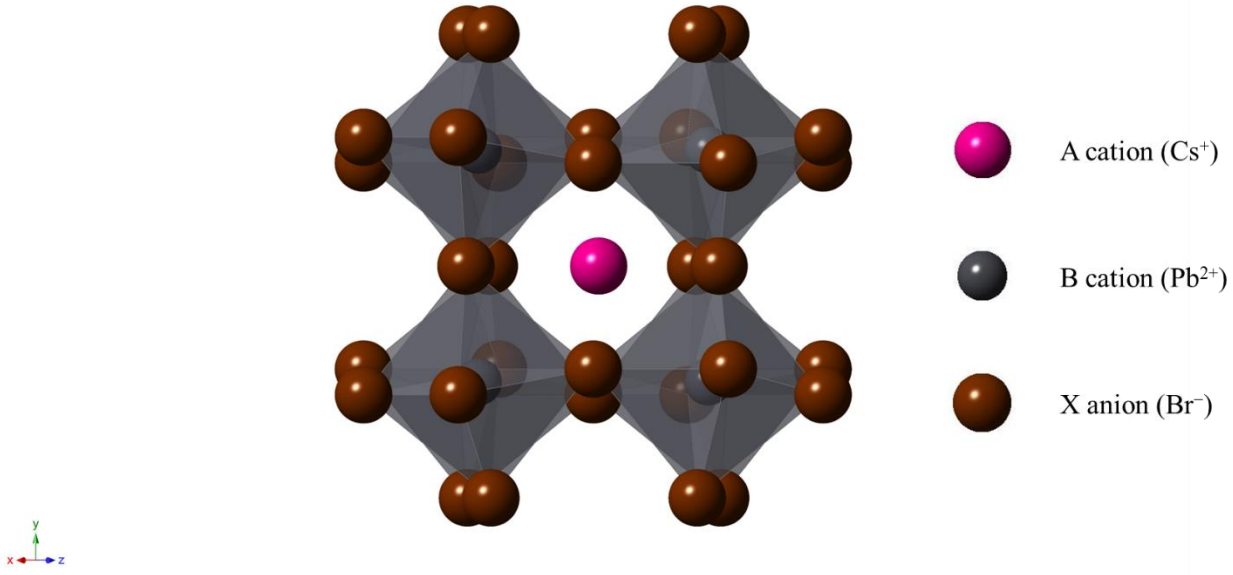

Figure 1.2. Crystal structure of $CsPbBr_3$ with the orthorhombic perovskite phase.

The ideal perovskite structure has a cubic unit cell. However, there will be distortions in the connectivity of the BX_6 octahedra when the radii of the cations do not produce the ideal ratios of A–X and B–X bond lengths. Thus, other structures including tetragonal and orthorhombic occur in perovskite compounds. To determine the structure that a compound with a given composition can form, we can calculate the tolerance factor based on the radii of the ions and the following equation:

$$t = \frac{R_A + R_X}{\sqrt{2}\,(R_B + R_X)} \tag{1.2}$$

where t is the Goldschmidt tolerance factor, and R_A, R_B, and R_X are the ionic radii of the A, B, and X site elements, respectively. Compounds with a tolerance factor between 0.9 and 1 tend to form cubic structures. The crystal structures are hexagonal or tetragonal when $t > 1$ and orthorhombic or rhombohedral when $0.71 < t < 0.9$. Non-perovskite structures can form when $t < 0.71$.

The most well-known compounds in the lead halide perovskite group are methylammonium lead halides ($CH_3NH_3PbX_3$) and cesium lead halides ($CsPbX_3$). The X-site can be occupied by chloride (Cl^-), bromide (Br^-), or iodide (I^-) anions or a mixture of them. Fluoride (F^-) is not commonly observed to be incorporated into the perovskite structure due to its high electronegativity and relatively small size. $CH_3NH_3^+$, Cs^+ and Pb^{2+} cations can form a rigid cation lattice while halide anions can easily move in the crystal without structural collapse.

In the research that is discussed in this thesis dissertation, $CsPbX_3$ is the major semiconductor to be studied. Thus, $CsPbX_3$ perovskites will be used as the primary example in this Introduction. There are three common phases for $CsPbX_3$ crystals, the cubic phase (α), orthorhombic phase (γ) and non-perovskite phase (δ). The non-perovskite phase does not emit in the visible light range

and its formation is generally undesirable. In this thesis dissertation, only the cubic and orthorhombic phases are used for further research.

1.2.2 Properties and Applications of Lead Halide Perovskites

Lead halide perovskite semiconductors show strong absorption and emission in the visible light range (380 nm – 700 nm or 3.26 eV – 1.77 eV) due to their suitable bandgap energies (1.55 eV – 3.05 eV).[6, 7, 9, 11-13] Both $CH_3NH_3PbX_3$ and $CsPbX_3$ semiconductors are broadly being developed for applications in solar cells, light-emitting devices, and fluorescent sensors. Because $CH_3NH_3PbI_3$ and $CsPbI_3$ can absorb almost all visible light, they have been used as the light absorber in lab-scale solar cells, thanks to the relatively low bandgap energy of these materials.[14, 15] The photon to electron conversion efficiency is high in these materials. This high efficiency is due to the long diffusion distances and high diffusion rates of photoexcited charge carriers, which increases the probability that charge carriers are transferred to the transport layer. With these advantages, lead halide perovskites have evolved as a promising class of materials for the solar cell and energy harvesting industry.

Lead halide perovskites also play an important role in the field of new light emitters. The narrow emission linewidths of $CsPbX_3$ makes it possible to construct LED lights with high color purity. The facile synthesis of $CsPbX_3$ semiconductors lowers the cost and energy intensity of their production. Some well-developed semiconductor materials, such as GaN, InP, SiC, require high temperatures (> 1000°C) in their production.[4] In traditional semiconductor manufacturing, each semiconductor material requires its own fabrication line. Compared to traditional semiconductor fabrication, $CsPbX_3$ can be produced under mild conditions (< 200°C) using solution-phase synthesis.[11] Furthermore, the anions within the $CsPbX_3$ semiconductor lattice can be switched after

synthesis through anion exchange to tune the bandgap and obtain a desired emission wavelength.[6, 12] Thus, anion exchange could enable a single fabrication line to produce semiconductors with a variety of different band gaps. By controlling the ratio of halide anions, the emission of $CsPbX_3$ can cover the full spectrum of visible light, making it a good material for light emitting displays. Additionally, the high EL QY of $CsPbX_3$ leads to high luminous efficacy when used in LED lights.

$CsPbX_3$ nanocrystals or quantum dots exhibit a high PL QY for fluorescence emission. In chemical or biological diagnosis of laboratorial tests, $CsPbX_3$ NCs are often used as tracer agent.[16] When the quantum dots are dispersed in the object being diagnosed, a certain type of chemical analyte (like H_2S) can react with $CsPbBr_3$ NCs to quench the fluorescence.[17] From the change in intensity emission, we can distinguish where the reaction occurs within the system. Besides the application as a probe, fluorescence makes $CsPbX_3$ useful to detect changes in the composition and structural of the nanocrystals in themselves during a reaction. For example, the defect concentration varies with the extent of anion exchange during this chemical transformation.[10] Fluorescence is quenched more significantly if more defects are formed that act as traps to capture electrons or holes. By analyzing the intermittency of emission from single NCs, the role of defects and how their concentration changes with ratio of halide anions can be elucidated.

1.3 Size Effects in Semiconductor Nanocrystals

Size effects on chemical reactions and physical properties have been studied hundreds of years, from bulk materials to nanomaterials. NCs show intrinsic differences during chemical reactions compared to their bulk counterparts, due to their significantly higher surface-to-volume ratios.[18-23] Therefore, nanoscale catalysts typically show higher activity for chemical transformations than bulk catalysts.

Semiconductors with nanoscale dimensions also exhibit size-dependent electronic structures. The Bohr exciton radius is the distance between an electron and a hole in an exciton. When the size of a semiconductor crystal approaches the Bohr exciton radius, quantum confinement is observed as the density of states near the band edges become more discrete. Quantum confinement has a more significant effect when the size is smaller than the Bohr radius. The bandgap energy increases with decreasing size due to quantum confinement, leading to a blueshift in both the absorption and emission of the semiconductor NCs. In fluorescent nanocrystals such as CdSe and $CsPbX_3$ NCs, the emission wavelength is determined by the crystal size; a broad emission peak will be observed for a population of NCs with a large size distribution and vice versa.

The phase diagram for a bulk material depicts the phases in thermodynamic equilibrium as a function of composition, temperature, and pressure. Structures and phases that do not appear in the bulk phase diagram may be stabilized at the nanoscale due to the contribution of surface energy to the total energy of the crystal.[24-27] As the size of a crystal decreases, the surface to volume ratio increases, and the contribution of the surface energy to the total free energy of the crystal increases. The surface structure of nanoscale crystals can change the relative stability of different phases due to different exposed facets with different atomic arrangements and bonding geometries. For example, the tolerance factor has been used broadly to predict the structure of bulk perovskites,

but the structure can be different in NCs. $CsPbCl_3$, $CsPbBr_3$ and $CsPbI_3$ are all predicted to form the orthorhombic perovskite structure in bulk based on their tolerance factors of 0.870, 0.862 and 0.851, respectively. However, the surface energy stabilizes the cubic structure of $CsPbX_3$ NCs for sizes near 5 nm. Therefore, the effect of particle size on crystal structure has been studied in recent years to understand the relationship between surface energy and phase stability.[26-28]

The microscopic pathway of a phase transition between the different regions of a phase diagram greatly depends on the dynamics of nucleating a new phase. Such dynamics can be hidden during the transformation of bulk solids because the bulk material contains numerous individual domains which undergo the phase change simultaneously. On the other hand, phase transitions in NCs can occur through a single nucleation and growth event. This means that by studying phase transitions in NCs, we may find information that is hidden in bulk crystals.

The pressure-induced phase transition of CdSe NCs from the wurtzite to rock salt phase has provided important insights into how nanocrystals size affects the thermodynamics and kinetics of phase transformations at the nanoscale.[24, 29] A hysteresis or difference in the forward and backward pressures needed to induce the phase transition between the wurtzite and rock salt phases has been reported in CdSe NCs. The width of the hysteresis loop for the phase transition in CdSe NCs is significantly larger than that observed for bulk CdSe, indicating that the kinetics are different for crystals of finite size. In bulk CdSe, the phase transition will occur at a fixed temperature and pressure. However, the phase transition point changes with size in NCs. The reason is that the extra energy required to stabilize or destabilize nucleation of the newly formed new phase (interior heterogeneities) in the original NCs serves as an energy barrier inhibiting the phase transition. Based on the microscopic pathway, the phase transition leads to rock salt surfaces with a higher energy than the wurtzite surfaces of the initial NCs. If ligands and solvent effects are excluded due

to same chemical environment in all experiments, the surface energy fraction of the total free energy increases as size decreases. Thus, a higher pressure is needed for smaller CdSe NCs to make phase transition from wurtzite to rock salt. Inspired by these previous works, we may consider the size dependence of surface energies and its effect on the chemical transformation of $CsPbX_3$ NCs during anion exchange.

The fast diffusion of halide anions in $CsPbX_3$ NCs combined with their high surface areas facilitates exchange between anions in solution and anions in the crystal lattice. Previous reports have shown that colloidal $CsPbX_3$ NCs can transform to mixed-halide NCs in seconds to minutes at room temperature by adding substitutional halide ions to the colloidal solution of nanocrystals.[6, 8, 12, 30] By controlling the concentration of substitutional anions, NCs with different ratios of mixed halides can be produced by anion exchange. In combination with quantum confinement effects, control over the halide composition through post-synthetic anion exchange provides a method to tune the band gap and emission wavelength of $CsPbX_3$ NCs. Similar to the pressure-induced transformation of CdSe NCs, we hypothesized that this chemical transformation of $CsPbX_3$ NCs would exhibit size-dependent kinetics. However, because a given batch of NCs will possess a distribution of sizes, methods to analyze the kinetics of anion exchange in single nanocrystals are desirable.

1.4 Single-Particle Fluorescence Microscopy

Single-particle fluorescence microcopy has been used to probe the physical properties of semiconductor nanocrystals. Quantum-confined CdSe NCs (1.5 – 10 nm) in which the diameter is smaller than the Bohr diameter (11.2 nm) are predicted to have atomic-like energy levels near their band edges, leading to a narrow spectral linewidth. However, an unexpected broadening of the spectral linewidth was observed in the ensemble measurements of CdSe NCs. Thus, Bawendi and coworkers first used single-particle fluorescence microscopy to eliminate the inhomogeneities in the ensemble sample of CdSe NCs. Much narrower spectral linewidths were observed and the discreet nature of energy levels in CdSe NCs was confirmed.[31]

Fluorescence microscopy has been used to observe blinking statistics in semiconductor NCs. Blinking, also called fluorescence intermittency, is an intrinsic property of fluorescent NCs in which the NC switches between on and off states. When electrons and holes recombine radiatively, NCs emit photons, and they are bright (on) in the field-of-view of the fluorescence microscope. If there are non-radiative pathways for electrons and holes to recombine, such as trapping of charge carriers, NCs will not emit photons, and they are dark (off) in the field-of-view of the fluorescence microscope. Because the fluorescence intermittency depends on the concentration and distribution of trap states, blinking can be used as a probe that helps us to characterize the composition, structure, phase change, and reaction dynamics in NCs. Routzahn and Jain correlated blinking behaviors to dopant level or exchange extent in the cation exchange reaction between CdSe and Ag_2Se.[32] They realigned the single particle trajectories to the same start point. For each time point, they calculated the on/off ratio of the emission trajectory, which is called the “bright fraction”, and plotted the trend of the bright fraction versus time. For the transformation of Ag_2Se NCs to CdSe, the nanocrystals are initially dark due to the small bandgap of Ag_2Se (such that it emits in the near

infrared). As the reaction proceeds, the bright fraction increases and reaches a plateau. For the transformation of CdSe to Ag_2Se, the NCs are initially bright. After the transition, the fraction of off states increases until the off state is dominant. They regarded the time period in which the bright fraction changes as an intermediate state and assigned this change to the dopant level in the NCs. Because of the short period of this intermediate state combined with different reaction times for different nanocrystals, this critical transitional region is averaged out in ensemble measurements of the transformation. Thus, in situ fluorescence microscopy offers a possible solution that the bright fraction or blinking statistics can be a probe of the dopant level in fluorescent NCs.

More recently, in situ single-particle fluorescence microscopy has been used to observe chemical transformations in single semiconductor nanocrystals including anion exchange, cation exchange and ion intercalation. Generally, while the reaction occurs, the NCs are illuminated by excitation light with known wavelength. Meanwhile, light emitted from the excited particles is collected by fluorescence microscope. Dichroic filters are used to separate excitation and emission light to avoid overlap. Since the collection of emitted light does not disturb the particles or the chemical environment, fluorescence microscopy can be used as an in-situ method to image how the particles change during reactions like anion exchange. Usually, the emission wavelengths of particles are different before and after transformation, due to changes in their composition and structure. In our work we use filter sets to block emission from the initial NCs but collect emission from the transformed NCs (or vice versa). In this way, the change of emission intensity will be a signature to indicate compositional and structural changes to the NC. By analyzing the intensity change with time (single-particle trajectories), we and others have concluded that each particle

reacts stochastically, but the ensemble of particles shows a statistical distribution of reaction times.[33-36]

In previous work from our group, we studied the intercalation of CH_3NH_3Br into $PbBr_2$ NCs with a uniform size using single-particle imaging.[34] Both the parent reactants (i.e., $PbBr_2$ and CH_3NH_3Br) were non-fluorescent and could not be seen under the fluorescence microscope. When individual NCs completed transformation to form fluorescent $CH_3NH_3PbBr_3$ NCs, the particles "turned on" in the microscope field-of-view. To reconstruct these experimental results as well as other chemical transformations, such as anion exchange, we have used the Monte Carlo simulations; different models were built to elucidate the mechanism of the reaction. For example, the switching time, which represents the rate of intensity rise in a trajectory, is less dependent on the concentration of the reagent for ion substitution for cases in which the initial and final structures exhibit immiscibility (e.g., cation exchange between CdSe and Ag_2Se NCs).[33] Likewise, the switching time for the intercalation of CH_3NH_3Br into $PbBr_2$ exhibited no concentration dependence, which led us to conclude that the initial and final structures were immiscible. In the contrast, for highly miscible cases like anion exchange between $CsPbCl_3$ and $CsPbBr_3$ NCs, the switching times are strongly concentration dependent.[35] Thus, the concentration dependence of the switching time is a signature to determine the relative miscibility in cases in which it is unknown.

1.5 Dissertation Outline

In this dissertation, we focus on the relationships between the structure, properties, and function of $CsPbX_3$ nanocrystals. We use single-particle fluorescence microscopy to study anion exchange in single $CsPbX_3$ NCs. We reveal that the chemical reactivity of $CsPbX_3$ NCs during anion exchange shows a stochastic nature. Using Monte Carlo simulations, we determine that the degree of structural change during the transformation of $CsPbX_3$ NCs leads to the differences in their chemical reactivity.

Chapter 1 provides an introduction to $CsPbX_3$ NCs, size effects, and single-particle fluorescence microscopy. Chapter 2 describes the use of single-particle imaging to study anion exchange between $CsPbBr_3$ and $CsPbI_3$ NCs in both directions. We observed irreversibility in the transformation of $CsPbBr_3$ NCs to $CsPbI_3$ and that of $CsPbI_3$ NCs to $CsPbBr_3$ and correlated this irreversibility with the degree of structural distortions during anion exchange. Chapter 3 describes the study of the size dependence of the transformation of $CsPbBr_3$ NCs to $CsPbI_3$. We demonstrated due to size-dependent miscibility at the nanoscale, the perovskite crystal structure undergoes different changes during the transformation of $CsPbBr_3$ NCs to $CsPbI_3$ of different sizes. Chapter 4 gives a summary of this dissertation and provides and outlook for future work.

1.6 References

1. Wikipedia World energy supply and consumption. https://en.wikipedia.org/wiki/World_energy_supply_and_consumption.

2. U4E GLOBAL LIGHTING CHALLENGE: 14 BILLION EFFICIENT LIGHTING PRODUCTS COMMITTED IN TWO YEARS. https://united4efficiency.org/cems-global-lighting-challenge-announces-14-billion-efficient-lighting-products-committed-two-years/.

3. Wikipedia LED lamp. https://en.wikipedia.org/w/index.php?title=LED_lamp&oldid=1128979042.

4. Wikipedia Light-emitting diode. https://en.wikipedia.org/w/index.php?title=Light-emitting_diode&oldid=1131106961.

5. Kovalenko, M. V.; Protesescu, L.; Bodnarchuk, M. I., Properties and potential optoelectronic applications of lead halide perovskite nanocrystals. *Science* **2017,** *358* (6364), 745-750.

6. Nedelcu, G.; Protesescu, L.; Yakunin, S.; Bodnarchuk, M. I.; Grotevent, M. J.; Kovalenko, M. V., Fast anion-exchange in highly luminescent nanocrystals of cesium lead halide perovskites (CsPbX3, X= Cl, Br, I). *Nano letters* **2015,** *15* (8), 5635-5640.

7. Swarnkar, A.; Chulliyil, R.; Ravi, V. K.; Irfanullah, M.; Chowdhury, A.; Nag, A., Colloidal CsPbBr3 Perovskite Nanocrystals: Luminescence beyond Traditional Quantum Dots. *Angewandte Chemie International Edition* **2015,** *54* (51), 15424-15428.

8. Creutz, S. E.; Crites, E. N.; De Siena, M. C.; Gamelin, D. R., Anion exchange in cesium lead halide perovskite nanocrystals and thin films using trimethylsilyl halide reagents. *Chemistry of Materials* **2018,** *30* (15), 4887-4891.

9. Akkerman, Q. A.; D'Innocenzo, V.; Accornero, S.; Scarpellini, A.; Petrozza, A.; Prato, M.; Manna, L., Tuning the optical properties of cesium lead halide perovskite nanocrystals by anion exchange reactions. *Journal of the American Chemical Society* **2015,** *137* (32), 10276-10281.

10. Karimata, I.; Tachikawa, T., In Situ Exploration of the Structural Transition during Morphology-and Efficiency-Conserving Halide Exchange on a Single Perovskite Nanocrystal. *Angewandte Chemie* **2021,** *133* (5), 2578-2583.

11. Protesescu, L.; Yakunin, S.; Bodnarchuk, M. I.; Krieg, F.; Caputo, R.; Hendon, C. H.; Yang, R. X.; Walsh, A.; Kovalenko, M. V., Nanocrystals of cesium lead halide perovskites (CsPbX3, X= Cl, Br, and I): novel optoelectronic materials showing bright emission with wide color gamut. *Nano letters* **2015,** *15* (6), 3692-3696.

12. Pellet, N.; Teuscher, J.; Maier, J.; Grätzel, M., Transforming Hybrid Organic Inorganic Perovskites by Rapid Halide Exchange. *Chemistry of Materials* **2015,** *27* (6), 2181-2188.

13. Jang, D. M.; Park, K.; Kim, D. H.; Park, J.; Shojaei, F.; Kang, H. S.; Ahn, J.-P.; Lee, J. W.; Song, J. K., Reversible Halide Exchange Reaction of Organometal Trihalide Perovskite Colloidal Nanocrystals for Full-Range Band Gap Tuning. *Nano Letters* **2015,** *15* (8), 5191-5199.

14. Green, M. A.; Ho-Baillie, A.; Snaith, H. J., The emergence of perovskite solar cells. *Nature Photonics* **2014,** *8* (7), 506-514.

15. Lin, Q.; Armin, A.; Nagiri, R. C. R.; Burn, P. L.; Meredith, P., Electro-optics of perovskite solar cells. *Nature Photonics* **2014,** *9*, 106.

16. Lian, H.; Li, Y.; Saravanakumar, S.; Jiang, H.; Li, Z.; Wang, J.; Xu, L.; Zhao, W.; Han, G., Metal halide perovskite quantum dots for amphiprotic bio-imaging. *Coordination Chemistry Reviews* **2022,** *452*, 214313.

17. Luo, F.; Li, S.; Cui, L.; Zu, Y.; Chen, Y.; Huang, D.; Weng, Z.; Lin, Z., Biocompatible perovskite quantum dots with superior water resistance enable long-term monitoring of the H 2 S level in vivo. *Nanoscale* **2021,** *13* (34), 14297-14303.

18. Alivisatos, A. P., Perspectives on the physical chemistry of semiconductor nanocrystals. *The Journal of Physical Chemistry* **1996,** *100* (31), 13226-13239.

19. Yu, W. W.; Wang, Y. A.; Peng, X., Formation and stability of size-, shape-, and structure-controlled CdTe nanocrystals: ligand effects on monomers and nanocrystals. *Chemistry of Materials* **2003,** *15* (22), 4300-4308.

20. Mclaren, A.; Valdes-Solis, T.; Li, G.; Tsang, S. C., Shape and size effects of ZnO nanocrystals on photocatalytic activity. *Journal of the American Chemical Society* **2009,** *131* (35), 12540-12541.

21. Yu, Y.; Fan, G.; Fermi, A.; Mazzaro, R.; Morandi, V.; Ceroni, P.; Smilgies, D.-M.; Korgel, B. A., Size-dependent photoluminescence efficiency of silicon nanocrystal quantum dots. *The Journal of Physical Chemistry C* **2017,** *121* (41), 23240-23248.

22. Mastronardi, M. L.; Maier-Flaig, F.; Faulkner, D.; Henderson, E. J.; Kübel, C.; Lemmer, U.; Ozin, G. A., Size-dependent absolute quantum yields for size-separated colloidally-stable silicon nanocrystals. *Nano letters* **2012,** *12* (1), 337-342.

23. Rossetti, R.; Nakahara, S.; Brus, L. E., Quantum size effects in the redox potentials, resonance Raman spectra, and electronic spectra of CdS crystallites in aqueous solution. *The Journal of Chemical Physics* **1983,** *79* (2), 1086-1088.

24. Tolbert, S.; Alivisatos, A., Size dependence of a first order solid-solid phase transition: the wurtzite to rock salt transformation in CdSe nanocrystals. *Science* **1994,** *265* (5170), 373-376.

25. Yang, R. X.; Tan, L. Z., Understanding size dependence of phase stability and band gap in CsPbI3 perovskite nanocrystals. *The Journal of chemical physics* **2020,** *152* (3), 034702.

26. Yang, F.; Wang, C.; Pan, Y.; Zhou, X.; Kong, X.; Ji, W., Surface stabilized cubic phase

of CsPbI3 and CsPbBr3 at room temperature. *Chinese Physics B* **2019,** *28* (5), 056402.

27. Zhao, Q.; Hazarika, A.; Schelhas, L. T.; Liu, J.; Gaulding, E. A.; Li, G.; Zhang, M.; Toney, M. F.; Sercel, P. C.; Luther, J. M., Size-Dependent Lattice Structure and Confinement Properties in CsPbI3 Perovskite Nanocrystals: Negative Surface Energy for Stabilization. *ACS Energy Letters* **2020,** *5* (1), 238-247.

28. Swarnkar, A.; Marshall, A. R.; Sanehira, E. M.; Chernomordik, B. D.; Moore, D. T.; Christians, J. A.; Chakrabarti, T.; Luther, J. M., Quantum dot–induced phase stabilization of α-CsPbI3 perovskite for high-efficiency photovoltaics. *Science* **2016,** *354* (6308), 92-95.

29. Chen, C.-C.; Herhold, A. B.; Johnson, C. S.; Alivisatos, A. P., Size dependence of structural metastability in semiconductor nanocrystals. *Science* **1997,** *276* (5311), 398-401.

30. Koscher, B. A.; Bronstein, N. D.; Olshansky, J. H.; Bekenstein, Y.; Alivisatos, A. P., Surface- vs Diffusion-Limited Mechanisms of Anion Exchange in CsPbBr3 Nanocrystal Cubes Revealed through Kinetic Studies. *Journal of the American Chemical Society* **2016,** *138* (37), 12065-12068.

31. Empedocles, S.; Bawendi, M., Spectroscopy of Single CdSe Nanocrystallites. *Accounts of Chemical Research* **1999,** *32* (5), 389-396.

32. Routzahn, A. L.; Jain, P. K., Luminescence Blinking of a Reacting Quantum Dot. *Nano letters* **2015,** *15* (4), 2504-2509.

33. Routzahn, A. L.; Jain, P. K., Single-nanocrystal reaction trajectories reveal sharp cooperative transitions. *Nano letters* **2014,** *14* (2), 987-992.

34. Yin, B.; Cavin, J.; Wang, D.; Khan, D.; Shen, M.; Laing, C.; Mishra, R.; Sadtler, B., Fluorescence microscopy of single lead bromide nanocrystals reveals sharp transitions during their transformation to methylammonium lead bromide. *Journal of Materials Chemistry C* **2019,** *7* (12), 3486-3495.

35. Wang, D.; Cavin, J.; Yin, B.; Thind, A. S.; Borisevich, A. Y.; Mishra, R.; Sadtler, B., Role of Solid-State Miscibility during Anion Exchange in Cesium Lead Halide Nanocrystals Probed by Single-Particle Fluorescence. *The Journal of Physical Chemistry Letters* **2020,** *11* (3), 952-959.

36. Wang, D.; Zhang, D.; Sadtler, B., Irreversibility in Anion Exchange Between Cesium Lead Bromide and Iodide Nanocrystals Imaged by Single-Particle Fluorescence. *The Journal of Physical Chemistry C* **2020,** *124* (49), 27158-27168.

Chapter 2: Irreversibility in Anion Exchange Between Cesium Lead Bromide and Iodide Nanocrystals Imaged by Single-Particle Fluorescence

This chapter is adapted with permission from Wang, D.; **Zhang, D.**; Sadtler, B., Irreversibility in Anion Exchange between Cesium Lead Bromide and Iodide Nanocrystals Imaged by Single-Particle Fluorescence. *The Journal of Physical Chemistry C* **2020,** *124*, 27158-27168.

Author contributions: Wang, D. synthesized the $CsPbI_3$ nanocrystals; **Zhang, D.** synthesized the $CsPbBr_3$ nanocrystals. Wang, D. performed experiments of anion exchange from $CsPbBr_3$ nanocrystals to $CsPbI_3$. **Zhang, D.** performed experiments of anion exchange from $CsPbI_3$ nanocrystals to $CsPbBr_3$. Both authors made contributions to sample characterization, data analysis and simulations.

2.1 Introduction

Lead halide perovskite semiconductors with the formula $APbX_3$ (where A = $CH_3NH_3^+$ or Cs^+ and X = Cl^-, Br^-, or I^-) are widely studied for applications in optoelectronic devices, including solar cells and light-emitting diodes (LEDs).[1-7] The high photoluminescence quantum yields, tunable band gap, and facile synthesis of colloidal $CsPbX_3$ nanocrystals (NCs) make them especially attractive for light-emission applications.[6-14] Starting with one initial composition prepared by the hot-injection method (e.g., $CsPbBr_3$), the emission wavelength of $CsPbX_3$ NCs can be tuned across the entire visible spectrum via anion exchange to $CsPbBr_{3-x}I_x$ or $CsPbBr_{3-x}Cl_x$.[10-12, 15-20] To maximize color purity for light-emission applications, it is critical to have high uniformity in structure and composition among the population of NCs. Early reports on anion exchange indicated that mixed-halide $CsPbBr_{3-x}Cl_x$ and $CsPbBr_{3-x}I_x$ NCs form homogenous solid solutions at all phase fractions (i.e., all values of x).[15-17] However, recent work has shown that mixed-halide lead perovskite crystals can possess structural and compositional heterogeneity,[20-24] which will be deleterious for their application in optoelectronic devices.

The solid-state miscibility between two crystalline compounds reflects the degree of similarity in their structure. $CsPbCl_3$ and $CsPbBr_3$ are miscible at all phase fractions at room temperature, while $CsPbCl_3$ and $CsPbI_3$ are immiscible due to the large difference in anion size and electronegativity.[25, 26] $CsPbBr_3$ and $CsPbI_3$ possess intermediate miscibility. The structures of $CsPbBr_3$, $CsPbI_3$, and mixed-halide $CsPbBr_{3-x}I_x$ NCs have been reported to possess either the perovskite cubic α phase,[15-17] the perovskite orthorhombic γ phase,[12, 22, 27] or the non-perovskite orthorhombic δ phase (i.e., yellow phase)[28] depending on the method used to prepare the NCs (e.g., hot-injection synthesis with mixed halide precursors vs. post-synthetic anion exchange), the method used to determine the structure (e.g., conventional powder x-ray diffraction vs.

synchrotron-based x-ray scattering), and the amount of time between sample preparation and structure measurement. Furthermore, recent studies on $CsPbX_3$ NCs synthesized by the hot-injection method have shown that the presence of size-dependent surface strain[29] and coherent twin boundaries[22] can lead to variations in the tilting of corner-sharing PbX_6 octahedra that make up the perovskite structure. While these investigations have not yet been extended to $CsPbX_3$ NCs prepared by anion exchange, we anticipate that subtle differences in the structure of the parent nanocrystals may lead to different degrees of structural reorganization as $CsPbX_3$ nanocrystals undergo anion exchange. Thus, it is critical to have an in-situ method to probe how differences in the structure of $CsPbX_3$ nanocrystals affect their chemical reactivity.

Single-particle optical measurements remove ensemble averaging to reveal differences in chemical and physical behavior among nanocrystals prepared within the same synthetic batch.[13, 14, 30-43] We and others have used single-particle fluorescence microscopy to monitor chemical transformations in semiconductor NCs including cation exchange, anion exchange, and ion intercalation based on changes in the emission intensity and wavelength of individual NCs as they transform.[39-43] These measurements quantify heterogeneity in the reactions times for a population of NCs undergoing the same transformation. In every system studied so far, the switching times, which characterize the rate at which the PL intensity changes for individual NCs, are much shorter than the time it takes for the ensemble of NCs to transform. However, each NC exhibits a different characteristic waiting time before it begins to transform, which leads to a gradual change in PL intensity for the ensemble of NCs. The difference in structure between the initial and final crystals controls the variance in reactivity among the population of NCs. Immiscible crystal pairs (e.g., $CdSe/Ag_2Se$ and $PbBr_2/CH_3NH_3PbBr_3$) that require a substantial reorganization of both cations and anions exhibit shorter waiting and switching times compared to highly miscible systems (e.g.,

$CsPbCl_3$/$CsPbBr_3$) in which a phase transformation does not occur.[39-42] Furthermore, the switching times for miscible systems show a stronger dependence on the concentration of the substitutional ion.

In this chapter, we used single-particle fluorescence microscopy to image anion exchange in $CsPbBr_3$ and $CsPbI_3$ nanocrystals. We observed asymmetric behavior at both the ensemble and single-particle levels when the interconversion between $CsPbBr_3$ and $CsPbI_3$ proceeded in opposite directions. We develop a simple kinetic model that captures this asymmetric behavior based on the degree of reorganization of the crystal lattice during the transformation. $CsPbI_3$ NCs undergo a larger change in structure as they transform to $CsPbBr_3$ compared to when $CsPbBr_3$ NCs transform to $CsPbI_3$. The more abrupt change leads to a narrower distribution of reaction times when as-synthesized $CsPbI_3$ NCs undergo anion exchange to $CsPbBr_3$. Our study reveals that anion exchange between $CsPbBr_3$ and $CsPbI_3$ is not completely reversible. Structural differences between $CsPbX_3$ NCs directly synthesized by the hot-injection method and those prepared by anion exchange lead to differences in their chemical reactivity.

2.2 Experimental

Materials: The following chemicals were used as received: cesium carbonate (Cs_2CO_3, 99%, Millipore Sigma Inc.), lead (II) iodide (PbI_2, 99%, Millipore Sigma Inc.), lead (II) bromide ($PbBr_2$, 98+%, Alfa Aesar), oleic acid (90%, Millipore Sigma Inc.), oleylamine (70%, Millipore Sigma Inc), tert-butanol (anhydrous, ⩾ 99.5%, Millipore Sigma Inc.), hexane (anhydrous, 95%, Millipore Sigma Inc.), 1-octadecene (ODE, tech. 90%, Alfa Aesar), toluene (anhydrous, 99.8%, Millipore Sigma Inc.), tetrabutylammonium bromide (TBAB, ⩾ 98%, Millipore Sigma Inc.), and tetrabutylammonium iodide (TBAI, ⩾ 98%, Millipore Sigma Inc.).

Synthesis of cesium lead halide perovskite nanocrystals: The hot-injection method reported by Kovalenko and coworkers was adapted to synthesize colloidal cesium lead iodide ($CsPbI_3$) and cesium lead bromide ($CsPbBr_3$) nanocrystals (NCs).[8] Instead of drying the oleic acid and oleylamine separately, we mixed these surfactants with the other precursors (i.e., Cs_2CO_3 or PbX_2) and dried them together. In a typical synthesis, 102 mg of Cs_2CO_3, 0.32 mL of oleic acid, and 5 mL of ODE were added to a 50-mL, round-bottom flask (labeled as Flask I). For the synthesis of $CsPbI_3$, 87 mg of PbI_2, 0.7 mL of oleylamine, 0.7 mL of oleic acid, and 5 mL of ODE were added into another 50-mL, round-bottom flask (labeled as Flask II). For the synthesis of $CsPbBr_3$, 69 mg of $PbBr_2$, 1 mL of oleylamine, 1 mL of oleic acid, and 5 mL of ODE were added to Flask II. Both flasks were connected to a Schlenk line. Flask I was heated at 120°C under vacuum for 1 hour and then heated at 150°C under argon for another hour. Flask II was heated at 100°C under vacuum for 1 hour. Then, Flask II was switched to an argon environment, and the temperature was elevated to 170°C. Next, 0.4 mL of the solution from Flask I was removed using a syringe and quickly injected into Flask II. After 60 s, Flask II was quenched in an ice bath. After cooling, the mixture

in Flask II was centrifuged at 8000 rpm for 5 mins. The precipitate was collected, dispersed in 10 mL of anhydrous hexane, and stored in a nitrogen-filled glovebox for future use.

Photoluminescence (PL) spectroscopy: PL spectra were measured by using a Cary Eclipse fluorescence spectrophotometer. The scan rate was set to medium, and the step size was 1 nm. The slit widths for excitation and emission were adjusted between 2.5 and 10 nm to obtain spectra with maximum intensities of around 500 counts. The excitation wavelength was 400 nm.

Anion exchange reactions between $CsPbBr_3$ and $CsPbI_3$ NCs in colloidal solution were monitored at the ensemble level by PL spectroscopy. TBAI was used to transform $CsPbBr_3$ NCs into $CsPbI_3$, and TBAB was used to transform $CsPbI_3$ NCs into $CsPbBr_3$. To prepare each sample, the stock solution of $CsPbBr_3$ or $CsPbI_3$ NCs was first diluted by a factor of 100 by adding 50 μL of the stock solution to 5 mL of hexane. Then, 1.5 mL of the diluted $CsPbX_3$ solution and 1 mL of hexane were added to a quartz cuvette. First, a PL spectrum of the initial $CsPbX_3$ NCs was measured. Then, aliquots of either the TBAB or TBAI solution (0.3 mg/mL in tert-butanol) were added sequentially to the cuvette. The volume of TBAB/TBAI for each addition was 60 and 80 μL, respectively. After each addition, the cuvette was vigorously shaken for 30 s before measuring the PL spectrum. Anion exchange was considered complete when further addition of the TBAB/TBAI solution led to shifts in the PL spectra of less than 2 nm.

Single-particle fluorescence imaging: Fluorescence microscopy was performed by using a Nikon N-STORM microscopy system consisting of a Nikon TiE motorized inverted optical microscope and a Nikon CFI-6-APO TIRF 100× oil-immersion objective lens with a numerical aperture of 1.49 and a working distance of 210 μm. A white-light LED (X-cite 120 LED) was used as the

excitation source. Dilute solutions of the $CsPbX_3$ NCs were spin-coated onto microscope coverslips and assembled into flow cells. See the **Appendix A** and our previous work for additional details on sample preparation.[41, 42] Diluting the stock solution of $CsPbX_3$ NCs by a factor of 500 before spin-coating provided a sufficient number of NCs in the microscope field-of-view to gather statistics of the reaction trajectories while minimizing the number of clusters of particles. No further preparation was needed for the majority of NCs to remain fixed to the substrate while imaging anion exchange. To watch the transformation of $CsPbI_3$ NCs to $CsPbBr_3$, we first used a red filter set (Chroma #49005-ET-DSRed, excitation window: 530 – 558 nm, emission window: 590 – 649 nm) to focus on emission from the initial $CsPbI_3$ NCs. We then switched to a green filter set (Chroma #49002-ET-EGFP, excitation window: 450 – 490 nm, emission window: 500 – 540 nm) to image anion exchange. In this case, the initial field-of-view is dark, and individual NCs become bright as they undergo anion exchange. A solution of ODE and tert-butanol (25:1 volume ratio) was first flowed into the flow cell. Next, a solution of TBAB in ODE and tert-butanol (25:1 volume ratio) was flowed into the cell to trigger anion exchange. The flow rate was fixed at 20 mL/h by a syringe pump. The concentrations of TBAB used were 1, 2, 3, 4, 6, and 10 μg/mL (i.e., 3.1, 6.2, 9.3, 12.4, 18.6, and 31.0 μmol/L). Fluorescent videos were recorded at a light intensity of ~29 $\mu W/cm^2$ at the focal plane using the green filter set. An Andor iXon 897 electron-multiplying CCD camera (512 ×512, 16 μm pixels, > 90% quantum efficiency) was used to detect fluorescence signals, and the exposure time was 20 ms.

To watch the transformation of $CsPbBr_3$ NCs to $CsPbI_3$, we first used the green filter set to focus on emission from the initial $CsPbBr_3$ NCs and then switched to the red filter set to watch the turn-on in emission as NCs underwent anion exchange. Solutions of TBAI in ODE and tert-butanol (25:1 volume ratio) were used to trigger anion exchange. The concentrations of TBAI used were

1, 2, 3, 4, 6, and 10 μg/mL (i.e., 2.7, 5.4, 8.1, 10.8, 16.2, and 27.0 μmol/L). Fluorescent videos were recorded at a light intensity of ~18 $\mu W/cm^2$ at the focal plane using the red filter set and an exposure time of 20 ms. For the back conversion of $CsPbBr_{3-x}I_3$ NCs that had already undergone anion exchange, the green filter set was used to watch the conversion back to $CsPbI_3$, and the red filter set was used to watch conversion back to $CsPbBr_3$. For each of these transformations, the initial field-of-view was bright, and the NCs became dark as they underwent anion exchange.

Image analysis: Intensity vs. time trajectories for individual $CsPbX_3$ NCs were extracted from the recorded fluorescence videos as described in our previous work.[41, 42] The brightness and contrast of each video was auto-adjusted by using look-up tables (LUTs) in the Nikon-NIS Elements AR software (version 4.50.00) based on the intensity distribution of all NCs in the field-of-view. This non-destructive method of brightness modification provides the best visibility of NCs in each video. We next excluded clusters of particles (i.e., multiple NCs emitting within a diffraction-limited spot) by analyzing the distribution of intensity values. Intensity trajectories exhibiting fluorescence intermittency with clear 'on' and 'off' states are indicative of single particles (see **Figure 2.15**) based on previous reports.[13, 36, 37, 44, 45] However, in a cluster of particles the intensity trajectories of multiple NCs overlap, resulting in trajectories with multiple 'on' states and without a clear 'off' state (**Figure 2.16**). Clusters of particles were excluded from the subsequent analysis.

We measured the 'waiting time' and 'switching time' for hundreds of single NCs at each concentration of TBAB or TBAI to quantify differences in the kinetics of anion exchange in different directions. For the transformations of as-synthesized $CsPbBr_3$ NCs to $CsPbI_3$ and as-synthesized $CsPbI_3$ NCs to $CsPbBr_3$, we watched the NCs 'turn on' during anion exchange. For the back conversion of $CsPbBr_{3-x}I_3$ NCs that had already undergone exchange prior to imaging,

we watched the NCs 'turn off' under the microscope. In these cases, the intensity trajectories were reversed along the x-axis (i.e., time) so that all trajectories could be analyzed in the same way. The waiting time for each NC to 'turn on' was defined by time point where the mean intensity (averaged over 10 data points in a 200-ms window) in a trajectory reached a threshold value, V:

$$V = m + 5\sigma \tag{2.1}$$

where m is the mean intensity (averaged over 100 data points in a 2-s window) for the trajectory before the reaction starts, and σ is the standard deviation for a Gaussian fit to the intensity fluctuations in this region. To compare the waiting times using different concentrations of TBAB or TBAI, the waiting time for the first NC to transform was defined as 0 s, and the waiting times for all other NCs in the same field-of-view were determined relative to the first one. Each distribution of relative waiting times was plotted as a histogram, and the mean value and full width at half maximum (FWHM) were extracted from a Gaussian fit (see **Figures 2.17– 2.20**).

The switching time for each NC was determined by fitting its intensity trajectory to a sigmoidal function:

$$I(t) = I_{initial} + \frac{\left(I_{final} - I_{initial}\right)}{1 + e^{(b - t/\tau)}} \tag{2.2}$$

where $I_{initial}$ and I_{final} are mean values of the intensity (averaged over 100 data points in a 2-s window) at the start and near the maximum of a single-particle trajectory, respectively, and τ is the switching time. The values of b and τ were extracted from fitting the intensity trajectory using MATLAB. Due to the fluorescence intermittency of the NCs, some trajectories could not easily be fit to a sigmoidal function. The goodness of the fit was evaluated by the correlation coefficient between the fitted curve and the original trajectory. Only trajectories with a correlation coefficient above 0.8 were used in subsequent analysis.

The rise time in fluorescence intensity over the entire field-of-view was also measured (i.e., the ensemble intensity trajectory) for the different transformations. The ensemble rise time was defined as half the time it takes for the mean intensity (averaged over 5 adjacent data points) in an ensemble trajectory to increase from 25% to 75% of the maximum intensity (averaged over 5 data points after the maximum point). A comparison of the ensemble rise times for anion exchange in different directions vs. the mean switching time for individual NCs is shown in **Figure 2.14**.

Monte Carlo simulations: Monte Carlo simulations were used to model the reaction trajectories for anion exchange between $CsPbBr_3$ and $CsPbI_3$ NCs. The simulations were similar to our previous work on modeling anion exchange between $CsPbCl_3$ and $CsPbBr_3$ NCs[42] and the intercalation of CH_3NH_3Br into $PbBr_2$ NCs[41] as well as work by Routzahn and Jain on cation exchange between CdSe and Ag_2Se NCs.[39] Each simulation consisted of an ensemble of 500 particles, and each particle possessed 20 sites for anion exchange. At each time step, a particle among the population was chosen at random. If the particle had already completely transformed (i.e., all 20 sites had undergone exchange), then the trajectory moved on to the next step without exchange. Otherwise, the probability for the i^{th} exchange event to occur in a particle was defined as p_i. The exchange event occurred only if p_i was larger than a randomly chosen number between 0 and 1. Each simulation ended when the average number of exchanged sites among the population of particles reached 19.998 or the total number of time steps reached 600,000. The value of p_i was determined by an equilibrium constant k_i and the change in free energy ΔG_i for anion exchange. We developed different models based on the way each of these values evolved with consecutive reaction events in a particle as it undergoes exchange. The relationships between $p_i, k_i,$ and ΔG_i are given by the following equations:

$$k_i = \exp(-\Delta G_i) \tag{2.3}$$

$$p_i = \frac{k_i}{1 + k_i} \tag{2.4}$$

The change in free energy for each exchange event is given by:

$$\Delta G_i = \Delta G_0 + \Delta g_i \tag{2.5}$$

where ΔG_0 is a constant that depends on the simulated concentration of substitutional ions, and the value of Δg_i changes with the number of successful events. In both models described below, the initial value, k_1, was varied from 0.03 to 0.24 to simulate the concentration dependence of waiting of switching times. The initial value of $k = 0.03$ was adapted from our previous work,[41, 42] which allows the code to run within in a reasonable number of time steps (i.e., 600,000 steps in these simulations). The variation of the value of k is approximately one order of magnitude, similar to the experimental variation of concentration. A scaling factor of 0.03 was used to convert the value of k_1 into the simulated concentrations, k_0:

$$k_0 = \frac{k_1}{0.03} \tag{2.6}$$

After conversion, the values of the simulated concentrations are comparable to experimental ones when the TBAI/TBAB concentration is given in μg/mL as in **Figure 2.4**. The waiting time for each particle in a trajectory was defined as the simulated time when 50% of the sites in the particle (i.e., 10 out of 20) had undergone exchange. The switching time for each particle was defined as half of the time difference between when 25% and 75% of the sites in the particle had undergone exchange.

Exchange-density model: We previously developed this model to simulate anion exchange between $CsPbCl_3$ and $CsPbBr_3$ NCs in which the initial and final crystals possess high

miscibility.[42] In this model, the value ΔG_i decreases continuously as the number of successful exchange events in each particle increases.

$$\triangle g_i = -\delta i^2 \tag{2.7}$$

where δ is an empirical constant = 0.005. In this model the probability for exchange, p_i, to occur is proportional to the density of exchanged ions in the particle. Further details of this model can be found in our previous work.[42]

Structural-reorganization model: This model is an adaptation of one that we previously developed to describe the intercalation of CH_3NH_3Br into $PbBr_2$ nanocrystals in which there is a significant change in structure during the transformation.[41] In this model, ΔG_i for exchange is initially constant. After a critical threshold of successful events in a particle ($i_c = 5$ in these simulations), the value of ΔG_i begins to decrease with the number of events:

$$\triangle g_i = \delta \times \Delta G_0 \left((i - i_c + 1)^{-1/5} - 1\right) \text{ for } i \geq i_c \tag{2.8}$$

where δ is an empirical constant = 2.4. ΔG_0 is the change in free energy for the first exchange event in a particle. In our previous phase-transformation model, $\triangle g_i = \delta \times \Delta G_0\big((i - i_c + 1)^{-1/3} - 1\big)$, and $i_c = 4$. Empirically, we found that the $i^{-1/5}$ dependence gave a better match to the experimental waiting and switching times for the conversion of $CsPbI_3$ NCs to $CsPbBr_3$ shown in **Figure 2.5**. The $i^{-1/5}$ dependence used in the current simulations provides a less abrupt change in ΔG_i, which is expected as the degree of structural reorganization when $CsPbI_3$ NCs transform to $CsPbBr_3$ is smaller compared to when $PbBr_2$ NCs transform into $CH_3NH_3PbBr_3$.

2.3 Results

Ensemble fluorescence spectroscopy. $CsPbX_3$ (X = Br or I) nanocrystals were synthesized using the hot-injection method developed Kovalenko and co-workers (see the **Experimental section 2.2** for further details).[8] Different halide sources have previously been used to induce anion exchange in $CsPbX_3$ NCs including lead halide salts, alkylammonium halides, and trimethylsilyl halides.[10-12, 15-20] We have found that tetrabutylammonium halides dissolved in a mixture of tert-butanol and a non-polar solvent (either hexane or 1-octadecene) induces anion exchange while minimizing degradation of the NCs as evidenced by ensemble and single-particle fluorescence.[42] We first studied the interconversion between $CsPbBr_3$ and $CsPbI_3$ NCs at the ensemble level using photoluminescence (PL) spectroscopy. $CsPbBr_3$ NCs were transformed to $CsPbI_3$ by successively adding 80 μL aliquots of a solution of tetrabutylammonium iodide (TBAI, 0.3 mg/mL = 0.81 mmol/L in tert-butanol) to a hexane solution of $CsPbBr_3$ NCs. The cuvette was shaken after the addition of each aliquot, and it took less than 30 s for the emission maximum to stop shifting after adding the TBAI solution. Therefore, following each addition, we allowed anion exchange to proceed for 30 s before acquiring a PL spectrum. PL spectra of the as-synthesized $CsPbBr_3$ NCs and resulting mixed-halide $CsPbBr_{3-x}I_x$ NCs are shown in **Figure 2.1(a)**. The emission maxima continuously red-shifted from 502 nm to 643 nm as five aliquots of the TBAI solution were added. The full width at half maximum (FWHM) of the PL spectra were similar for the both initial $CsPbBr_3$ NCs (0.13 eV) and for the iodide-rich $CsPbBr_{3-x}I_x$ NCs (0.11 eV) following the final aliquot of TBAI (see **Table 2.1**). Assuming a linear change in band gap energy with composition,[19] the composition of the product NCs after the total addition of 400 μL of the TBAI solution (0.32 μmol of TBAI) was $CsPbBr_{0.3}I_{2.7}$. Further addition of TBAI led to a minimal shift (i.e., < 2 nm) of the resulting PL spectra.

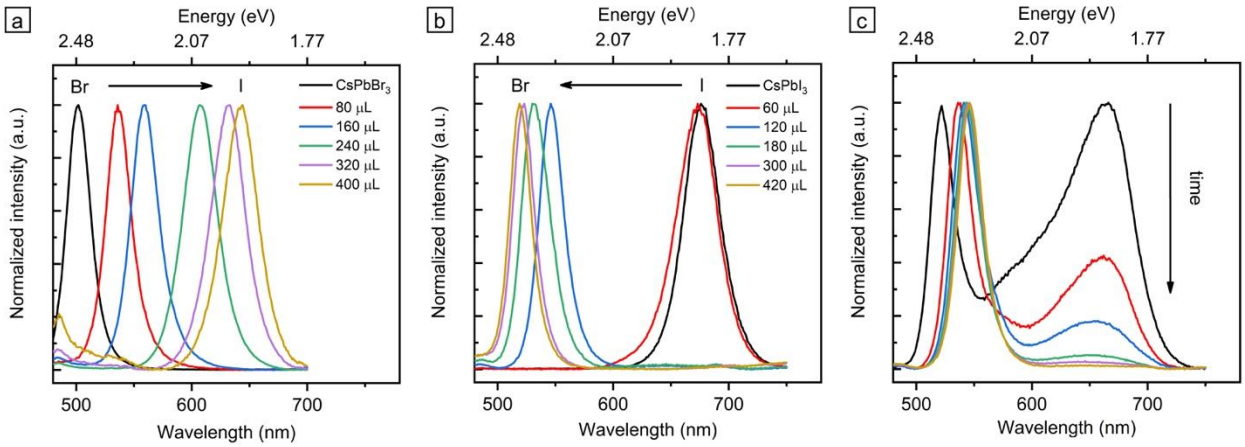

Figure 2.1. (a) PL spectra showing the transformation of $CsPbBr_3$ NCs to $CsPbI_3$ through the addition of increasing amounts of a TBAI solution in tert-butanol with a concentration of 0.3 mg/mL (0.81 mM/L). (b) PL spectra showing the transformation of $CsPbI_3$ NCs to $CsPbBr_3$ through the addition of increasing amounts of a TBAB solution in tert-butanol with a concentration of 0.3 mg/mL (0.93 mM/L). (c) Temporal evolution of the PL spectra over an approximately 8-minute period after the addition of two aliquots of the TBAB solution (120 μL total) to a solution of $CsPbI_3$ NCs. Each acquisition took approximately 30 s, and there were 1-minute intervals between spectra. All PL spectra were normalized to same maximum intensity, and the excitation wavelength was 400 nm for all spectra.

$CsPbI_3$ NCs were transformed to $CsPbBr_3$ by successively adding 60 μL aliquots of a solution of tetrabutylammonium bromide (TBAB, 0.3 mg/mL = 0.93 mmol/L in tert-butanol) to a hexane solution of $CsPbI_3$ NCs (**Figure 2.1(b)**). After the second aliquot (i.e., 120 μL total of the TBAB solution), the resulting spectrum of the mixed-halide $CsPbBr_{3-x}I_x$ NCs changed over the course of several minutes. The temporal evolution of the PL spectra after the second aliquot is shown in **Figure 2.1(c)**. The PL spectrum first split into two peaks, one centered at 522 nm and the other at

666 nm (corresponding to $CsPbBr_{2.6}I_{0.4}$ and $CsPbBr_{0.1}I_{2.9}$ respectively). Over a period of several minutes, the peak centered at 666 nm decreased in intensity while the peak originally centered at 522 nm red-shifted in its peak maximum to 546 nm (corresponding to $CsPbBr_{2.2}I_{0.8}$). Similar to the transformation of $CsPbBr_3$ to $CsPbI_3$, subsequent additions of TBAB required less than 30 seconds for the peak maximum to stop shifting (**Figure 2.1(b)**). The FWHM of the PL spectra were similar for the both initial $CsPbI_3$ NCs (0.11 eV) and for the bromide-rich $CsPbBr_{3-x}I_x$ NCs (0.11 eV) following the final aliquot of TBAB (see **Table 2.2**). Based on its peak maximum at 519 nm, the composition of the product NCs after a total of 420 μL of the TBAB solution (0.39 μmol of TBAB) was $CsPbBr_{2.6}I_{0.4}$. When 420 μL of the TBAB solution was added all at once rather than in 60 μL aliquots, the PL spectrum was also observed to first split into two peaks and then merge into a single peak centered at 518 nm after several minutes (**Figure 2.6**).

Thus, two populations of nanocrystals, one iodide-rich and one bromide-rich, were readily observable during the ensemble transformation of $CsPbI_3$ NCs to $CsPbBr_3$ but not during the transformation of $CsPbBr_3$ NCs to $CsPbI_3$ (at the time scale that the steady-state PL spectra were obtained). The continuous red-shifting of PL spectra with successive TBAI addition during the transformation of $CsPbBr_3$ NCs to $CsPbI_3$ closely resembles systems in which the initial and final crystal possess high solid solubility, such as anion exchange between $CsPbCl_3$ and $CsPbBr_3$ NCs[15, 25, 42] or cation exchange between CdTe and HgTe NCs.[46] On the other hand, the abrupt shift in PL peak position during the transformation of $CsPbI_3$ NCs to $CsPbBr_3$ with increasing TBAB addition bears similarity to NC transformations in which the initial and final crystals lack miscibility, such as the conversion of CdSe to Ag_2Se NCs via cation exchange. In this reaction, optical spectra can be assigned to linear combinations of purely CdSe and purely Ag_2Se NC spectra with no identifiable intermediates.[39, 47] In the transformation of $CsPbI_3$ NCs to $CsPbBr_3$, the two

populations of NCs show partial miscibility based on the shifts in peak maxima for the bromide-rich and iodide-rich fractions.

Structural characterization. Characterization of the $CsPbX_3$ NCs before and after anion exchange using bright-field transmission electron microscopy (TEM) and x-ray diffraction (XRD) is shown in **Figures 2.7** through **2.10**. Due to slow degradation of the $CsPbX_3$ NCs even when stored in a nitrogen-filled glovebox over the course of several months and laboratory shutdowns amidst the Covid-19 pandemic these structural characterizations were performed on different batches of $CsPbBr_3$ and $CsPbI_3$ NCs (prepared using the same reaction conditions) than the ones used for ensemble and single-particle fluorescence. Ensemble PL spectra of the different batches of NCs are shown in **Figure 2.11**. The PL maxima and FWHM for both $CsPbBr_3$ samples are nearly identical, and the same is true for both $CsPbI_3$ samples. The as-synthesized $CsPbBr_3$ and $CsPbI_3$ NCs have a platelet shape with average edge lengths of 9.4 ± 1.5 nm and 11.3 ± 2.5 nm (average ± 1st standard deviation), respectively (**Figures 2.7** and **2.8**). Anion exchange was performed by drop casting a solution of either TBAI onto $CsPbBr_3$ NCs or TBAB onto $CsPbI_3$ NCs dispersed on a TEM grid. Histograms of the edge lengths before and after anion exchange are provided in **Figure 2.9** and show that the original size and shape of the NCs are preserved after anion exchange. The expected change in lateral dimensions after anion exchange based on the larger lattice volume of $CsPbI_3$ compared to $CsPbBr_3$ is within the first standard deviation of the size distributions for these batches of NCs. Thus, we do not observe a significant change in the average edge length after anion exchange, similar to previous work.[12]

X-ray diffraction (XRD) patterns of the $CsPbX_3$ NCs before and after anion exchange are shown in **Figure 2.10**. The patterns of all samples matched most closely with simulated patterns

for the respective perovskite orthorhombic γ phase of $CsPbX_3$. For example, the as-synthesized $CsPbI_3$ NCs possess peaks that are present in the orthorhombic γ phase of $CsPbI_3$ but absent in the cubic α phase. Additionally, peaks indicative of the non-perovskite δ phase in the initial $CsPbI_3$ sample are absent. The XRD patterns displayed the expected peak shifts to smaller angles when $CsPbBr_3$ NCs were converted to $CsPbI_3$ and to larger angles when $CsPbI_3$ NCs were converted to $CsPbBr_3$. However, similar to the ensemble PL spectra described above, the XRD patterns indicate that the NCs still contained a residual amount of the parent anion after exchange, even when an excess of the substitutional anion was used. At the high concentrations of NCs needed to prepare samples for XRD (relative to samples used for ensemble PL and TEM described above), some aggregation and degradation was observed in the samples after anion exchange as evidenced by narrower peaks (indicating larger crystallite size) and the presence of peaks belonging to the non-perovskite δ phase as an impurity in $CsPbI_3$ NCs produced by anion exchange (see **Figure 2.10**). The potential effects of particle degradation should be minimal in the fluorescence microscopy studies described below. The NCs are fixed to a glass substrate such that aggregation during anion exchange cannot occur. Furthermore, the non-perovskite δ phase of $CsPbI_3$ is non-fluorescent and therefore will not be detected during fluorescence imaging.

Single-particle fluorescence imaging: Further interpretation of the PL spectra shown in **Figure 2.1** is limited as the observed spectral shifts are averaged over all nanocrystals in the cuvette, which are undergoing different rates of anion exchange. Thus, we used single-particle PL microscopy to understand the origins of the asymmetric behavior observed for anion exchange between $CsPbBr_3$ and $CsPbI_3$ NCs. The change in the emission wavelength and intensity for individual NCs provides a signature of their transformation.[39-42] We prepared samples for single-particle imaging by spin-

coating dilute solutions of $CsPbX_3$ NCs onto microscope coverslips. Each sample was then assembled into a home-made flow cell used to introduce the substitutional anion, either TBAI or TBAB dissolved in tert-butanol and 1-octadecene (additional details on sample preparation are provided in the **Experimental** section **2.2**). We used two different filter sets to image the transformation between $CsPbBr_3$ and $CsPbI_3$ NCs. A red filter set (Chroma #49005-ET-DSRed, excitation window: 530 – 558 nm, emission window: 590 – 649 nm) was used to image the conversion of $CsPbBr_3$ NCs to $CsPbI_3$. As illustrated in **Figure 2.2(a)**, the red filter blocks emission from the initial $CsPbBr_3$ NCs but transmits emission from iodide-rich $CsPbBr_{3-x}I_x$ NCs (for $2.7 \geqslant x \geqslant 1.7$ assuming a linear relationship between bandgap and halide composition). Consequently, the initial field-of-view is dark for this transformation (**Figure 2.2(b)**). After the TBAI is injected into the flow cell, fluorescent spots begin to appear (**Figure 2.2(c)**). We also transformed $CsPbBr_3$ NCs to iodide-rich $CsPbBr_{3-x}I_x$ prior to imaging and then watched their back conversion to $CsPbBr_3$ by monitoring the turn off in emission of individual NCs with the same red filter set. Conversely, a green filter set (Chroma #49002-ET-EGFP, excitation window: 450 – 490 nm, emission window: 500 – 540 nm) was used to block emission from $CsPbI_3$ NCs but transmit emission from bromide-rich $CsPbBr_{3-x}I_x$ NCs (for $0 \leqslant x \leqslant 2$ assuming a linear relationship between bandgap and halide composition). We imaged the conversion of $CsPbI_3$ NCs to $CsPbBr_3$ using the green filter set in which the turn on in emission indicates the transformation of each NC (**Figure 2.2(d), (e)**). We also transformed $CsPbI_3$ NCs to bromide-rich $CsPbBr_{3-x}I_x$ prior to imaging and then watched their back conversion to $CsPbI_3$ by monitoring the turn off in emission of individual NCs. We note that ensemble PL and XRD indicate the exchange reaction is not complete even when an excess of substitutional anions is used, similar to a previous report.[24] For

simplicity, we refer to NCs after anion exchange as $CsPbBr_3$ or $CsPbI_3$ even though they may contain residual amounts of the parent anion.

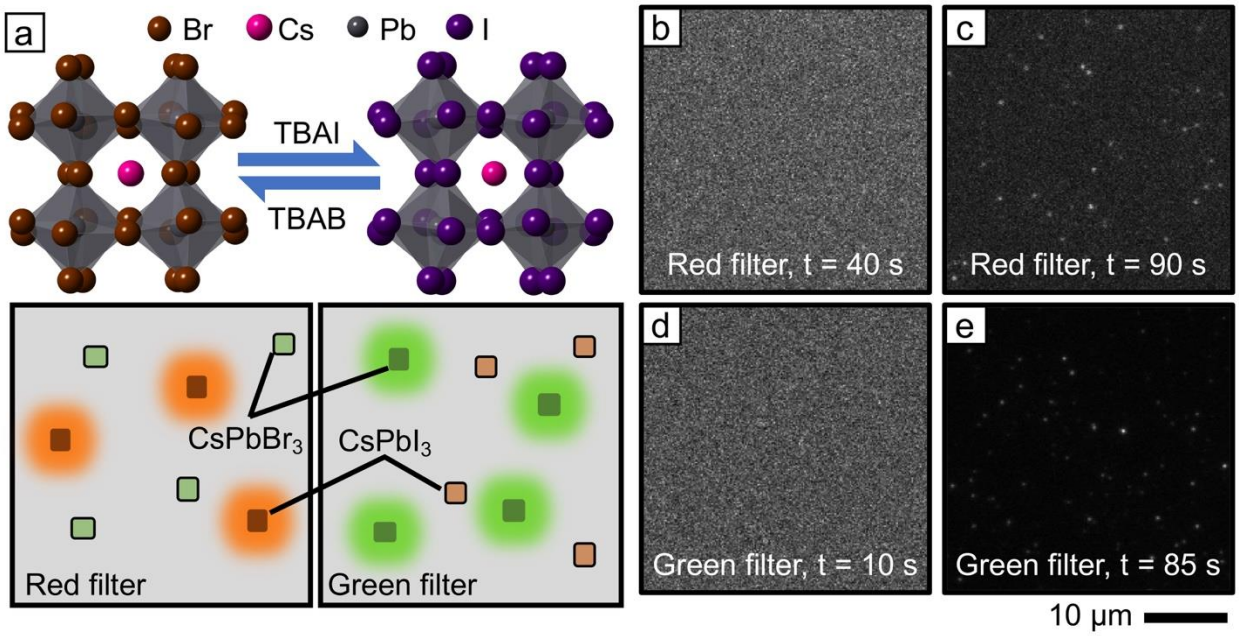

Figure 2.2. (a) Models of $CsPbBr_3$ and $CsPbI_3$ crystals with the perovskite orthorhombic γ phase (top) and illustrations of the microscope field-of-view under different excitation conditions (bottom). Emission from $CsPbI_3$ NCs is detected using the red filter set, and emission from $CsPbBr_3$ NCs is detected using the green filter set. (b, c) Fluorescence video frames before and after the transformation of $CsPbBr_3$ NCs to $CsPbI_3$ using TBAI. (d, e) Fluorescence video frames before and after the transformation of $CsPbI_3$ NCs to $CsPbBr_3$ using TBAB. Only portions of the entire field-of-view are shown in b-e.

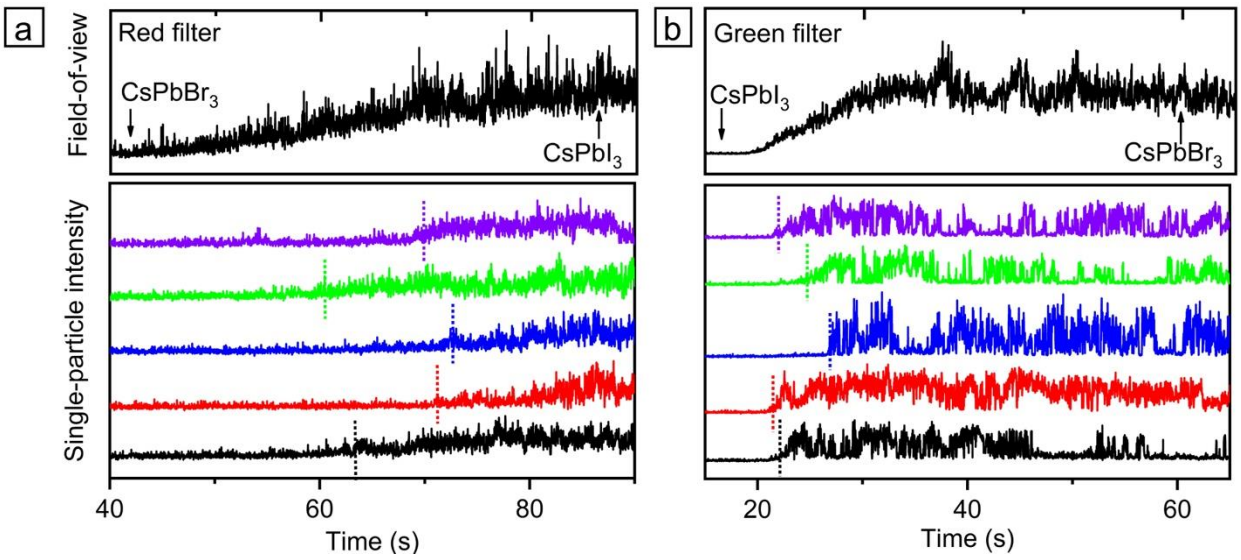

Figure 2.3. Fluorescence intensity trajectories for $CsPbX_3$ NCs undergoing anion exchange. (a) Intensity trajectory over the entire field-of-view (top) along with representative trajectories for individual NCs (bottom) during the transformation of $CsPbBr_3$ NCs to $CsPbI_3$ using TBAI at a concentration of 1 μg/mL (2.7 μmol/L). The single-particle trajectories have been vertically offset for clarity. (b) Intensity trajectory over the entire field-of-view (top) along with representative trajectories for individual NCs (bottom) during the transformation of $CsPbI_3$ NCs to $CsPbBr_3$ using TBAB at a concentration of 1 μg/mL (3.1 μmol/L). The vertical dashed lines in the individual trajectories mark the waiting time for the NC.

Figure 2.3 compares the change in fluorescence intensity integrated over the entire microscope field-of-view during anion exchange to representative trajectories for individual NCs. For flow rates between 10 and 25 mL/h used to introduce the TBAI or TBAB solution, the transformation times were independent of flow rate (**Figure 2.12**), and a flow rate of 20 mL/h was used in the experiments described below. Furthermore, the transformation times of individual NCs were independent of their position within the field-of-view (**Figure 2.13**) indicating that the reaction

trajectories are controlled by the solid-state transformation of each NC rather than the diffusion of anions in solution. The ensemble trajectories shown in the top panels of **Figure 2.3** include hundreds of single-particle trajectories (only portions of the field-of-view are shown in **Figures 2.2(b-e)**). As shown in the bottom panels of **Figure 2.3**, individual NCs undergo relatively sharp transitions relative to the ensemble. A comparison of ensemble rise-times at different concentrations of substitutional ion to the mean intensity rise for individual NCs undergoing anion exchange is provided in **Figure 2.14**. The PL intensities of individual NCs start to rise at different times (marked by the dashed lines in **Figure 2.3**). Thus, the ensemble intensity rise incorporates the intensity rises of individual NCs as well as different waiting times before each NC starts to react. Notably, the trajectories of $CsPbI_3$ NCs transforming to $CsPbBr_3$ exhibit sharper rises in intensity compared to the trajectories of $CsPbBr_3$ NCs transforming to $CsPbI_3$ at both the ensemble and single-particle levels.

We quantified differences in the trajectories of individual NCs based on both the waiting time for the emission intensity of each NC to start increasing and the switching time or steepness of the intensity rise. To minimize the number of clusters that were included this analysis, we only analyzed trajectories that exhibited fluorescence intermittency with clear 'on' and 'off' states that are typically observed in the intensity trajectories of single particles (see **Figure 2.15** for examples).[13, 36, 37, 44, 45] Intensity trajectories with multiple 'on' states and without a clear 'off' state indicate a cluster of particles (i.e., multiple particles emitting within a diffraction-limited spot size, see **Figure 2.16** for examples) and were excluded from subsequent analysis. The waiting time was measured as the time it took for the intensity of the NC to reach a value of 5σ over the mean background intensity before the reaction (where σ is the standard deviation in background intensity). Because it is difficult to measure the exact time the TBAI or TBAB solution enters the

field-of-view under the microscope, the first NC to transform was given a waiting time of 0 s, and the waiting times of subsequent transformations were measured relative to the first one. Histograms of the distributions of waiting times for the conversion of $CsPbBr_3$ NCs to $CsPbBrI_3$, $CsPbI_3$ NCs to $CsPbBr_3$, and $CsPbBr_{3-x}I_3$ NCs (produced by anion exchange prior to imaging) to both $CsPbBr_3$ and $CsPbI_3$ are shown in **Figures 2.17 – 2.20**. We fitted each distribution to a Gaussian function to extract both the mean value and the standard deviation of waiting times (**Figure 2.21**). The switching time for each NC was measured based on a sigmoidal fit of its intensity rise; a steeper rise in intensity gives a smaller value for the switching time. Similar to the waiting times, for each transformation we extracted the mean switching time and standard deviation from Gaussian fitting of the distribution of switching times.

To understand the asymmetric behavior observed in ensemble PL spectra at different concentrations of substitutional anion, we performed each transformation over a range of TBAI/TBAB concentrations (i.e., 1, 2, 3, 4, 6, 10 μg/mL) and measured the resulting distributions of waiting and switching times. For the transformation of $CsPbBr_3$ NCs to $CsPbI_3$, shown in **Figure 2.4(a)**, the mean and standard deviation of waiting times decreased from 22.8 ± 9.7 s to 4.8 ± 2.4 s as the concentration of TBAI increased from 1 to 10 μg/mL (2.7 to 27.0 μmol/L). The mean and standard deviation of switching times for this transformation decreased from 6.2 ± 2.1 s to 2.5 ± 0.8 s as the concentration of TBAI increased from 1 to 10 μg/mL. The concentration dependencies of the waiting and switching times for the transformation of $CsPbI_3$ NCs to $CsPbBr_3$ are shown in **Figure 2.4(c)**. The mean waiting and switching times and their standard deviations decreased from 6.7 ± 3.1 s to 2.4 ± 1.6 s and from 1.8 ± 1.2 s to 0.6 ± 0.5 s, respectively as the concentration of TBAB increased from 1 to 10 μg/mL (3.1 to 31.1 μM/L). Thus, in both exchange directions the waiting and switching times decreased as the concentration of TBAB/TBAI increased. The shorter

waiting and switching times for the transformation of $CsPbI_3$ NCs to $CsPbBr_3$ at low TBAB concentrations (along with the narrower distribution of waiting times) lead to the sharper rise in intensity for the ensemble of particles shown in **Figure 2.3(b)**.

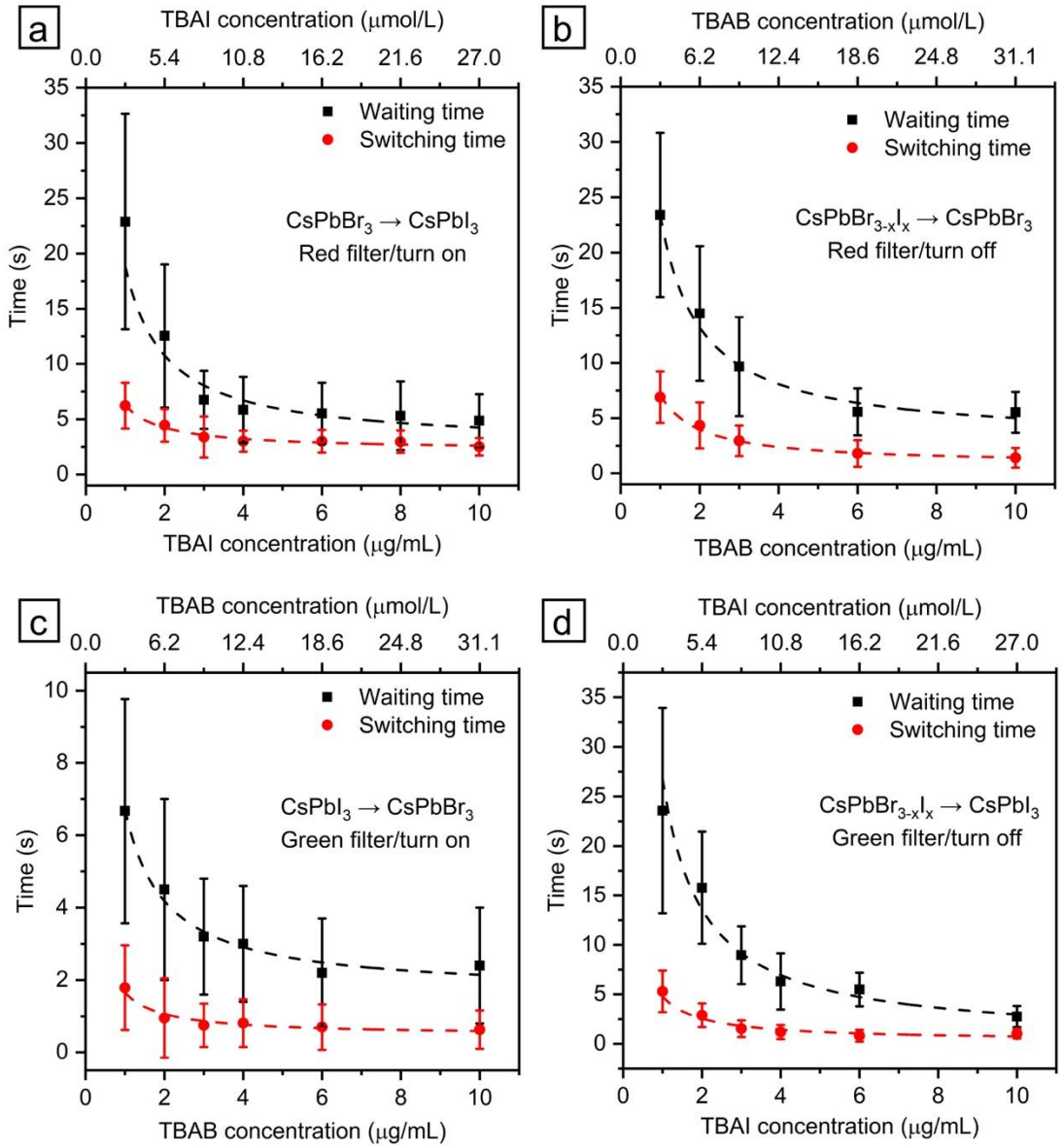

Figure 2.4. Experimental mean values of the waiting times (black squares) and switching times (red circles) for anion exchange between $CsPbBr_3$ and $CsPbI_3$ NCs. (a) Transformation of $CsPbBr_3$ NCs to $CsPbI_3$. (b) Back conversion of iodide-rich $CsPbBr_{3-x}I_x$ NCs (prepared by anion exchange

of $CsPbBr_3$ prior to imaging) to $CsPbBr_3$. (c) Transformation of $CsPbI_3$ NCs to $CsPbBr_3$. (d) Back conversion of bromide-rich $CsPbBr_{3-x}I_x$ NCs (prepared by anion exchange of $CsPbI_3$ prior to imaging) to $CsPbI_3$. The error bars for each data point indicate the standard deviation of the waiting/switching times. The dashed lines in each plot are fits to the concentration dependence of the form $y = a/x + b$. The fitted values of a and b are summarized in **Table 2.4**.

The mean values of the waiting and switching times for anion exchange and their dependence on concentration showed significant differences in the two exchange directions. The mean waiting time for the conversion of $CsPbBr_3$ NCs to $CsPbI_3$ was 16 s longer than the conversion of $CsPbI_3$ NCs to $CsPbBr_3$ when using 1 μg/mL of TBAI or TBAB. The difference between mean waiting times decreased at higher concentrations of the substitutional anion with only a 2-s difference at 10 μg/mL. The mean waiting times for the conversion of $CsPbBr_3$ NCs to $CsPbI_3$ decreased by 80% as the concentration increased from 1 to 10 μg/mL, while they only decreased by 60% for the conversion of $CsPbI_3$ NCs to $CsPbBr_3$. The mean switching times also showed differences in their concentration dependence in each exchange direction. The mean switching times for the conversion of $CsPbBr_3$ NCs to $CsPbI_3$ decreased by 50% as the TBAI concentration increased from 2 μg/mL to 10 μg/mL, while the mean switching times for the conversion of $CsPbI_3$ NCs to $CsPbBr_3$ decreased by only 30% over the same concentration range of TBAB. Overall, the mean waiting and switching times for the conversion of as-synthesized $CsPbBr_3$ NCs to $CsPbI_3$ exhibited a stronger dependence on the concentration of the substitutional ion.

Mixed-halide $CsPbBr_{3-x}I_x$ nanocrystals produced by anion exchange exhibited similar mean waiting and switching times to those of the as-synthesized $CsPbBr_3$ NCs undergoing exchange to $CsPbI_3$ regardless of the exchange direction. We converted $CsPbBr_3$ NCs to iodide-rich

$CsPbBr_{3-x}I_x$ and then imaged their back conversion under the microscope to $CsPbBr_3$ using different concentrations of TBAB (**Figure 2.4(b)**). Using the red filter set, we observed the initially bright fluorescent spots in the field-of-view become dark as the transformation progressed. The mean waiting and switching times and their standard deviations decreased from 23.4 ± 7.4 s to 5.5 ± 1.8 s and from 6.9 ± 2.3 s to 1.4 ± 0.9 s, respectively, as the concentration of TBAB increased from 1 to 10 μg/mL (3.1 to 31.1 μmol/L). These values for back exchange are significantly longer than the transformation of as-synthesized $CsPbI_3$ NCs to $CsPbBr_3$ and closely match those of the $CsPbBr_3$ to $CsPbI_3$ reaction. We also converted $CsPbI_3$ NCs to bromide-rich $CsPbBr_{3-x}I_x$ and then imaged their back conversion to $CsPbI_3$ under the microscope using the green filter set to watch the turn off in emission (**Figure 2.4(d)**). Similar, to the iodide-rich $CsPbBr_{3-x}I_x$ NCs undergoing back conversion, the mean waiting and switching times and their standard deviation decreased from 23.6 ± 10.4 s to 2.7 ± 1.1 s and from 5.3 ± 2.1 s to 1.0 ± 0.5 s, respectively, as the concentration of TBAI increased from 1 to 10 μg/mL (2.7 to 27.0 μmol/L).

Monte Carlo model for asymmetric anion exchange: We reasoned that the asymmetric behavior observed in both ensemble and single-particle fluorescence studies arises from differences in the reaction path during anion exchange in opposite directions. To support this hypothesis, we used Monte Carlo trajectories to simulate anion exchange in individual particles and their waiting and switching times (see the **Experimental** section **2.2** for further details). In these simulations, differences in the reaction path are reflected in the way the probability for each exchange event in a particle evolves with the number of previous successful events. The incorporation of positive cooperativity where previous events make future ones more probable produces sharp transitions for individual particles to transform along with a distribution of waiting times.[39-42] We find that

the degree of cooperativity or how much the probability changes with each previous event controls the sharpness of transitions (i.e., the switching times) as well as the concentration dependence of waiting and switching times.

2.4 Model for asymmetry in anion exchange

The waiting and switching times for the transformation of as-synthesized $CsPbBr_3$ NCs to $CsPbI_3$ (as well as the back conversion of mixed-halide $CsPbBr_{3-x}I_x$ NCs) closely resemble our previous work on anion exchange between $CsPbCl_3$ and $CsPbBr_3$ NCs.[42] In this previous study, we showed that the concentration dependence of waiting and switching times for highly miscible systems can be reproduced when the probability gradually increases with the number of successive exchange events. The black traces in **Figure 2.5(a)** and **2.5(b)** show the simulated changes in free energy and associated probability of exchange events for this exchange-density model in which the change in free energy for anion exchange in a particle is proportional to the density of exchanged ions. The concave downward curvature for the change in free energy leads to a gradual increase in probability with successive exchange events. Changes in the concentration of substitutional anions were simulated by varying the initial probability. We varied the simulated concentration over a similar range to the experimental variations in concentration (in μg/mL of TBAI/TBAB) shown in **Figure 2.4**. The simulated concentration dependencies of waiting and switching times for the exchange-density model and corresponding experimental times for the back conversion of bromide-rich $CsPbBr_{3-x}I_x$ NCs to $CsPbI_3$ are shown in **Figures 2.5(c)** and **2.5(d)** (black traces). We use this sample for comparison as it will have nearly the same size distribution as the as-synthesized $CsPbI_3$ NCs that were used to prepare it. Based on the similarities in experimental waiting and switching times shown in **Figure 2.4**, this model also applies to the conversion of as-synthesized $CsPbBr_3$ NCs to $CsPbI_3$ and the back conversion of iodide-rich $CsPbBr_{3-x}I_x$ NCs to $CsPbBr_3$. The exchange-density model reproduces the longer waiting and switching times for these samples (see **Figure 2.22**) as well as their steeper dependence on concentration (at low concentrations of substitutional anion) relative to the conversion of $CsPbI_3$

NCs to $CsPbBr_3$ described below. Furthermore, both the exchange-density model and the experimental values for the back conversion of bromide-rich $CsPbBr_{3-x}I_x$ NCs to $CsPbI_3$ show a linear correlation between the waiting and switching times of individual particles. As shown in **Figure 2.23(a)** and **2.23(b)**, particles with longer waiting times are more likely to have longer switching times. Linear fits to the distribution of waiting and switching times for individual particles give average slopes of 0.15 ± 0.01 (average ± 1st standard deviation for different concentrations) for the exchange-density model and 0.11 ± 0.03 for the experimental results (see **Figure 2.24** and **Table 2.5** for details). This correlation occurs because the slower rises in intensity for individual particles (especially at lower concentrations of TBAI) lead to an overlap between the measurements of waiting and switching times.

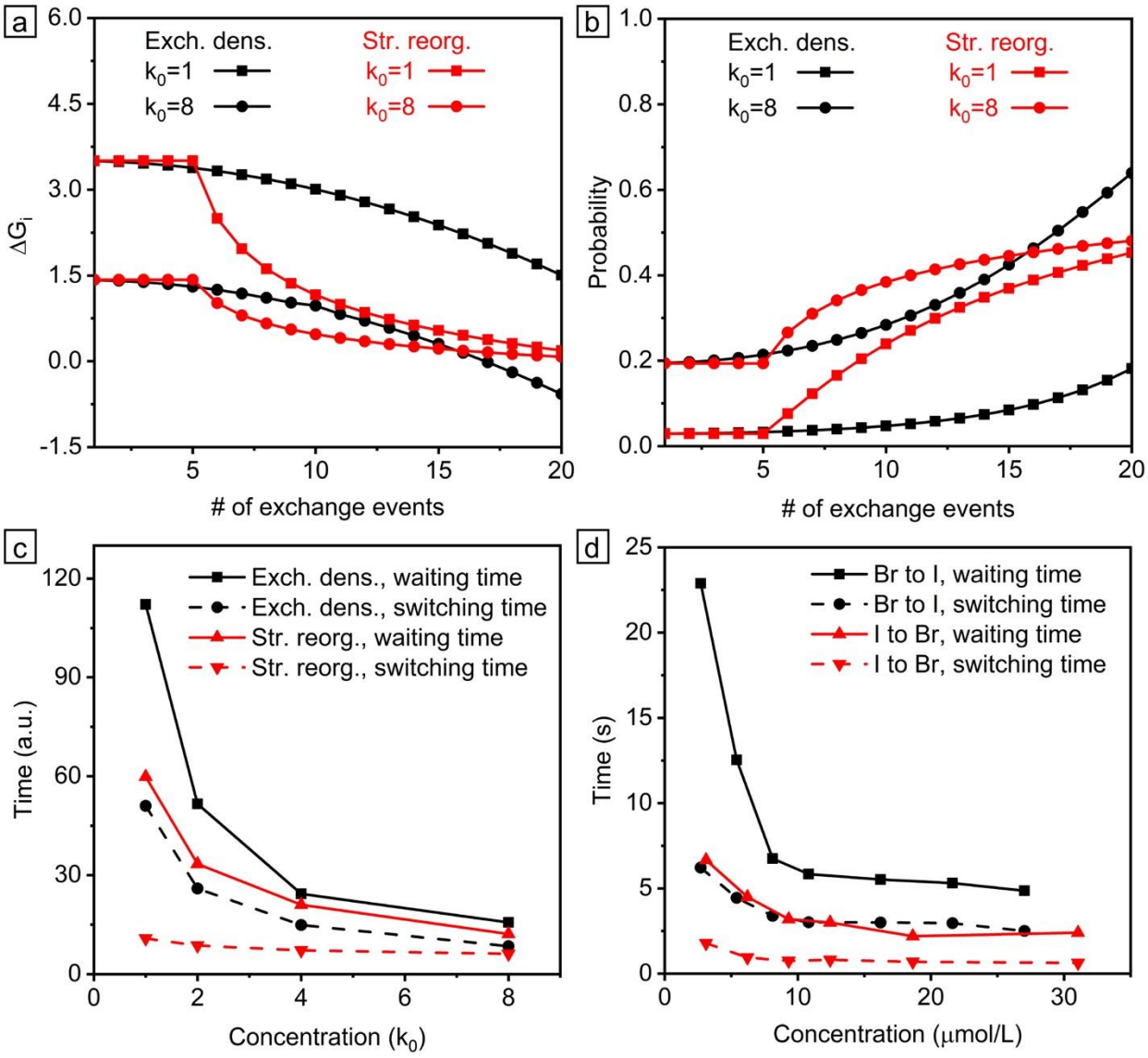

Figure 2.5. (a) Change in free energy, ΔG_i, with the number of exchange events, i, in a particle for the exchange-density (Exch. dens., black traces) and structural-reorganization (Str. reorg., red traces) models. In each model, a constant term added to the total free energy, ΔG_1, was varied to simulate the effect of concentration. Plots for the minimum (i.e., $k_0 = 1$, squares) and maximum (i.e., $k_0 = 8$, circles) concentrations simulated are shown. (b) The associated probability of exchange for the models shown in (a). (c) Simulated waiting and switching times for the two models as a function of k_0. (d) Experimental waiting and switching times for the conversion of as-

synthesized $CsPbI_3$ NCs to $CsPbBr_3$ (red traces) and the back-conversion of bromide-rich $CsPbBr_{3-x}I_x$ NCs to $CsPbI_3$ (black traces).

Previous work from our group and that of Routzahn and Jain has shown that the waiting and switching times for the transformation of immiscible crystal pairs (e.g., $CdSe/Ag_2Se$ and $PbBr_2/CH_3NH_3PbBr_3$) that require a substantial reorganization in structure can be reproduced by incorporating an abrupt increase in probability during the Monte Carlo trajectories.[39-41] For example, in our previous model used to describe the intercalation of CH_3NH_3Br into $PbBr_2$ NCs in which a new phase must nucleate in each particle, the initial reaction events have equal probability. However, after a critical number of events have taken place in a particle, the free energy change associated with each successive event abruptly decreases and the associated probability increases. The conversion of as-synthesized $CsPbI_3$ NCs to $CsPbBr_3$ studied here appears to be an intermediate case between the fully miscible and fully immiscible systems that have been previously modeled. While the transformation of $CsPbI_3$ NCs does not require a distinct phase change, it likely involves a coordinated reorganization of the tilt angles of corner-sharing PbX_6 octahedra (discussed in more detail below). Thus, we adapted our previous model to the conversion of $CsPbI_3$ NCs to $CsPbBr_3$ by adjusting the curvature in free energy after the threshold such that the change in probability was less abrupt. The red traces in **Figure 2.5(a)** and **2.5(b)** show the simulated changes in free energy and probability for exchange events using this structural-reorganization model. The initial events have equal probability, but after a critical threshold (5 in these simulations), the free energy change associated with each successive event decreases and the probability increases. The concave upward curvature for the change in free energy with reaction events after the threshold (and concave downward curvature of the probability)

leads to a change in probability that successfully models the sharper switching times for this transformation (**Figure 2.22**). The simulated concentration dependencies of waiting and switching times for the structural-reorganization model and corresponding experimental times for the conversion of $CsPbI_3$ NCs to $CsPbBr_3$ are shown in **Figures 2.5(c)** and **2.5(d)** (red traces). The structural-reorganization model reproduces both the shorter waiting and switching times seen experimentally for this transformation and their relative insensitivity to concentration. The larger structural reorganization needed during the conversion of $CsPbI_3$ NCs to $CsPbBr_3$ also leads to greater temporal separation between the waiting and switching times. In both the Monte Carlo simulations using the structural-reorganization model and the experimental values for the conversion of $CsPbI_3$ NCs to $CsPbBr_3$, there is no correlation between these values at low concentrations (**Figure 2.23(c)** and **2.23(d)**). However, at the highest simulated concentration, the change in free energy and probability for exchange events in the two models are similar (see the traces marked with circles in **Figure 2.5(a)** and **2.5(b)**). Consequently, the respective waiting and switching times for the two models also have more similar mean values at the highest simulated concentration (**Figure 2.5(c)**) in agreement with the experimental results (**Figure 2.5(d)**).

Our single-particle fluorescence studies supported by Monte Carlo simulations reveal that $CsPbI_3$ nanocrystals synthesized by the hot-injection method undergo an abrupt structural reorganization as they transform to $CsPbBr_3$. We postulate this structural reorganization involves coordinated changes in the titling patterns of PbX_6 octahedra. The in-plane and out-of-plane tilt angles of PbX_6 octahedra are different in bulk $CsPbBr_3$ and $CsPbI_3$ with the perovskite orthorhombic γ structure due to the different radii of Br^- (1.82 Å) and I^- (2.06 Å) anions (see **Table 2.6**). $CsPbBr_3$ and $CsPbI_3$ NCs also show differences in their octahedral tilting patterns.[12, 27, 48] Furthermore, Zhao and coworkers recently reported size-dependent structural variations in size-

selected $CsPbI_3$ NCs with the orthorhombic γ phase for edge lengths up to 15.3 nm that arise from surface strain.[29] Rietveld refinement of powder XRD patterns indicated there were variations in the octahedral tilt angles as a function of NC size.[29] While the size distributions of our $CsPbX_3$ samples are too broad to perform Rietveld refinement and measure changes in the octahedral tilt angles, the mean size of our initial $CsPbI_3$ NCs (11.9 nm) falls within the range where surface strain is expected to induce changes to their structure. Thus, the octahedral tilt angles likely change during anion exchange both due to differences in bulk structure along with the different surface energies associated with $CsPbBr_3$ and $CsPbI_3$.[49-51]

A more abrupt structural reorganization during the conversion of the as-synthesized $CsPbI_3$ NCs to $CsPbBr_3$ is consistent with the narrower distributions of waiting and switching times observed for this transformation (see **Figures 2.21** and **2.23**). This structural reorganization also explains the peak splitting observed in ensemble PL spectra during the conversion of $CsPbI_3$ NCs to $CsPbBr_3$. The interconversion between the two distinct populations of iodide-rich and bromide-rich $CsPbBr_{3-x}I_x$ NCs likely coincides with the reordering of the PbX_6 octahedra. On the other hand, $CsPbBr_3$ NCs undergo a smooth transition to $CsPbI_3$ indicating that the tilting pattern of the initial $CsPbBr_3$ NCs is largely conserved during their transformation. This smooth transition leads to longer waiting and switching times with a wider distribution at low concentrations of substitutional anion. Furthermore, $CsPbBr_{3-x}I_x$ nanocrystals that have already undergone anion exchange possess similar mean waiting and switching times to those of the as-synthesized $CsPbBr_3$ NCs undergoing exchange to $CsPbI_3$. This indicates that when bromide-rich $CsPbBr_{3-x}I_x$ NCs produced by anion exchange of $CsPbI_3$ are converted back to $CsPbI_3$ they retain a structure similar to the $CsPbBr_3$ NCs. Thus, we propose that anion exchange between as-synthesized $CsPbBr_3$ and

$CsPbI_3$ NCs is not reversible and that $CsPbI_3$ NCs produced by anion exchange do not have the same structure as those produced by hot-injection.

2.5 Conclusions

In summary, we used single-particle fluorescence to elucidate asymmetric chemical reactivity during anion exchange between $CsPbBr_3$ and $CsPbI_3$ nanocrystals. We attribute shorter reaction times for individual $CsPbI_3$ NCs along with a narrower distribution to a more abrupt structural reorganization needed as they transform to $CsPbBr_3$. $CsPbBr_3$ NCs do not undergo this structural reorganization as they transform to $CsPbI_3$ leading to a wider distribution of reaction times. Our study indicates that subtle structural differences between $CsPbX_3$ nanocrystals that are difficult to detect by conventional powder x-ray diffraction can have a significant impact on their chemical reactivity. X-ray total scattering measurements using synchrotron radiation could be used in the future to quantify differences in the structure of $CsPbI_3$ NCs made by the hot-injection method vs. by anion exchange.[27, 28, 52] While our studies were performed under dilute conditions (i.e., isolated nanocrystals dispersed on a substrate), the distribution of reaction times may affect the compositional homogeneity of $CsPbX_3$ NCs produced by anion exchange at higher concentrations, which will be needed to scale-up this reaction. If the local concentration of substitutional anions becomes depleted, then NCs with longer waiting times will incorporate a lower fraction of the substitutional anion. This inherent distribution of reaction times, which is controlled by the degree of structural reorganization during the nanocrystal transformation, is important to consider when developing scaled-up fabrication routes that maximize the color purity of luminescent $CsPbX_3$ nanocrystals for optoelectronic devices.

2.6 Appendix A

2.6.1 Tables

Table 2.1. Additional details for the fluorescence spectra shown in **Figure 2.1(a)** (i.e., transformation of $CsPbBr_3$ NCs to $CsPbI_3$): amount of TBAI added, the emission maximum of the resulting PL spectrum, and its FWHM.

Total volume of TBAI (μL)	Total moles of TBAI (μmole)	Peak maximum (nm)	Peak maximum (eV)	FWHM (nm)	FWHM (eV)
0	0	502	2.47	24	0.13
80	0.06	537	2.31	28	0.12
160	0.13	559	2.22	35	0.12
240	0.19	608	2.04	37	0.12
320	0.26	633	1.96	36	0.12
400	0.32	643	1.93	37	0.11

Table 2.2. Additional details for the fluorescence spectra shown in **Figure 2.1(b)** (i.e., transformation of $CsPbI_3$ NCs to $CsPbBr_3$): amount of TBAB added, the emission maximum of the resulting PL spectrum, and its FWHM.

Total volume of TBAB (μL)	Total moles of TBAI (μmole)	Peak maximum (nm)	Peak maximum (eV)	FWHM (nm)	FWHM (eV)
0	0	674	1.84	40	0.11
60	0.06	674	1.84	44	0.12
120	0.11	547	2.27	27	0.11
180	0.17	533	2.33	29	0.13
300	0.28	524	2.37	24	0.11
420	0.39	519	2.39	23	0.11

Table 2.3. The $CsPbBr_3$ and $CsPbI_3$ NCs samples characterized in figures.

		Sample characterized in the following figures
$CsPbBr_3$	Batch 1	**Figure 2.1(a), Figure 2.2(b, c), Figure 2.3(a), Figure 2.4(a), Figure 2.14(a), Figure 2.17, Figure 2.21(a)**
	Batch 2	**Figure 2.4(b), Figure 2.7(a, b), Figure 2.8(a, b), Figure 2.9, Figure 2.10, Figure 2.14(b), Figure 2.18, Figure 2.21(b)**
$CsPbI_3$	Batch 1	**Figure 2.1(b, c), Figure 2.2(d, e), Figure 2.3(b), Figure 2.4(c, d), Figure 2.5(d), Figure 2.6, Figure 2.12, Figure 2.13, Figure 2.14(c, d), Figure 2.15, Figure 2.16, Figure 2.19, Figure 2.20, Figure 2.21(c, d), Figure 2.23(a, c), Figure 2.24**
	Batch 2	**Figure 2.7(c, d), Figure 2.8(c, d), Figure 2.9, Figure 2.10**

Table 2.4. Fitting parameters for the concentration dependence of the mean waiting and switching times shown in **Figure 2.4**.

y = a/x + b		**Figure 2.4(a):** $CsPbBr_3$ to $CsPbI_3$	**Figure 2.4(b):** $CsPbBr_{3-x}I_x$ to $CsPbBr_3$	**Figure 2.4(c):** $CsPbI_3$ to $CsPbBr_3$	**Figure 2.4(d):** $CsPbBr_{3-x}I_x$ to $CsPbI_3$
Waiting time	a (s-μg/mL)	16.3	5.1	26.5	20.5
	b (s)	2.6	1.6	2.8	2.9
Switching time	a (s-μg/mL)	4.0	1.2	4.5	6.3
	b (s)	2.2	0.47	0.3	0.8

Table 2.5. Parameters for the linear fits (y = ax + b) of the scatter plots of waiting vs. switching time shown in **Figure 2.23**.

Exchange-density model	k_0	1	2	4	8		
	a (slope)	0.15	0.14	0.17	0.15		
	b (intercept)	18634	10397	5479	3872		
$CsPbBr_{3-x}I_x$ to $CsPbI_3$	TBAI conc. (μg/mL)	1	2	3	4	6	10
	a (slope)	0.15	0.11	0.12	0.09	0.059	0.11
	b (intercept)	14.1	4.5	3.82	5.95	1.99	3.48

Table 2.6. Tilt angles of PbX_6 octahedra (X = Br or I) based on the bulk crystal structures from ICSD collection codes #243735 for $CsPbBr_3$ and #21955 for $CsPbI_3$. Both crystals have the perovskite orthorhombic γ phase.

Tilt angle	$CsPbBr_3$	$CsPbI_3$
In-plane Pb–X–Pb	156.51°	155.57°
Out-of-plane Pb–X–Pb	163.79°	159.24°

2.6.2 Figures

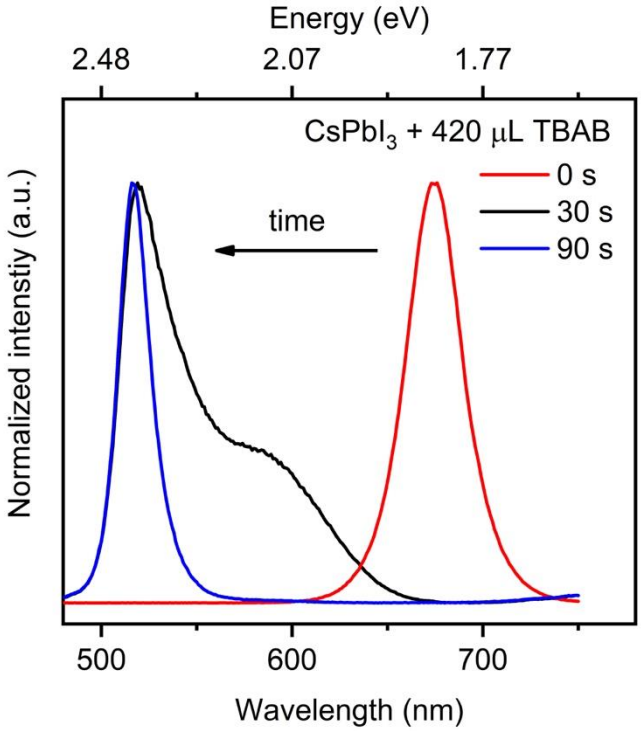

Figure 2.6. Normalized PL spectra of $CsPbI_3$ NCs before (red trace) and after (black and blue traces) adding 420 μL of a TBAB solution (0.3 mg/mL = 0.93 mmol/L) in tert-butanol. The PL spectra were measured 30 s (black trace) and 90 s (blue trace) after the addition of TBAB. The spectra stopped blue-shifting approximately 90 s after the addition of TBAB. The excitation wavelength was 400 nm for all spectra. **Figure 2.1** shows the resulting PL spectra when 60-μL aliquots of the same TBAB solution were added, and a spectrum was taken between each aliquot.

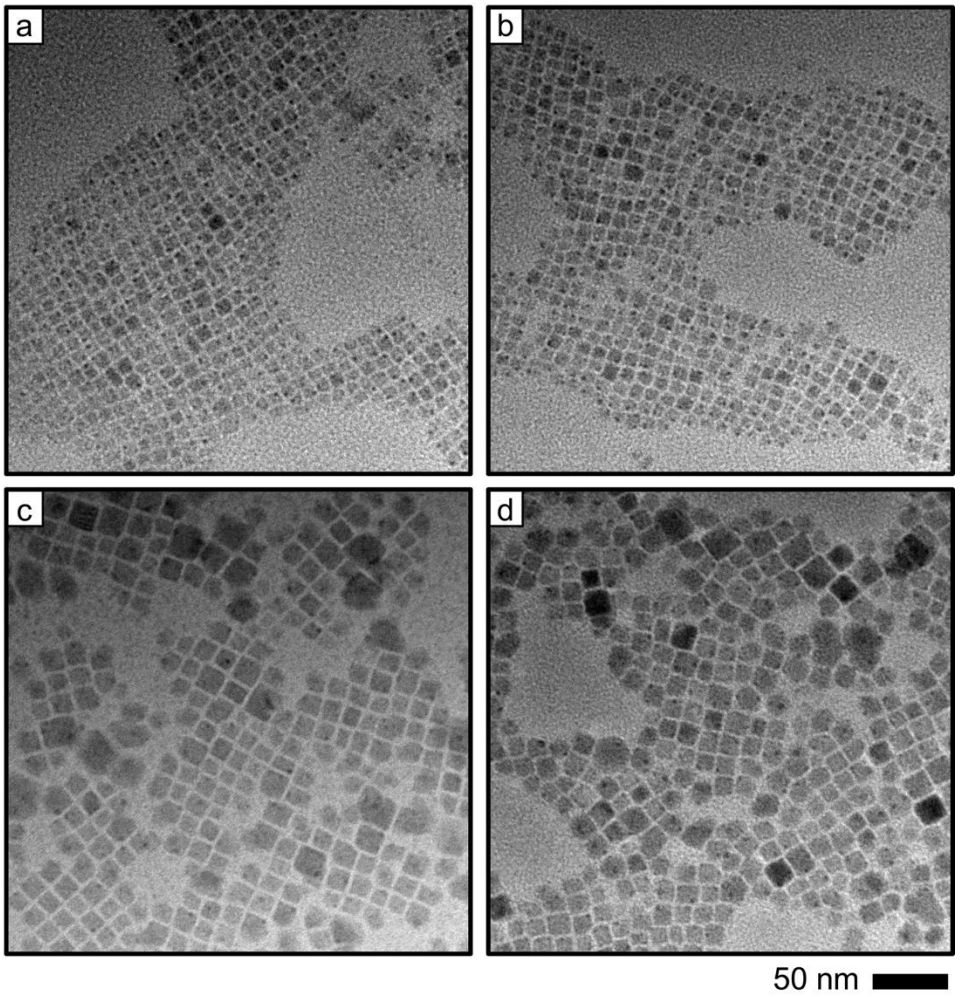

Figure 2.7. Bright-field TEM images of $CsPbX_3$ NCs before and after anion exchange. (a) As-synthesized $CsPbBr_3$ NCs. (b) $CsPbI_3$ NCs produced by anion exchange of $CsPbBr_3$ NCs on a TEM grid. (c) As-synthesized $CsPbI_3$ NCs. (d) $CsPbBr_3$ NCs produced by anion exchange of $CsPbI_3$ NCs on a TEM grid.

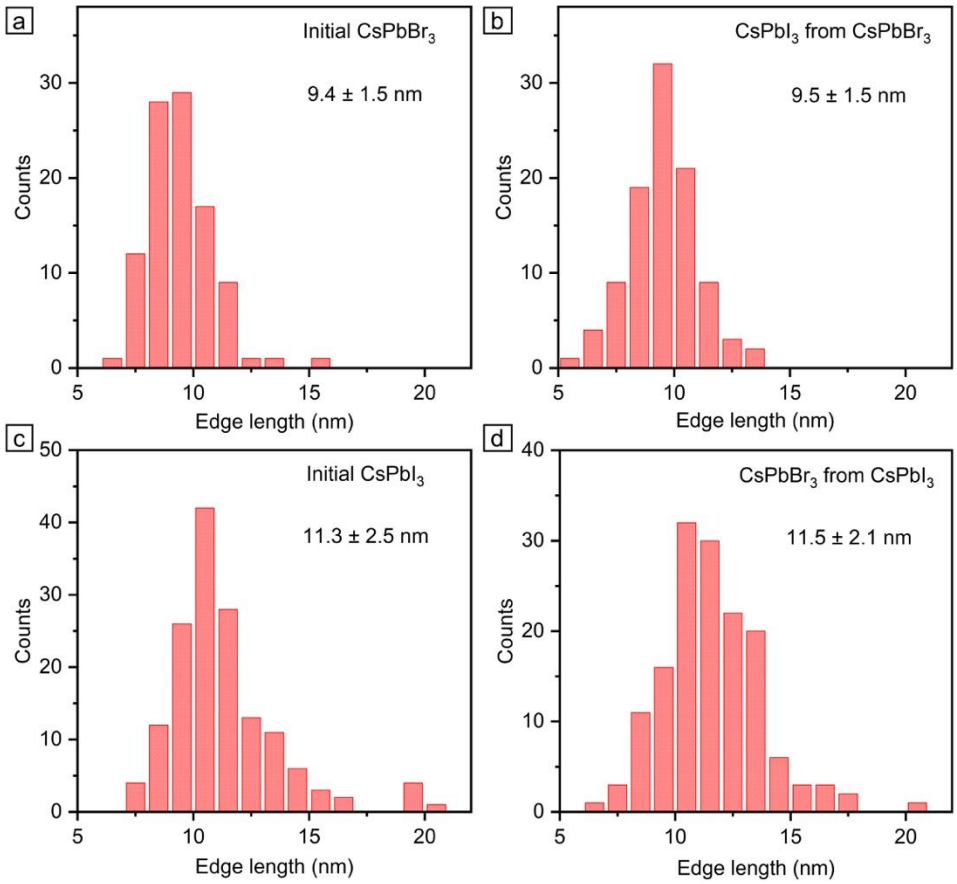

Figure 2.8. Size distributions of the $CsPbX_3$ NCs shown in **Figure 2.7**. (a) As-synthesized $CsPbBr_3$ NCs. (b) $CsPbI_3$ NCs produced by anion exchange of $CsPbBr_3$ NCs on a TEM grid. (c) As-synthesized $CsPbI_3$ NCs. (d) $CsPbBr_3$ NCs produced by anion exchange of $CsPbI_3$ NCs on a TEM grid. Based on the lattice constants of the bulk crystals, the distances between Pb atoms in $CsPbBr_3$ along the edges of the NCs are 8.250 Å in the (100) direction and 8.203 Å in the (001) direction. We assume the $CsPbBr_3$ NCs in **Figure 2.7** are oriented with the (010) plane parallel to the substrate similar to a previous report.[53] In bulk $CsPbI_3$, the distances between Pb atoms along the edges are 8.818 Å and 8.646 Å. The orientation of the unit cell is different in $CsPbI_3$. So, these Pb–Pb distances are along the (010) and (100) directions, respectively. When $CsPbBr_3$ NCs transform to $CsPbI_3$, the expected expansion of the lateral dimensions is 7% for the longer dimension and 5% for the shorter dimension, which lead to changes in the lateral dimensions of

less than 1 nm. A similar contraction of the lateral dimensions is expected when $CsPbI_3$ NCs transform to $CsPbBr_3$. However, these changes in size are less than the 1^{st} standard deviation in the size distribution of each sample. Thus, we do not observe a significant change in average edge length for either sample after anion exchange.

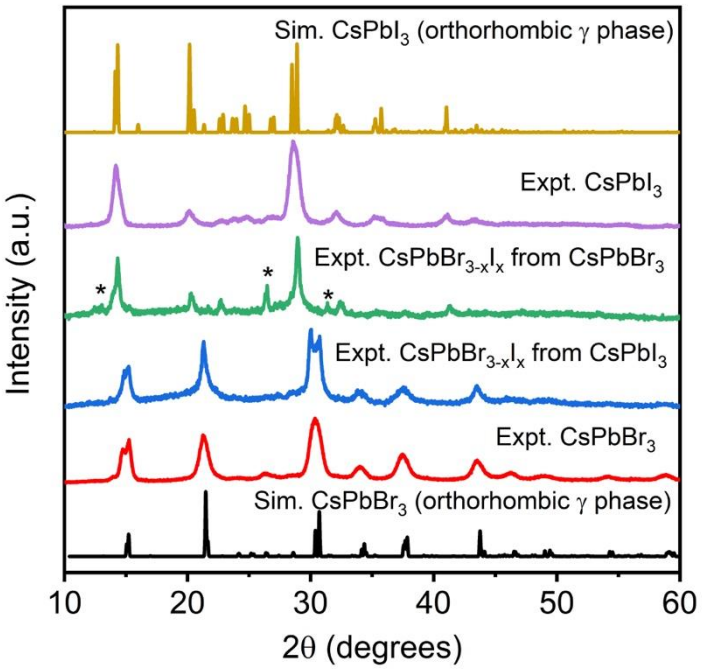

Figure 2.9. XRD patterns of $CsPbX_3$ NCs before and after anion exchange. From top to bottom the experimental patterns are the following: As-synthesized $CsPbI_3$ NCs (purple), iodide-rich $CsPbBr_{3-x}I_x$ NCs produced by anion exchange of $CsPbBr_3$ NCs (green), bromide-rich $CsPbBr_{3-x}I_x$ NCs produced by anion exchange of $CsPbI_3$ NCs (blue), and as-synthesized $CsPbBr_3$ NCs (red). Simulated powder XRD patterns made using ICSD collection codes #21955 for $CsPbI_3$ in the perovskite orthorhombic γ phase (yellow) and #243735 for $CsPbBr_3$ in the perovskite orthorhombic γ phase (black) are shown at the top and bottom of the plot. The peak positions in green pattern are shifted to higher angles compared to pure $CsPbI_3$, and the peak positions in the blue pattern are shifted to lower angles compared to pure $CsPbBr_3$ indicating that the NCs produced by anion exchange contain residual amounts of the parent anion. The sharper peaks following anion exchange in the green and blue patterns are likely the result of aggregation of the NCs leading to a larger average crystallite size. The impurity peaks marked with * in the green pattern are attributed to the non-perovskite orthorhombic δ phase of $CsPbI_3$.

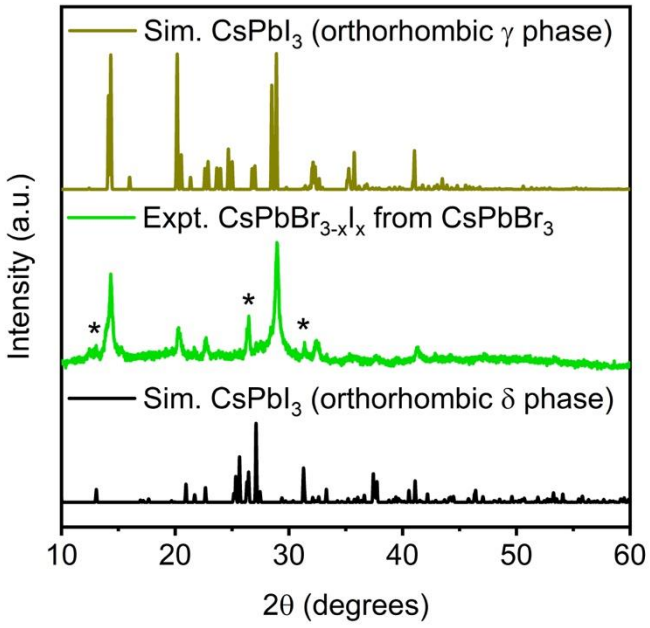

Figure 2.10. Comparison of the experimental XRD pattern for iodide-rich $CsPbBr_{3-x}I_x$ NCs produced by anion exchange of $CsPbBr_3$ NCs (middle, green) to simulated patterns for the perovskite orthorhombic γ phase of $CsPbI_3$ (top, yellow) and the non-perovskite orthorhombic δ phase (bottom, black). The simulated patterns were made using ICSD collection codes #21955 for the γ phase and #161480 for the δ phase. The impurity peaks marked with * are attributed to the non-perovskite δ phase of $CsPbI_3$, which results from degradation of the perovskite phase. While this impurity phase was detected in this sample, its formation may depend on the different preparation method for XRD analysis compared to fluorescence microscopy (i.e., samples for XRD were prepared at a higher concentration). Furthermore, as the δ phase of $CsPbI_3$ is not fluorescent, this impurity phase will not be detected in the fluorescence microscopy studies.

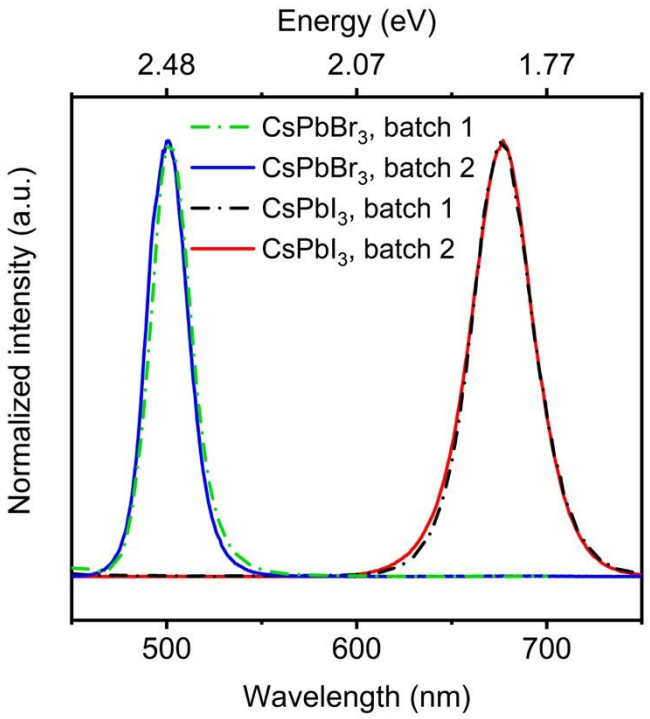

Figure 2.11. Normalized PL spectra of different batches of $CsPbBr_3$ (blue & green traces) and $CsPbI_3$ (red & black traces) NCs.

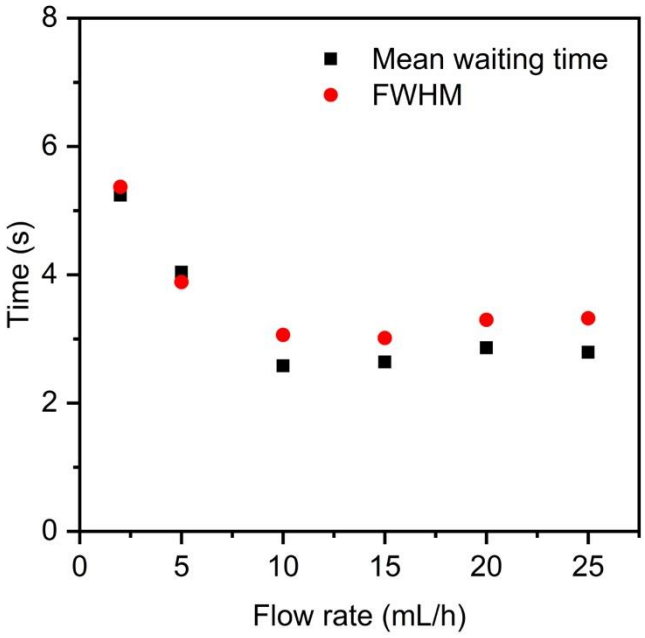

Figure 2.12. Comparison of the mean value (black squares) and the FWHM (red circles) of single-NC waiting times for the transformation of $CsPbI_3$ NCs to $CsPbBr_3$ measured using the same TBAB concentration (2 μg/mL, 6.2 μmol/L) introduced at different flow rates. The turn-on in emission of individual NCs was imaged with the green filter set (excitation window: 450 − 490 nm; emission window: 500 − 540 nm). The mean waiting time is independent of flow rate for flow rates between 10 and 25 mL/h.

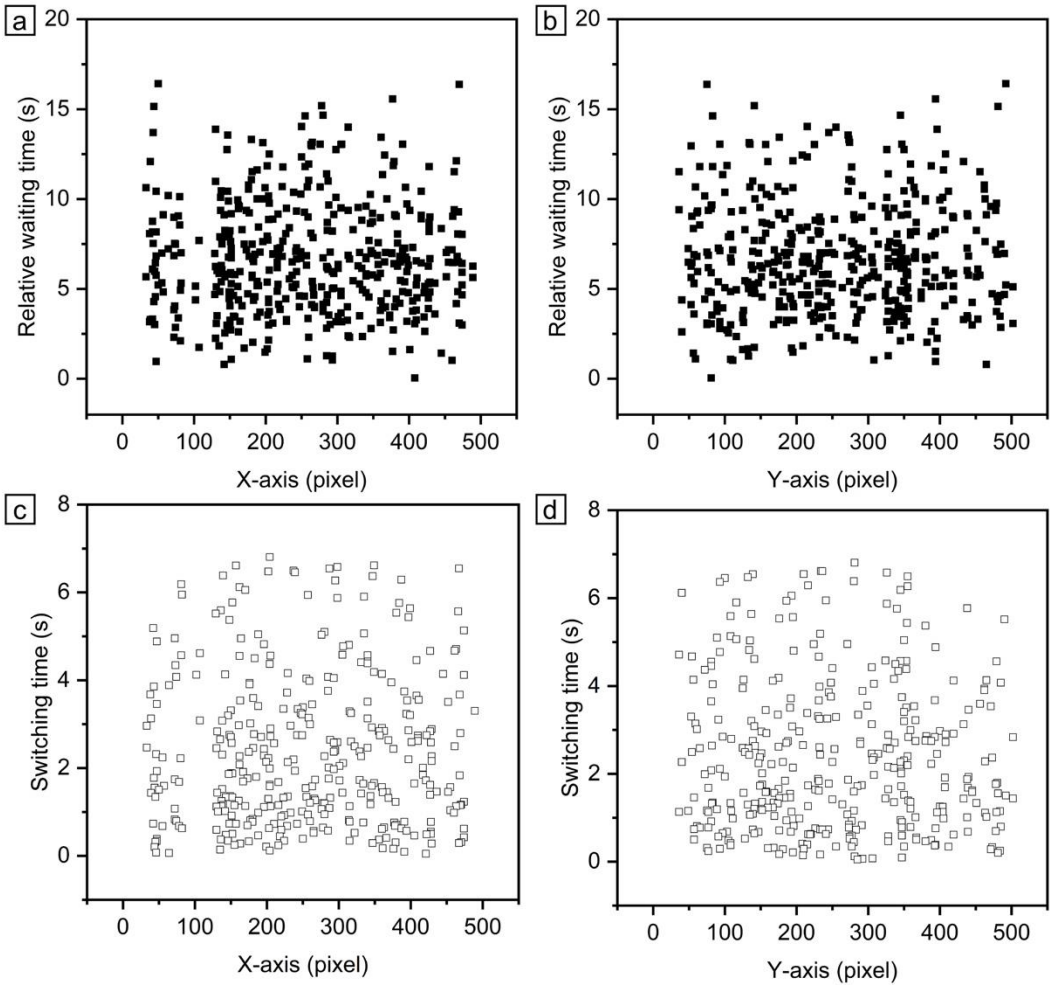

Figure 2.13. Waiting and switching times as a function of particle position for the transformation of $CsPbI_3$ NCs to $CsPbBr_3$ using a TBAB concentration of 1 μg/mL (3.1 μmol/L). The flow rate was 20 mL/h. (a, b) Waiting times for different NCs within the same field-of-view plotted vs. their pixel position along the (a) x-axis and (b) y-axis of the EMCCD camera. (c, d) Switching times for different NCs within the same field-of-view plotted vs. their pixel position along the (c) x-axis and (d) y-axis of the EMCCD camera.

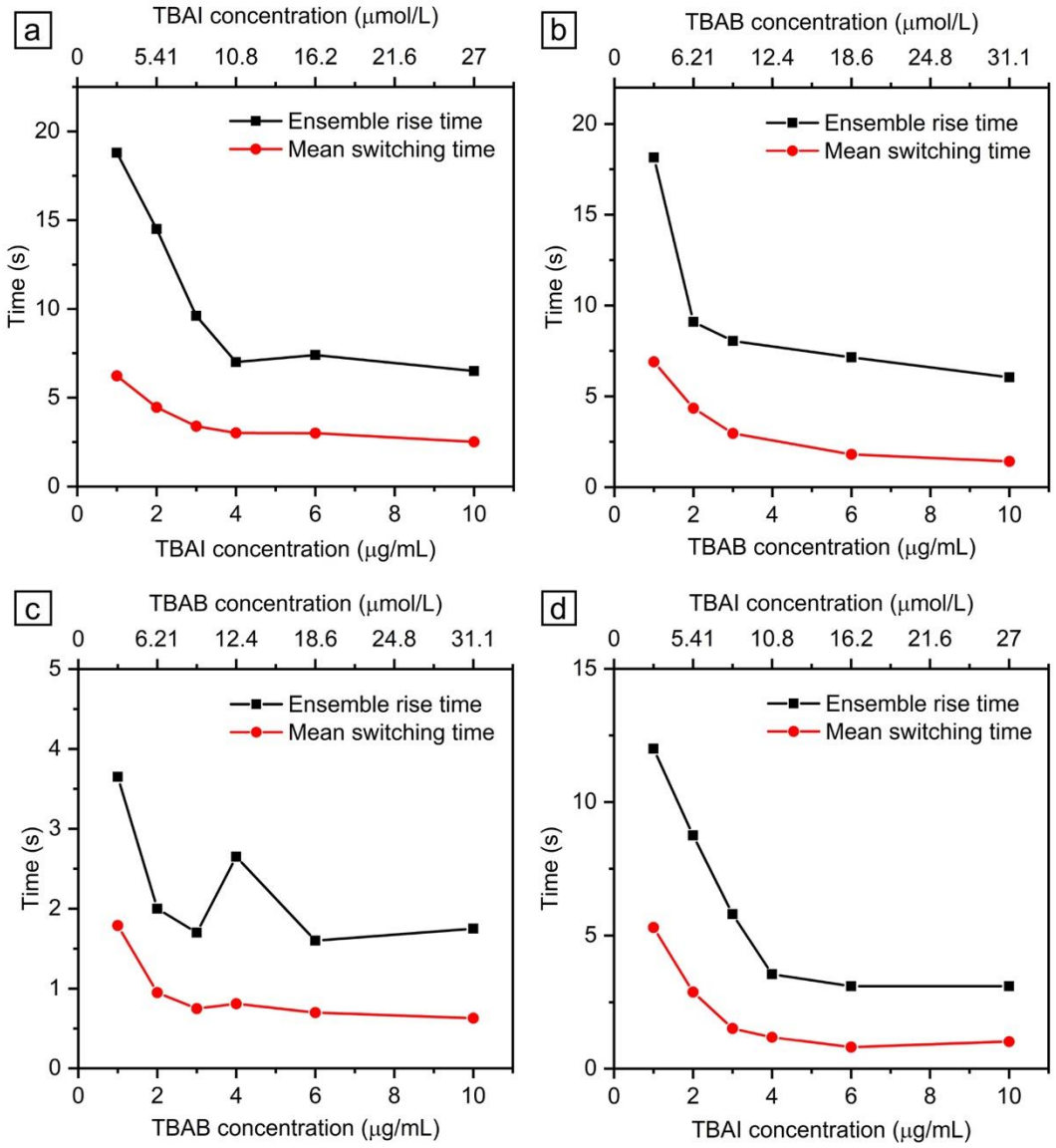

Figure 2.14. Comparison of the ensemble rise times in fluorescence intensity for all NCs in the field-of-view (black squares) to the mean of single-NC switching times (red circles) using different concentrations of TBAB or TBAI. (a) Transformation of as-synthesized $CsPbBr_3$ NCs to $CsPbI_3$. (b) Back conversion of iodide-rich $CsPbBr_{3-x}I_x$ NCs (prepared by anion exchange of $CsPbBr_3$ prior to imaging) to $CsPbBr_3$. (c) Transformation of as-synthesized $CsPbI_3$ NCs to $CsPbBr_3$. (d) Back conversion of bromide-rich $CsPbBr_{3-x}I_x$ NCs (prepared by anion exchange of $CsPbI_3$ prior to imaging) to $CsPbI_3$.

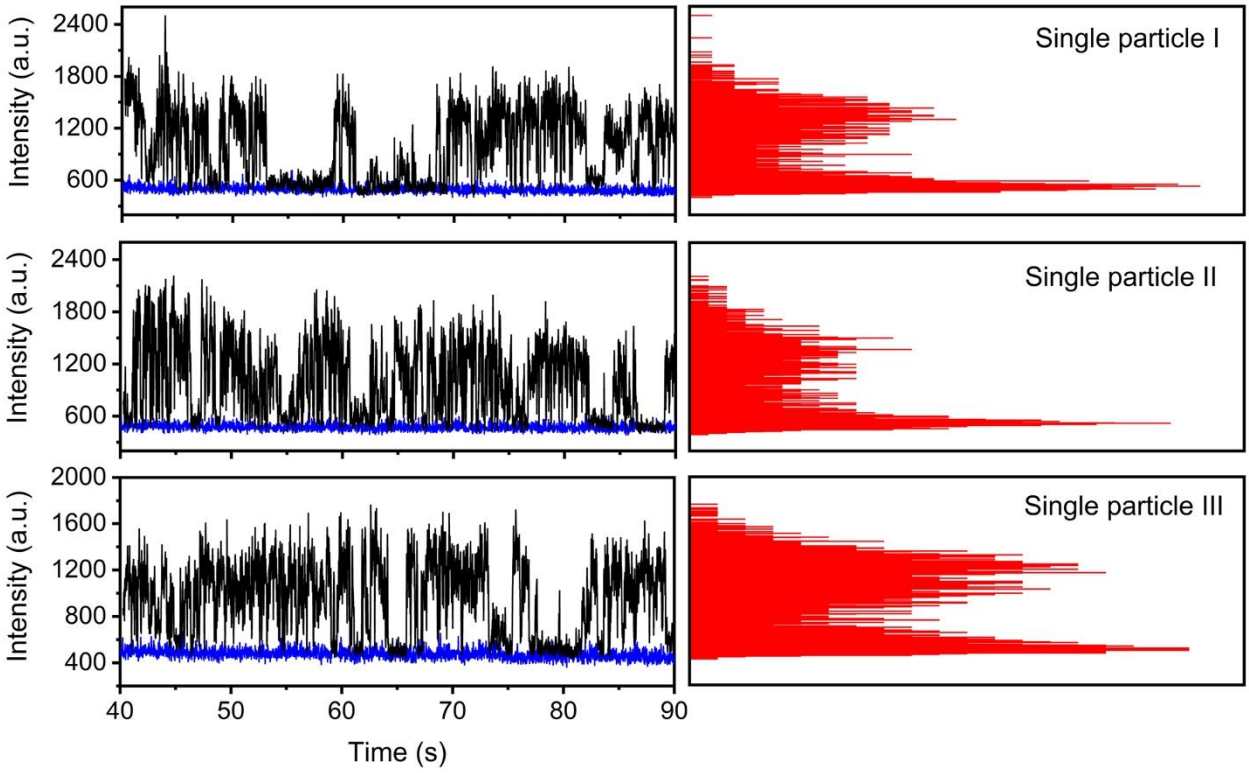

Figure 2.15. Representative intensity trajectories for single bromide-rich $CsPbBr_{3-x}I_x$ NCs following the transformation of $CsPbI_3$ NCs with a TBAB concentration of 1 μg/mL (3.1 μmol/L). Each of the black traces on the left-hand side is a segment of the trajectory after the intensity stopped increasing (i.e., following the exchange reaction). Each of the blue traces shows the background intensity in a nearby region not containing any particles. The red histograms on the right-hand side show the intensity distributions of the black traces. Intensity trajectories that exhibit fluorescence intermittency with a bimodal distribution of on and off states are indicative of single particles.

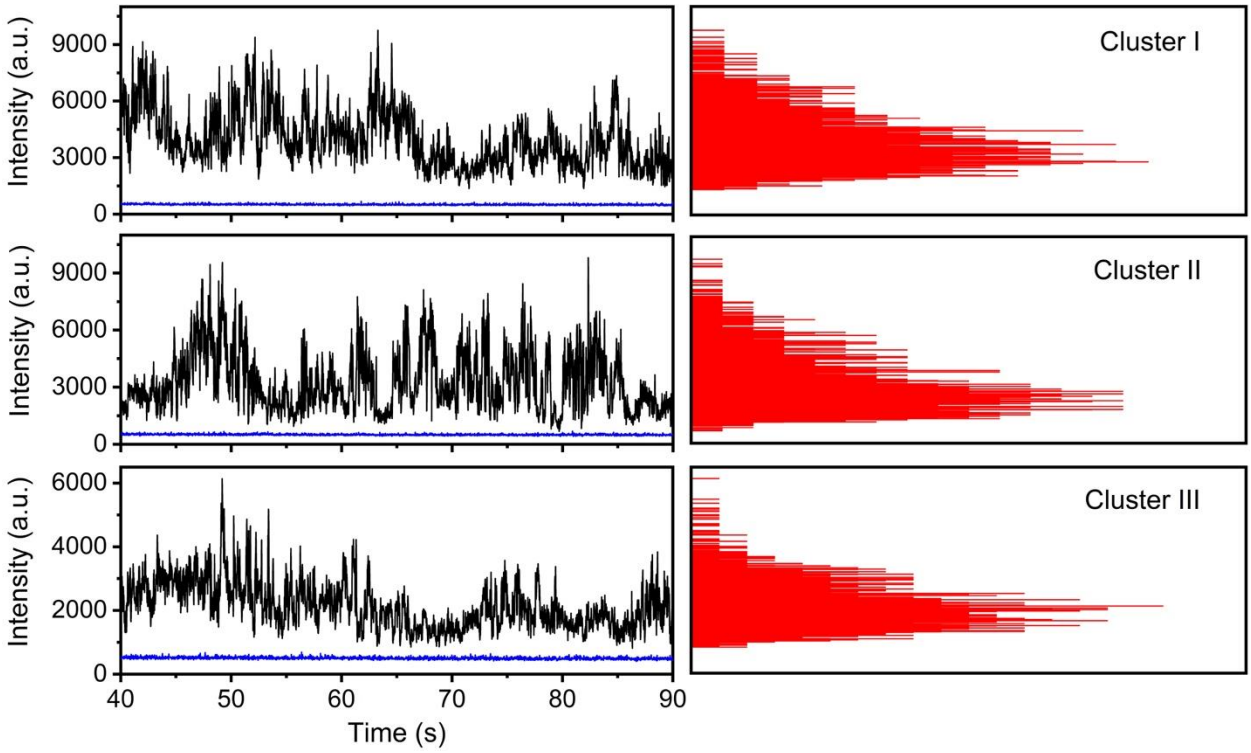

Figure 2.16. Representative intensity trajectories of clusters of $CsPbBr_{3-x}I_x$ NCs following the transformation $CsPbI_3$ NCs with a TBAB concentration of 1 μg/mL (3.1 μmol/L). Each of the black traces on the left-hand side is a segment of the trajectory after the intensity stopped increasing (i.e., following the exchange reaction). Each of the blue traces shows the background intensity in a nearby region not containing any particles. The red histograms on the right-hand side show the intensity distributions of the black traces. Unlike the trajectories for single particles shown in **Figure 2.15** above, clusters of particles do not show clear on and off states as each particle in the cluster blinks independently.

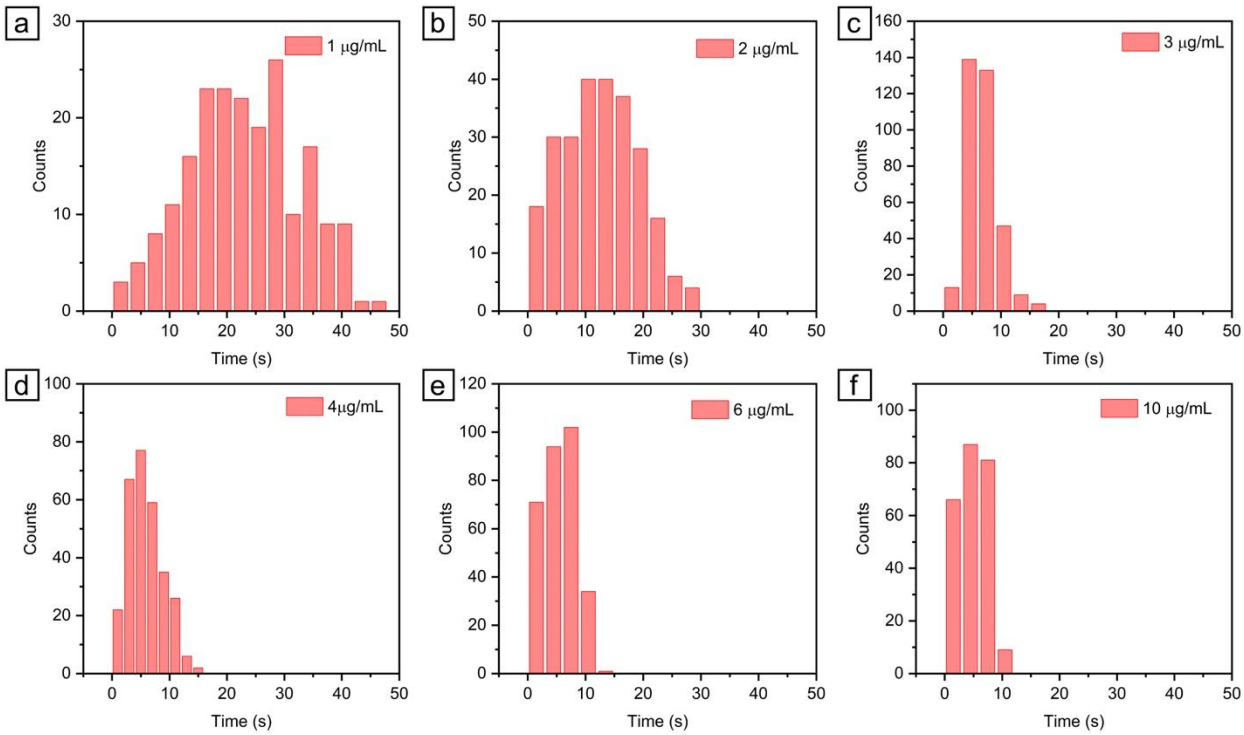

Figure 2.17. Histograms of the relative waiting times for the transformation of as-synthesized $CsPbBr_3$ NCs to $CsPbI_3$ using TBAI. The turn-on in emission of individual NCs was imaged with the red filter set (excitation window: 530 − 558 nm; emission window: 590 − 649 nm). The concentrations of TBAI used were (a) 1 μg/mL (2.7 μmol/L), (b) 2 μg/mL (5.4 μmol/L), (c) 3 μg/mL (8.1 μmol/L), (d) 4 μg/mL (10.8 μmol/L), (e) 6 μg/mL (16.2 μmol/L), and (f) 10 μg/mL (27 μmol/L). For each histogram, a relative waiting time of 0 seconds corresponds to the first NC to transform among the population.

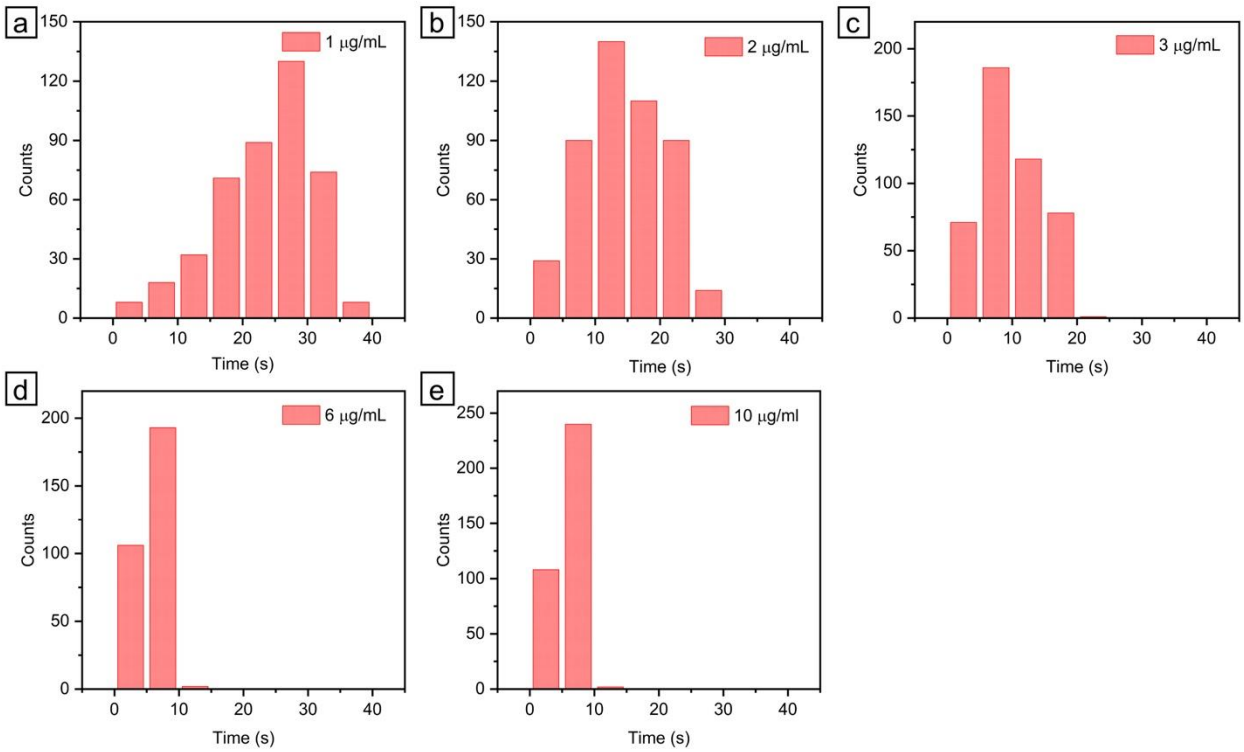

Figure 2.18. Histograms of the relative waiting times for the back conversion of iodide-rich $CsPbBr_{3-x}I_x$ NCs to $CsPbBr_3$ using TBAB. The iodide-rich $CsPbBr_{3-x}I_x$ NCs were prepared by anion exchange of $CsPbBr_3$ NCs with PbI_2 in solution prior to imaging. The turn-off in emission of individual NCs was imaged with the red filter set (excitation window: 530 − 558 nm; emission window: 590 − 649 nm). The concentrations of TBAB used were (a) 1 μg/mL (3.1 μmol/L), (b) 2 μg/mL (6.2 μmol/L), (c) 3 μg/mL (9.3 μmol/L), (d) 6 μg/mL (18.6 μmol/L), and (e) 10 μg/mL (31.1 μmol/L). For each histogram, a relative waiting time of 0 seconds corresponds to the first NC to transform among the population.

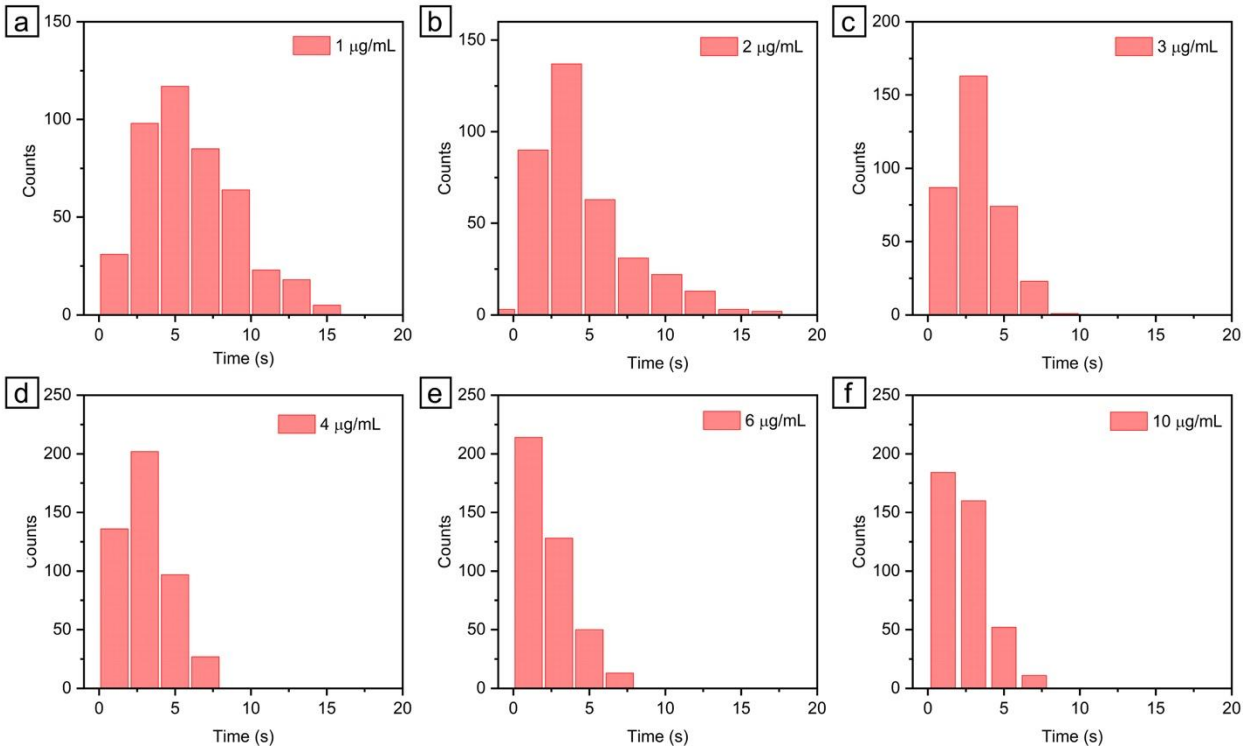

Figure 2.19. Histograms of the relative waiting times for the transformation of as-synthesized $CsPbI_3$ NCs to $CsPbBr_3$ using TBAB. The turn-on in emission of individual NCs was imaged with the green filter set (excitation window: 450 − 490 nm; emission window: 500 − 540 nm). The concentrations of TBAB used were (a) 1 μg/mL (3.1 μmol/L), (b) 2 μg/mL (6.2 μmol/L), (c) 3 μg/mL (9.3 μmol/L), (d) 4 μg/mL (12.4 μmol/L), (e) 6 μg/mL (18.6 μmol/L), and (f) 10 μg/mL (31.1 μmol/L). For each histogram, a relative waiting time of 0 seconds corresponds to the first NC to transform among the population.

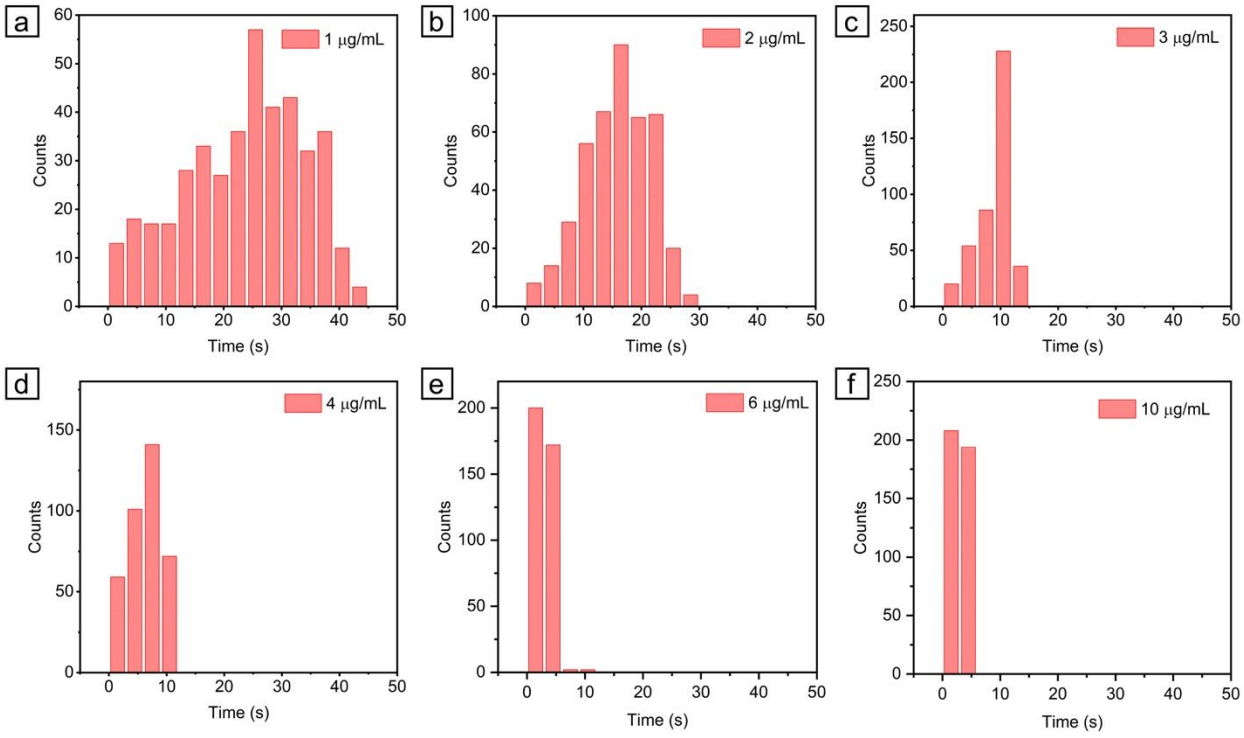

Figure 2.20. Histograms of the relative waiting times for the back conversion of bromide-rich $CsPbBr_{3-x}I_x$ NCs to $CsPbI_3$ using TBAI. The bromide-rich $CsPbBr_{3-x}I_x$ NCs were prepared by anion exchange of $CsPbI_3$ NCs on a coverslip using TBAB prior to imaging. The turn-off in emission of individual NCs was imaged with the green filter set (excitation window: 450 − 490 nm; emission window: 500 − 540 nm). The concentrations of TBAI used were (a) 1 μg/mL (2.7 μmol/L), (b) 2 μg/mL (5.4 μmol/L), (c) 3 μg/mL (8.1 μmol/L), (d) 4 μg/mL (10.8 μmol/L), (e) 6 μg/mL (16.2 μmol/L), and (f) 10 μg/mL (27 μmol/L). For each histogram, a relative waiting time of 0 seconds corresponds to the first NC to transform among the population.

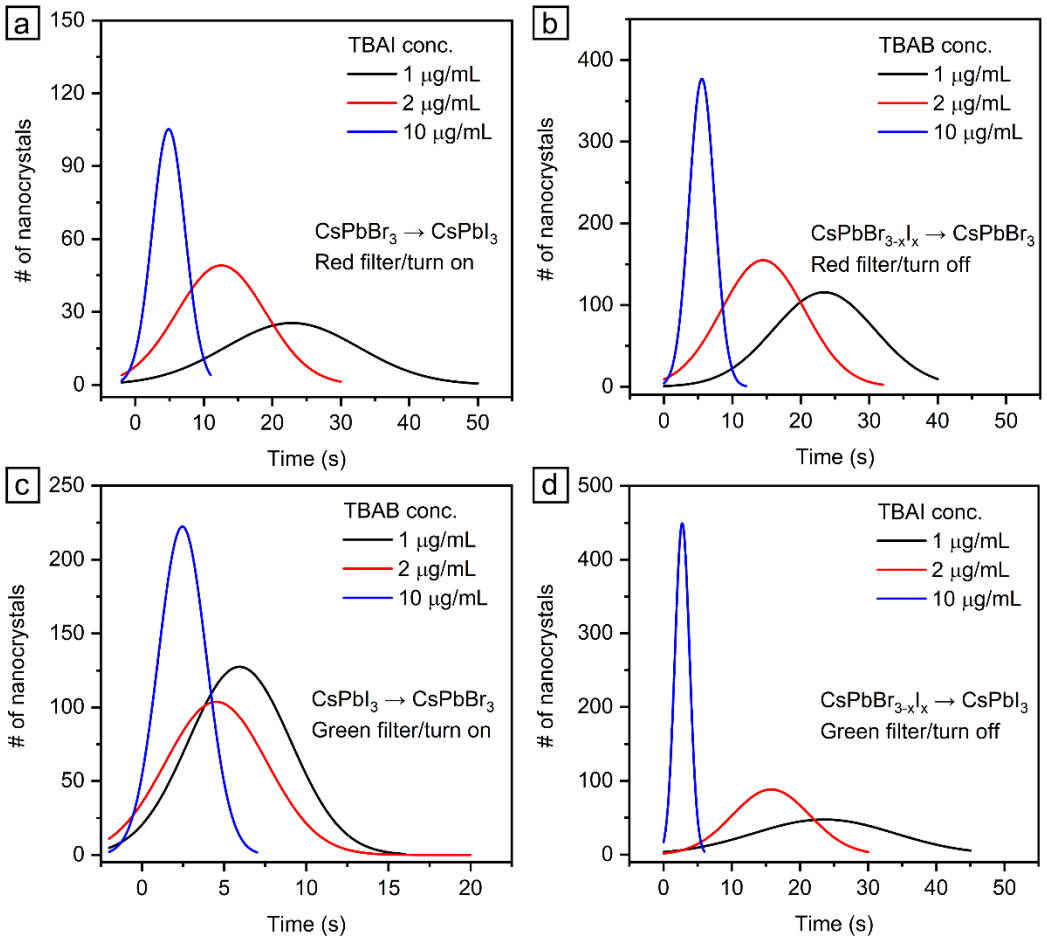

Figure 2.21. Examples of Gaussian fits to the distributions of relative waiting times shown above in **Figures 2.17 – 2.20** for single $CsPbX_3$ NCs undergoing anion exchange. (a) Transformation of as-synthesized $CsPbBr_3$ NCs to $CsPbI_3$ using TBAI (example fits to histograms in **Figure 2.17**). (b) Back conversion of iodide-rich $CsPbBr_{3-x}I_x$ NCs to $CsPbBr_3$ using TBAB (example fits to histograms in **Figure 2.18**). (c) Transformation of as-synthesized $CsPbI_3$ NCs to $CsPbBr_3$ using TBAB (example fits to histograms in **Figure 2.19**). (d) Back conversion of bromide-rich $CsPbBr_{3-x}I_x$ NCs to $CsPbI_3$ using TBAI (example fits to histograms in **Figure 2.20**). The concentrations of TBAI shown in (a) and (d) are 1, 2, and 10 μg/mL (i.e., 2.7, 5.4, and 27.0 μmol/L). The concentrations of TBAB shown in (b) and (c) are 1, 2, and 10 μg/mL (i.e., 3.1, 6.2, and 31.1 μmol/L).

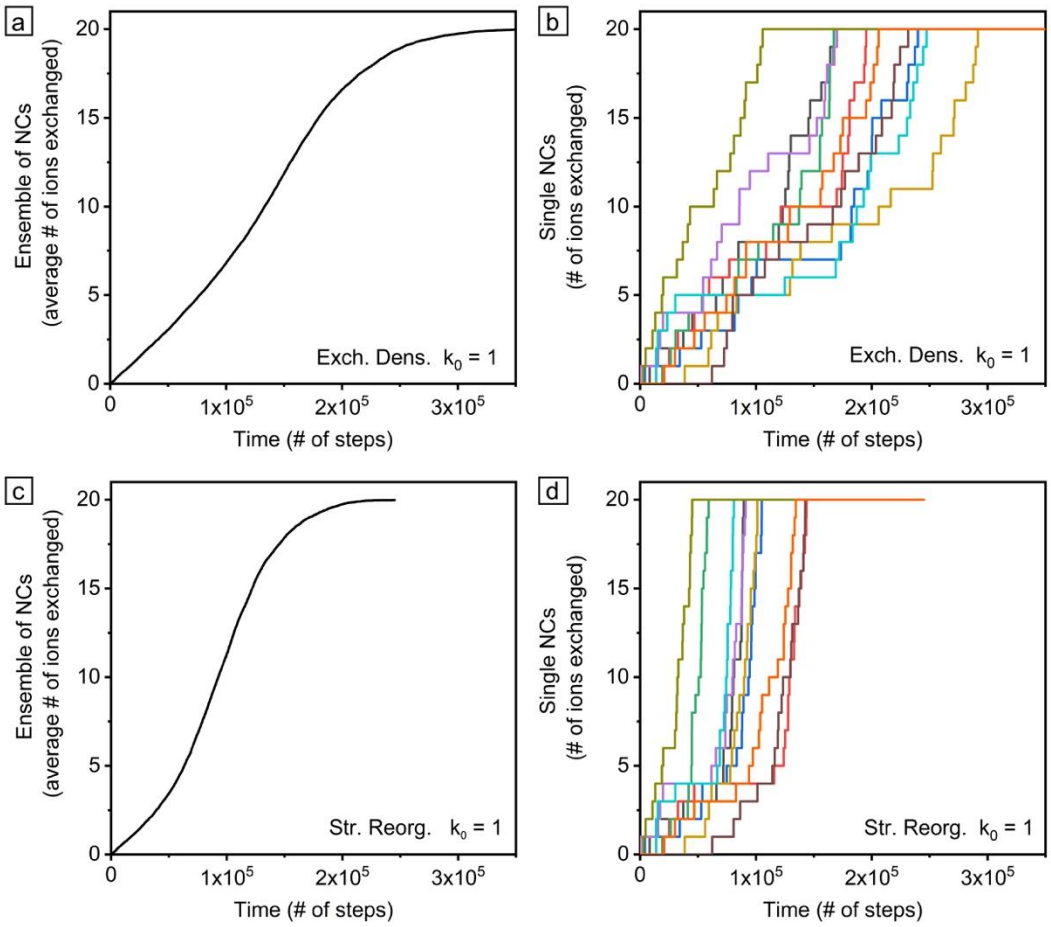

Figure 2.22. Simulated reaction trajectories for anion exchange. (a) Ensemble trajectory for the exchange-density model using a simulated concentration $k_0 = 1$. (b) Representative single-particle trajectories for the exchange-density model using $k_0 = 1$; (c) Ensemble trajectory for the structural-reorganization model using a simulated concentration $k_0 = 1$. (d) Representative single-particle trajectories for the structural-reorganization model using $k_0 = 1$. The structural-reorganization model leads to sharper transitions for individual particles

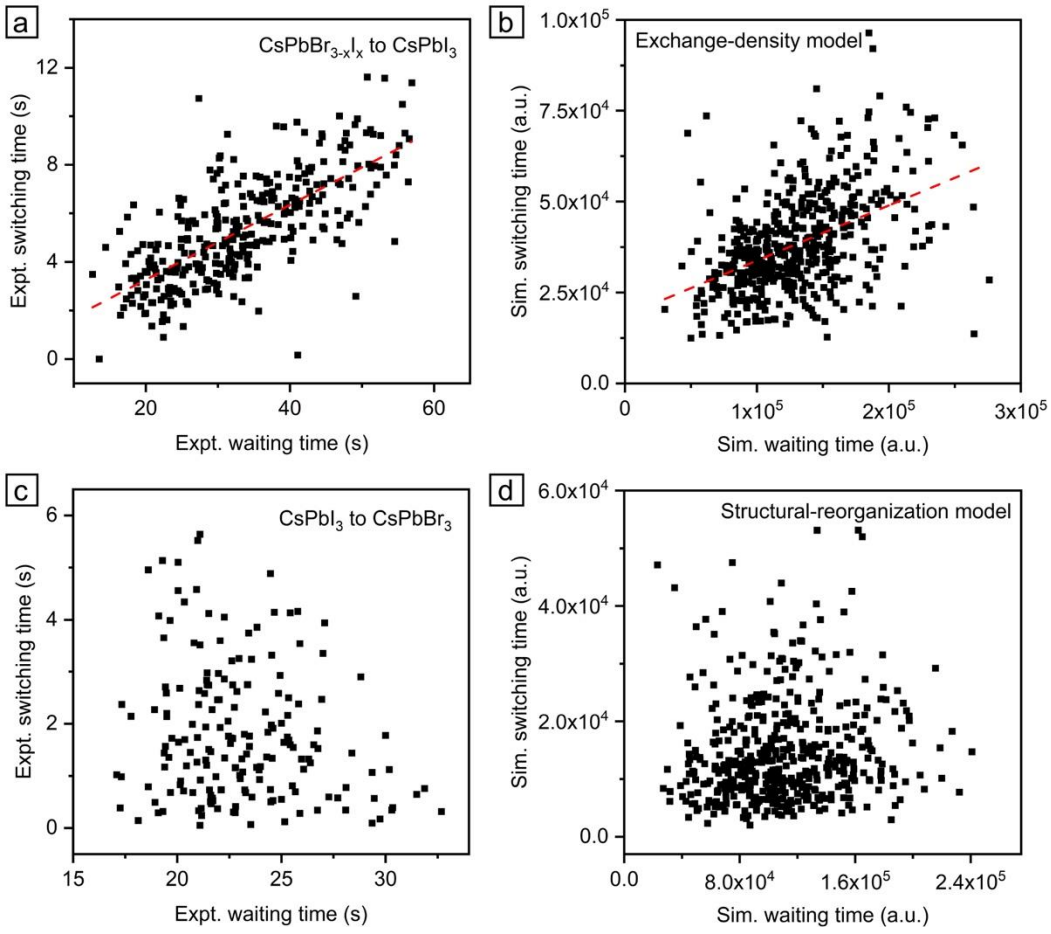

Figure 2.23. Plots of the waiting time vs. switching time for individual particles. (a) The back conversion of bromide-rich $CsPbBr_{3-x}I_x$ NCs to $CsPbI_3$ using a TBAI concentration of 1 μg/mL (2.7 μmol/L). (b) Exchange-density model using a simulated concentration $k_0 = 1$. (c) Transformation of as-synthesized $CsPbI_3$ NCs to $CsPbBr_3$ using a TBAB concentration of 1 μg/mL (3.1 μmol/L). (d) Structural-reorganization model using a simulated concentration $k_0 = 1$. The red dashed lines provide linear fits of the scatter plots in (a) and (b). The fitting parameters at different concentrations are provided in **Table 2.5**.

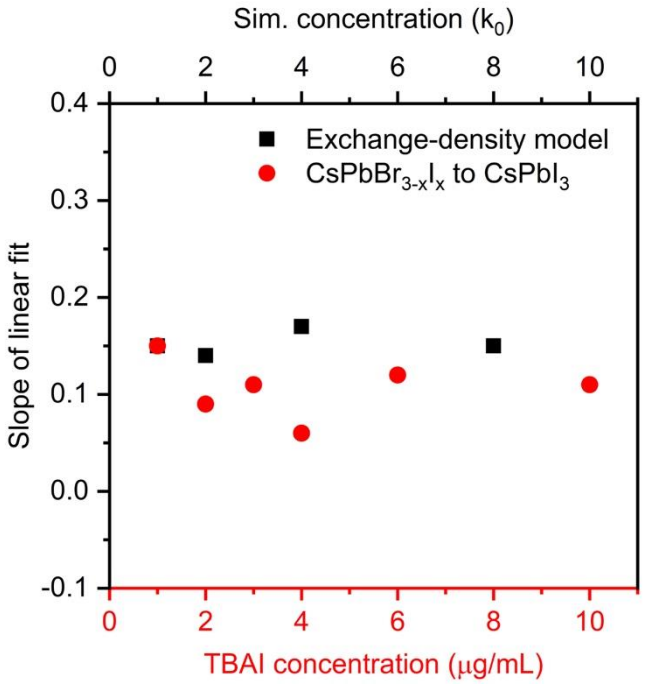

Figure 2.24. The slopes from linear fits to scatter plots of the waiting vs. switching time for individual particles. The red circles correspond to the back conversion of bromide-rich $CsPbBr_{3-x}I_x$ NCs to $CsPbI_3$ using TBAI concentrations of 1, 2, 3, 4, 6 and 10 μg/mL (2.7, 5.4, 8.1, 10.8, 16.2 and 27 μmol/L). The black squares correspond to the exchange-density model using simulated concentrations k_0 = 1, 2, 4, and 8. The mean slopes for the experimental and simulated results are 0.11 ± 0.03 and 0.15 ± 0.01, respectively.

2.7 References

1. Green, M. A.; Ho-Baillie, A.; Snaith, H. J., The emergence of perovskite solar cells. *Nature Photonics* **2014,** *8* (7), 506-514.

2. Lin, Q.; Armin, A.; Nagiri, R. C. R.; Burn, P. L.; Meredith, P., Electro-optics of perovskite solar cells. *Nature Photonics* **2014,** *9*, 106.

3. Wang, D.; Liu, Z.; Zhou, Z.; Zhu, H.; Zhou, Y.; Huang, C.; Wang, Z.; Xu, H.; Jin, Y.; Fan, B.; Pang, S.; Cui, G., Reproducible One-Step Fabrication of Compact MAPbI3–xClx Thin Films Derived from Mixed-Lead-Halide Precursors. *Chemistry of Materials* **2014,** *26* (24), 7145-7150.

4. Xiao, Z.; Kerner, R. A.; Zhao, L.; Tran, N. L.; Lee, K. M.; Koh, T.-W.; Scholes, G. D.; Rand, B. P., Efficient perovskite light-emitting diodes featuring nanometre-sized crystallites. *Nature Photonics* **2017,** *11* (2), 108-115.

5. Wang, N.; Cheng, L.; Ge, R.; Zhang, S.; Miao, Y.; Zou, W.; Yi, C.; Sun, Y.; Cao, Y.; Yang, R.; Wei, Y.; Guo, Q.; Ke, Y.; Yu, M.; Jin, Y.; Liu, Y.; Ding, Q.; Di, D.; Yang, L.; Xing, G.; Tian, H.; Jin, C.; Gao, F.; Friend, R. H.; Wang, J.; Huang, W., Perovskite light-emitting diodes based on solution-processed self-organized multiple quantum wells. *Nature Photonics* **2016,** *10* (11), 699-704.

6. Rainò, G.; Becker, M. A.; Bodnarchuk, M. I.; Mahrt, R. F.; Kovalenko, M. V.; Stöferle, T., Superfluorescence from lead halide perovskite quantum dot superlattices. *Nature* **2018,** *563* (7733), 671-675.

7. Utzat, H.; Sun, W.; Kaplan, A. E. K.; Krieg, F.; Ginterseder, M.; Spokoyny, B.; Klein, N. D.; Shulenberger, K. E.; Perkinson, C. F.; Kovalenko, M. V.; Bawendi, M. G., Coherent single-photon emission from colloidal lead halide perovskite quantum dots. *Science* **2019,** *363* (6431), 1068-1072.

8. Protesescu, L.; Yakunin, S.; Bodnarchuk, M. I.; Krieg, F.; Caputo, R.; Hendon, C. H.; Yang, R. X.; Walsh, A.; Kovalenko, M. V., Nanocrystals of Cesium Lead Halide Perovskites (CsPbX3, X = Cl, Br, and I): Novel Optoelectronic Materials Showing Bright Emission with Wide Color Gamut. *Nano Letters* **2015,** *15* (6), 3692-3696.

9. Swarnkar, A.; Chulliyil, R.; Ravi, V. K.; Irfanullah, M.; Chowdhury, A.; Nag, A., Colloidal CsPbBr3 Perovskite Nanocrystals: Luminescence beyond Traditional Quantum Dots. *Angewandte Chemie International Edition* **2015,** *54* (51), 15424-15428.

10. Bekenstein, Y.; Koscher, B. A.; Eaton, S. W.; Yang, P.; Alivisatos, A. P., Highly Luminescent Colloidal Nanoplates of Perovskite Cesium Lead Halide and Their Oriented Assemblies. *Journal of the American Chemical Society* **2015,** *137* (51), 16008-16011.

11. Di Stasio, F.; Christodoulou, S.; Huo, N.; Konstantatos, G., Near-Unity Photoluminescence Quantum Yield in CsPbBr3 Nanocrystal Solid-State Films via Postsynthesis

Treatment with Lead Bromide. *Chemistry of Materials* **2017,** *29* (18), 7663-7667.

12. Creutz, S. E.; Crites, E. N.; De Siena, M. C.; Gamelin, D. R., Anion Exchange in Cesium Lead Halide Perovskite Nanocrystals and Thin Films Using Trimethylsilyl Halide Reagents. *Chemistry of Materials* **2018,** *30* (15), 4887-4891.

13. Zhang, A.; Dong, C.; Ren, J., Tuning Blinking Behavior of Highly Luminescent Cesium Lead Halide Nanocrystals through Varying Halide Composition. *The Journal of Physical Chemistry C* **2017,** *121* (24), 13314-13323.

14. Yoshimura, H.; Yamauchi, M.; Masuo, S., In Situ Observation of Emission Behavior during Anion-Exchange Reaction of a Cesium Lead Halide Perovskite Nanocrystal at the Single-Nanocrystal Level. *The Journal of Physical Chemistry Letters* **2020,** *11* (2), 530-535.

15. Nedelcu, G.; Protesescu, L.; Yakunin, S.; Bodnarchuk, M. I.; Grotevent, M. J.; Kovalenko, M. V., Fast Anion-Exchange in Highly Luminescent Nanocrystals of Cesium Lead Halide Perovskites (CsPbX3, X = Cl, Br, I). *Nano Letters* **2015,** *15* (8), 5635-5640.

16. Akkerman, Q. A.; D'Innocenzo, V.; Accornero, S.; Scarpellini, A.; Petrozza, A.; Prato, M.; Manna, L., Tuning the Optical Properties of Cesium Lead Halide Perovskite Nanocrystals by Anion Exchange Reactions. *Journal of the American Chemical Society* **2015,** *137* (32), 10276-10281.

17. Hoffman, J. B.; Schleper, A. L.; Kamat, P. V., Transformation of Sintered CsPbBr3 Nanocrystals to Cubic CsPbI3 and Gradient CsPbBrxI3–x through Halide Exchange. *Journal of the American Chemical Society* **2016,** *138* (27), 8603-8611.

18. Pellet, N.; Teuscher, J.; Maier, J.; Grätzel, M., Transforming Hybrid Organic Inorganic Perovskites by Rapid Halide Exchange. *Chemistry of Materials* **2015,** *27* (6), 2181-2188.

19. Koscher, B. A.; Bronstein, N. D.; Olshansky, J. H.; Bekenstein, Y.; Alivisatos, A. P., Surface- vs Diffusion-Limited Mechanisms of Anion Exchange in CsPbBr3 Nanocrystal Cubes Revealed through Kinetic Studies. *Journal of the American Chemical Society* **2016,** *138* (37), 12065-12068.

20. Li, M.; Zhang, X.; Lu, S.; Yang, P., Phase transformation, morphology control, and luminescence evolution of cesium lead halide nanocrystals in the anion exchange process. *RSC Advances* **2016,** *6* (105), 103382-103389.

21. Rosales, B. A.; Men, L.; Cady, S. D.; Hanrahan, M. P.; Rossini, A. J.; Vela, J., Persistent Dopants and Phase Segregation in Organolead Mixed-Halide Perovskites. *Chemistry of Materials* **2016,** *28* (19), 6848-6859.

22. Bertolotti, F.; Protesescu, L.; Kovalenko, M. V.; Yakunin, S.; Cervellino, A.; Billinge, S. J. L.; Terban, M. W.; Pedersen, J. S.; Masciocchi, N.; Guagliardi, A., Coherent Nanotwins and Dynamic Disorder in Cesium Lead Halide Perovskite Nanocrystals. *ACS Nano* **2017,** *11* (4), 3819-3831.

23. Pan, D.; Fu, Y.; Chen, J.; Czech, K. J.; Wright, J. C.; Jin, S., Visualization and Studies of Ion-Diffusion Kinetics in Cesium Lead Bromide Perovskite Nanowires. *Nano Letters* **2018,** *18* (3), 1807-1813.

24. Haque, A.; Ravi, V. K.; Shanker, G. S.; Sarkar, I.; Nag, A.; Santra, P. K., Internal Heterostructure of Anion-Exchanged Cesium Lead Halide Nanocubes. *The Journal of Physical Chemistry C* **2018,** *122* (25), 13399-13406.

25. Yin, W.-J.; Yan, Y.; Wei, S.-H., Anomalous Alloy Properties in Mixed Halide Perovskites. *The Journal of Physical Chemistry Letters* **2014,** *5* (21), 3625-3631.

26. Bechtel, J. S.; Van der Ven, A., First-principles thermodynamics study of phase stability in inorganic halide perovskite solid solutions. *Physical Review Materials* **2018,** *2* (4), 045401.

27. Cottingham, P.; Brutchey, R. L., On the crystal structure of colloidally prepared CsPbBr3 quantum dots. *Chemical Communications* **2016,** *52* (30), 5246-5249.

28. Cottingham, P.; Brutchey, R. L., Compositionally Dependent Phase Identity of Colloidal CsPbBr3–xIx Quantum Dots. *Chemistry of Materials* **2016,** *28* (21), 7574-7577.

29. Zhao, Q.; Hazarika, A.; Schelhas, L. T.; Liu, J.; Gaulding, E. A.; Li, G.; Zhang, M.; Toney, M. F.; Sercel, P. C.; Luther, J. M., Size-Dependent Lattice Structure and Confinement Properties in CsPbI3 Perovskite Nanocrystals: Negative Surface Energy for Stabilization. *ACS Energy Letters* **2020,** *5* (1), 238-247.

30. Empedocles, S.; Bawendi, M., Spectroscopy of Single CdSe Nanocrystallites. *Accounts of Chemical Research* **1999,** *32* (5), 389-396.

31. Zhu, F.; Men, L.; Guo, Y.; Zhu, Q.; Bhattacharjee, U.; Goodwin, P. M.; Petrich, J. W.; Smith, E. A.; Vela, J., Shape Evolution and Single Particle Luminescence of Organometal Halide Perovskite Nanocrystals. *ACS Nano* **2015,** *9* (3), 2948-2959.

32. Park, Y.-S.; Guo, S.; Makarov, N. S.; Klimov, V. I., Room Temperature Single-Photon Emission from Individual Perovskite Quantum Dots. *ACS Nano* **2015,** *9* (10), 10386-10393.

33. Rainò, G.; Nedelcu, G.; Protesescu, L.; Bodnarchuk, M. I.; Kovalenko, M. V.; Mahrt, R. F.; Stöferle, T., Single Cesium Lead Halide Perovskite Nanocrystals at Low Temperature: Fast Single-Photon Emission, Reduced Blinking, and Exciton Fine Structure. *ACS Nano* **2016,** *10* (2), 2485-2490.

34. Utzat, H.; Shulenberger, K. E.; Achorn, O. B.; Nasilowski, M.; Sinclair, T. S.; Bawendi, M. G., Probing Linewidths and Biexciton Quantum Yields of Single Cesium Lead Halide Nanocrystals in Solution. *Nano Letters* **2017,** *17* (11), 6838-6846.

35. Freppon, D. J.; Men, L.; Burkhow, S. J.; Petrich, J. W.; Vela, J.; Smith, E. A., Photophysical properties of wavelength-tunable methylammonium lead halide perovskite nanocrystals. *Journal of Materials Chemistry C* **2017,** *5* (1), 118-126.

36. Gibson, N. A.; Koscher, B. A.; Alivisatos, A. P.; Leone, S. R., Excitation Intensity Dependence of Photoluminescence Blinking in CsPbBr3 Perovskite Nanocrystals. *The Journal of Physical Chemistry C* **2018,** *122* (22), 12106-12113.

37. Seth, S.; Ahmed, T.; Samanta, A., Photoluminescence Flickering and Blinking of Single CsPbBr3 Perovskite Nanocrystals: Revealing Explicit Carrier Recombination Dynamics. *The journal of physical chemistry letters* **2018,** *9* (24), 7007-7014.

38. Yuan, G.; Ritchie, C.; Ritter, M.; Murphy, S.; Gómez, D. E.; Mulvaney, P., The Degradation and Blinking of Single CsPbI3 Perovskite Quantum Dots. *The Journal of Physical Chemistry C* **2018,** *122* (25), 13407-13415.

39. Routzahn, A. L.; Jain, P. K., Single-Nanocrystal Reaction Trajectories Reveal Sharp Cooperative Transitions. *Nano Letters* **2014,** *14* (2), 987-992.

40. Routzahn, A. L.; Jain, P. K., Luminescence Blinking of a Reacting Quantum Dot. *Nano Letters* **2015,** *15* (4), 2504-2509.

41. Yin, B.; Cavin, J.; Wang, D.; Khan, D.; Shen, M.; Laing, C.; Mishra, R.; Sadtler, B., Fluorescence microscopy of single lead bromide nanocrystals reveals sharp transitions during their transformation to methylammonium lead bromide. *Journal of Materials Chemistry C* **2019,** *7* (12), 3486-3495.

42. Wang, D.; Cavin, J.; Yin, B.; Thind, A. S.; Borisevich, A. Y.; Mishra, R.; Sadtler, B., Role of Solid-State Miscibility during Anion Exchange in Cesium Lead Halide Nanocrystals Probed by Single-Particle Fluorescence. *The Journal of Physical Chemistry Letters* **2020,** *11* (3), 952-959.

43. Karimata, I.; Tachikawa, T., In Situ Exploration of the Structural Transition during Morphology- and Efficiency-Conserving Halide Exchange on a Single Perovskite Nanocrystal. *Angewandte Chemie International Edition n/a* (n/a).

44. Orfield, N. J.; McBride, J. R.; Keene, J. D.; Davis, L. M.; Rosenthal, S. J., Correlation of Atomic Structure and Photoluminescence of the Same Quantum Dot: Pinpointing Surface and Internal Defects That Inhibit Photoluminescence. *ACS Nano* **2015,** *9* (1), 831-839.

45. Ryan, D. P.; Goodwin, P. M.; Sheehan, C. J.; Whitcomb, K. J.; Gelfand, M. P.; Van Orden, A., Mapping Emission from Clusters of CdSe/ZnS Nanoparticles. *The Journal of Physical Chemistry C* **2018,** *122* (7), 4046-4053.

46. Smith, A. M.; Nie, S., Bright and Compact Alloyed Quantum Dots with Broadly Tunable Near-Infrared Absorption and Fluorescence Spectra through Mercury Cation Exchange. *Journal of the American Chemical Society* **2011,** *133* (1), 24-26.

47. White, S. L.; Smith, J. G.; Behl, M.; Jain, P. K., Co-operativity in a nanocrystalline solid-state transition. *Nature Communications* **2013,** *4*, 2933.

48. Marronnier, A.; Roma, G.; Boyer-Richard, S.; Pedesseau, L.; Jancu, J.-M.; Bonnassieux,

Y.; Katan, C.; Stoumpos, C. C.; Kanatzidis, M. G.; Even, J., Anharmonicity and Disorder in the Black Phases of Cesium Lead Iodide Used for Stable Inorganic Perovskite Solar Cells. *ACS Nano* **2018,** *12* (4), 3477-3486.

49. Feng Yang, C. W., Yuhao Pan, Xieyu Zhou, Xianghua Kong, Wei Ji, Surface stabilized cubic phase of CsPbI₃ and CsPbBr₃ at room temperature. *Chin. Phys. B* **2019,** *28* (5), 56402-056402.

50. Yang, R. X.; Tan, L. Z., Understanding size dependence of phase stability and band gap in CsPbI3 perovskite nanocrystals. *The Journal of Chemical Physics* **2020,** *152* (3), 034702.

51. Jeon, S.; Jung, M.-C.; Ahn, J.; Woo, H. K.; Bang, J.; Kim, D.; Lee, S. Y.; Woo, H. Y.; Jeon, J.; Han, M. J.; Paik, T.; Oh, S. J., Post-synthetic oriented attachment of CsPbBr3 perovskite nanocrystal building blocks: from first principle calculation to experimental demonstration of size and dimensionality (0D/1D/2D). *Nanoscale Horizons* **2020,** *5* (6), 960-970.

52. Bertolotti, F.; Nedelcu, G.; Vivani, A.; Cervellino, A.; Masciocchi, N.; Guagliardi, A.; Kovalenko, M. V., Crystal Structure, Morphology, and Surface Termination of Cyan-Emissive, Six-Monolayers-Thick CsPbBr3 Nanoplatelets from X-ray Total Scattering. *ACS Nano* **2019,** *13* (12), 14294-14307.

53. Lv, L.; Xu, Y.; Fang, H.; Luo, W.; Xu, F.; Liu, L.; Wang, B.; Zhang, X.; Yang, D.; Hu, W.; Dong, A., Generalized colloidal synthesis of high-quality, two-dimensional cesium lead halide perovskite nanosheets and their applications in photodetectors. *Nanoscale* **2016,** *8* (28), 13589-13596.

Chapter 3: Size-Dependent Miscibility Controls the Kinetics of Anion Exchange in Cesium Lead Halide Nanocrystals

A manuscript based on this chapter by **Zhang, D.**; Wu, X.; Wang, D. Sadtler, B., and titled "Size-Dependent Miscibility Controls the Kinetics of Anion Exchange in Cesium Lead Halide Nanocrystals" is currently under review in the Journal of Chemical Physics.

Author contributions: **Zhang, D.** and Sadtler, B. designed the research. **Zhang, D.** and Wu, X. synthesized the $CsPbBr_3$ nanocrystals with different sizes. **Zhang, D.** and Wu, X. performed experiments of anion exchange from $CsPbBr_3$ nanocrystals to $CsPbI_3$ at the ensemble and single-particle scale. **Zhang D.** characterized samples and designed simluation models. All authors made contributions to data analysis and simulations.

3.1 Introduction

Colloidal semiconductor nanocrystals (NCs) exhibit size-dependent chemical and physical properties.[1-16] In addition to size-dependent shifts in their optical absorption and emission spectra, the relative stability of different crystalline phases and the kinetics and thermodynamics of transitions between phases in nanoscale crystals is size dependent. For example, the pressure needed to transform wurtzite CdSe NCs into rock salt increases as their size decreases due the lower surface energies of facets that comprise the initial wurtzite NCs relative to the rock salt phase and the increasing contribution of surface energy to the total energy of the crystals.[5, 6, 8, 9] More recently, size-dependent changes in the structure of cesium lead halide perovskite nanocrystals have been reported.[16] The cubic (α) and orthorhombic (γ) phases are the two main structures observed for perovskite $CsPbX_3$ NCs. Calculations using density functional theory indicate that the cubic perovskite phase becomes more stable than the orthorhombic phase as the nanocrystal size decreases due to the lower surface energy of the cubic phase.[17, 18]

Lead halide perovskite semiconductors with the formula $APbX_3$ (A = $CH_3NH_3^+$ or Cs^+, X = Cl^-, Br^-, I^-) are promising candidates as the active material in solar cells, light-emitting diodes (LEDs), and other optoelectronic devices.[19-27] The high photoluminescence (PL) quantum yield, tunable bandgap, and solution-phase processing of $CsPbX_3$ nanocrystals make these materials attractive in light-emission applications.[28-34] Post-synthetic exchange of the halide anions in $CsPbX_3$ NCs produces solid solutions with tunable anion ratios (e.g., $CsPbBr_{3-x}I_x$ with $0 < x < 3$); the final anion composition is controlled by the relative concentrations of the substitutional and lattice halide anions.[29, 35-40] Since this reaction occurs within minutes at room temperature, anion exchange is an attractive method to control the bandgap and absorption and emission properties of cesium lead halide nanocrystals for optoelectronic devices.

Heterogeneity in the composition of $CsPbX_{3-x}Y_x$ solid solutions (where X and Y are two different halide anions) will lower the color purity of their emission, which is undesirable for LEDs incorporating these materials. Within a single crystal, the relative solid-state miscibility between halide anions determines the compositional homogeneity. $CsPbCl_3$ and $CsPbBr_3$ exhibit high miscibility and generally show high compositional uniformity following anion exchange.[35, 41] However, because of the larger difference in size and electronegativity between Br^- and I^- and the lower tolerance factors for perovskite $CsPbBr_3$ and $CsPbI_3$ crystals, this anion pair exhibits lower miscibility compared to the Cl/Br pair.[39, 42] For example, $CsPbBr_{3-x}I_x$ NCs produced by anion exchange of $CsPbBr_3$ NCs with PbI_2 were shown to possess a radial compositional gradient that is bromide rich at the core and iodide rich near the surface.[43]

Beyond heterogeneity within individual particles, variations in the size and shape of NCs prepared within the same batch along with differences in the local concentration of substitutional ions will lead to different rates of ion exchange among the NCs. Prior studies that monitor the ensemble emission wavelength or diffraction peaks of a large population of NCs have shown there are different stages of reaction during anion exchange.[39, 44, 45] For example, different kinetics were observed for the transformation of $CsPbBr_3$ NCs to $CsPbCl_3$ compared with the transformation of $CsPbBr_3$ NCs to $CsPbI_3$; anion exchange was attributed to being diffusion-limited for the former but surface-limited for the latter.[44] However, because these measurements average over asynchronous changes in the transformation of many NCs, they obscure heterogeneity in the reactivity of individual NCs.

Single-particle measurements enable the quantification of how variations in the chemical and physical properties among different particles contribute to the ensemble behavior.[41, 46-66] In situ fluorescence microcopy has been used to monitor changes in the fluorescence intensity,

wavelength, and lifetime of individual semiconductor nanocrystals and microcrystals undergoing anion exchange, cation exchange, and ion intercalation.[41, 58-66] Measuring the fluorescence spectrum and/or fluorescence lifetime of a single NC during anion exchange provides information on how the photophysics of the semiconductor change with the extent of the reaction.[64-66] However, these measurements are generally limited to following only one particle at a time. On the other hand, by observing changes in fluorescence intensity, the transformation of hundreds of individual nanocrystals can be recorded simultaneously. Our previous work has used this method to monitor anion exchange between different $CsPbX_3$ (X = Cl, Br, I) NCs.[41, 63] In all cases, the time it takes a single NC to undergo ion exchange is much shorter than ensemble reaction rate. Each NC exhibits both a unique starting time to begin anion exchange (as determined by when the fluorescence intensity started to rise) and time to complete the transformation (as determined by when the fluorescence intensity plateaus). We thus assign a switching time to each single-particle fluorescence trajectory based on the rate of the intensity rise.

For different solid-state transformations, the concentration dependence of switching times has been shown to reflect the relative miscibility between the initial and final crystals. The switching time is independent of the concentration of the substitutional ions when the initial and final structures are immiscible (e.g., cation exchange between CdSe and Ag_2Se NCs and intercalation of $CH_3NH_3^+$ and Br^- into $PbBr_2$ NCs).[58, 62] In contrast, for highly miscible systems like anion exchange between $CsPbCl_3$ and $CsPbBr_3$ NCs, the switching times are strongly concentration dependent.[41] $CsPbBr_3$ and $CsPbI_3$ NCs exhibit intermediate miscibility between these extremes. We previously studied anion exchange between $CsPbBr_3$ and $CsPbI_3$ NCs using single-particle fluorescence and observed asymmetric behavior for the forward and backward exchange reactions (i.e., $CsPbBr_3$ to $CsPbI_3$ and vice versa).[63] We assigned this asymmetry to a smaller structural

reorganization that occurs when $CsPbBr_3$ NCs are converted to $CsPbI_3$ compared to exchange in the opposite direction (indicating the exchange reaction is irreversible). However, we only studied $CsPbBr_3$ NCs of a single size.

In this work, we synthesized $CsPbBr_3$ NCs with different average sizes to study the size-dependence of anion exchange to produce $CsPbI_3$ NCs. We used single-particle fluorescence microscopy to image the transformation of individual $CsPbBr_3$ NCs to $CsPbI_3$. We observe that smaller NCs exhibit a stronger concentration dependence of their switching times and longer switching times at lower concentrations of substitutional iodide compared to larger NCs. We used Monte Carlo methods to simulate anion exchange in individual particles and construct different models for how the particle size affects the probability for exchange. A larger amount of structural reorganization in a particle is reflected in a larger degree of positive cooperativity for successive exchange events, which leads to smaller dependence of the switching time on the simulated concentration. By combining our experimental results with these simulations, we propose that smaller $CsPbBr_3$ NCs maintain a more homogenous structure and composition during anion exchange compared with larger NCs, which leads to longer transformation times once the reaction has started. On the other hand, the greater amount of structural reorganization needed for the transformation of larger NCs causes their switching times to be more abrupt. The insights gained from these studies inform the synthesis of $CsPbX_3$ NCs with uniform composition and emission wavelength. In the production of mixed-halide lead perovskite NCs via anion exchange, a high concentration of substitutional halide anions can suppress differences in the reactivity between nanocrystals of different sizes.

3.2 Experimental

Materials

The following chemicals were used as received: cesium carbonate (Cs_2CO_3, 99%, Millipore Sigma Inc.), lead(II) bromide ($PbBr_2$, > 98%, Alfa Aesar), oleic acid (OA, 90%, Millipore Sigma Inc.), oleylamine (OAm, 70%, Millipore Sigma Inc.), hexane (anhydrous, 95%, Millipore Sigma Inc.), 1-octadecene (ODE, tech. 90%, Alfa Aesar), trimethylsilyl iodide (TMSI, 97%, Millipore Sigma Inc.), acetone (HPLC, 99.8%, Millipore Sigma Inc.). TMSI was stored at –20°C in a built-in refrigerator inside a nitrogen-filled glovebox. The bottle of TMSI was used within one month after opening it to minimize degradation.

Synthesis of $CsPbBr_3$ nanocrystals with average edge length of 9.5 nm

All flasks used to synthesize $CsPbBr_3$ nanocrystals were stirred at 400 rpm using a magnetic stir bar and stirring plate to dissolve and mix the reagents. The synthesis of $CsPbBr_3$ NCs with an average edge length of 9.5 nm was adapted from the procedure of Kovalenko et al.,[28] with modifications as follows. To prepare the Cs-oleate precursor solution, 0.102 g of Cs_2CO_3 was added to a mixture of 0.312 mL of OA and 5 mL of ODE in a 50-mL, round-bottom flask (labeled as Flask I). To prepare the lead bromide precursor, 0.069 g of $PbBr_2$ was added to a mixture of 1 mL of OA, 1 mL of OAm, and 5 mL of ODE in a second 50-mL, round-bottom flask (labeled as Flask II). Both flasks were heated at 120°C under vacuum for 30 min. The temperature of Flask I was then raised to 150°C while that of Flask II remained at 120°C under argon (95%) for another 30 min. Next, 0.4 mL of the solution from Flask I was swiftly injected into Flask II. After 1 min, Flask II was quenched in an ice bath. The mixture in Flask II was then transferred to a centrifuge

tube and centrifuged at 8000 rpm for 5 min. The precipitate was collected, transferred into a glovebox, and dispersed in 10 mL of hexane.

Synthesis of $CsPbBr_3$ nanocrystals with average edge lengths of 5.1, 6.1, and 7.8 nm

To prepare $CsPbBr_3$ NCs with average sizes smaller than 9.5 nm, we adapted the procedure from Son et al.,[67] with modifications as follows. For the Cs-oleate solution, 0.125 g of Cs_2CO_3 was dissolved in a mixture of 0.447 mL of OA and 4.436 mL of ODE in a 50-mL, round-bottom flask (labeled as Flask I). To prepare the lead bromide precursor, 0.074 g of $PbBr_2$ and varying amounts of $ZnBr_2$ (0 – 0.533 g) were added into a mixture of 1 mL of OA, 1 mL of OAm, and 5 mL of ODE in a second 50-mL, round-bottom flask (labeled as Flask II). The amounts of $ZnBr_2$ were 0.184 g, 0.530 g, and 0.530 g to produce $CsPbBr_3$ NCs with average edge lengths of 5.1, 6.1, and 7.8 nm, respectively. Both flasks were heated at 120°C under vacuum for 30 min. Flask I was then heated to 150°C under Ar while Flask II was maintained at 120°C under Ar for another 30 min. Before injection of the Cs-oleate precursor, Flask II was heated to either 140℃ (for 5.1-nm NCs) or 190℃ (for 6.1- and 7.8-nm NCs). Then, 0.2 mL of the solution from Flask I was injected swiftly into Flask II. After different reaction times (88 s for 5.1-nm NCs, 10 s for 6.1-nm NCs, and 10 s for 7.8-nm NCs), Flask II was quenched in an ice bath.

For the batches of $CsPbBr_3$ NCs with average sizes of 5.1 and 6.1 nm, the washing procedure is as follows. After cooling, the mixture in Flask II was transferred to a centrifuge tube and centrifuged at 3500 rpm for 10 min to remove unreacted salts. The supernatant was collected, and the precipitate was discarded. As an antisolvent, 8 mL of acetone was then added to the supernatant and mixed thoroughly. The mixture was centrifuged at 3500 rpm for 3 min. The precipitate was collected, transferred into a glovebox, and dispersed in 10 mL of hexane. For the batch of $CsPbBr_3$

NCs with an average size of 7.8 nm, the mixture after synthesis was transferred to a centrifuge tube and centrifuged at 8000 rpm for 5 min. The precipitate was collected, transferred into a glovebox, and 10 mL hexane was added to disperse the precipitate. The mixture was centrifuged again at 3500 rpm for 3 min to remove unreacted salts. The supernatant was collected and transferred into a glovebox.

Synthesis of $CsPbBr_3$ nanocrystals with average edge length of 13.1 nm

The synthesis of $CsPbBr_3$ NCs with an average edge length of 13.1 nm was adapted from the step-growth method reported by Xie, Pradhan, et al.[68] For the Cs-oleate solution, 0.131 g of Cs_2CO_3 was dissolved in a mixture of 0.5 mL of OA and 3.2 mL of ODE in a 50-mL, round-bottom flask (labeled as Flask I). To prepare the lead bromide precursor, 0.0734 g of $PbBr_2$ was added to a mixture of 0.5 mL of OA, 0.5 mL of OAm, and 3.5 mL of ODE in a second 50-mL, round-bottom flask (labeled as Flask II). Flask I was maintained at 120°C under vacuum for 1 h and then heated to 150°C under Ar until the mixture turned clear. Flask II was maintained at 150°C under vacuum for 30 min then under Ar until the mixture turned clear. The mixture in Flask II was then cooled down to 25°C. Next, 0.2 mL of the mixture in Flask I was injected into Flask II. After reacting for 30 minutes while stirring, the mixture was centrifuged at 10,000 rpm for 10 min. The precipitate was collected, transferred into a glovebox, and dispersed in 2 mL of ODE to prepare a seed solution for further growth.

In a third 50-mL, round-bottom flask (labeled as Flask III), 4 mL of ODE was maintained at 25°C under vacuum for 10 min. The atmosphere was then switched to Ar while 2 mL of the seed solution was injected into Flask III. The mixture was heated to 200°C with a heating rate of approximately 10°C/min. After the temperature reached 200°C, the mixture was cooled in an ice

bath to room temperature, transferred to a centrifuge tube, and then centrifuged at 10,000 rpm for 10 min. The precipitate was collected, transferred into a glovebox, and dispersed in 10 mL of hexane.

Optical spectroscopy

Photoluminescence (PL) spectra were measured using a Cary Eclipse fluorescence spectrophotometer. The excitation wavelength was 400 nm, and the step size was 1 nm. The entrance and exit slits were set to 5 nm. To prepare samples for PL spectroscopy, the original solution of $CsPbBr_3$ NCs was diluted 200 times with hexane and transferred to a quartz cuvette. The time evolution of PL spectra for a given sample during anion exchange was measured by adding 100 µL of a 0.01 M solution of TMSI in hexane to the cuvette and running a PL scan every 35 seconds. This concentration of TMSI provides an excess of iodide relative to the total amount of bromide in the $CsPbBr_3$ sample. Titrations of the amount of TMSI needed for anion exchange to be complete were determined by sequentially adding 20-µL aliquots of a 0.001 M solution of TMSI in hexane to the cuvette containing $CsPbBr_3$ NCs in hexane. After each addition of TMSI, the cuvette was shaken thoroughly for 30 seconds, and a PL spectrum was acquired. Only representative spectra are plotted in **Figure 3.9** for the titration experiments of each NC size.

UV-Vis absorption spectra were measured using a Cary 60 spectrometer. The scan range was from 800 nm to 200 nm. To prepare samples for absorption spectroscopy, the original $CsPbBr_3$ NC solution was diluted 50 times with hexane and transferred to a quartz cuvette.

Single-particle fluorescence microscopy

To prepare flow cells to image anion exchange using single-particle fluorescence microscopy, diluted solutions of the $CsPbBr_3$ NCs were spin-coated onto microscope coverslips. Two holes were drilled into a separate glass slide using a Dremel, which was then attached to the microscope coverslip using epoxy to make the flow cell. Additional details on the preparation of flow cells are provided in section **2.2** of **Chapter 2** and in our previous reports.[41, 62, 63]

The flow cell was placed on the stage of an inverted fluorescence microscope with the coverslip containing the NCs on the bottom. Fluorescence microscopy was performed using a Nikon N-STORM microscopy system consisting of a Nikon TiE motorized inverted optical microscope and a Nikon CFI-6-APO TIRF 100× oil-immersion objective lens with a numerical aperture of 1.49 and a working distance of 210 μm. An X-cite 120 LED system with a light intensity of ∼29 $\mu W/cm^2$ at the focal plane was used as excitation source. The flow cell was first filled with pure hexane using a syringe pump. The top of the coverslip with deposited $CsPbBr_3$ NCs was brought into focus using a green filter set (Chroma #49002-ET-EGFP, excitation window: 450 – 490 nm, emission window: 500 – 540 nm). A second syringe pump was used to inject a TMSI solution into the flow cell to induce anion exchange. The flow rate was fixed at 20 mL/h based on our prior work.[63] The concentrations of TMSI solutions we used were 5, 7.5, 10, 12.5, 15, 20, 30, 50 μM. To monitor anion exchange of single $CsPbBr_3$ nanocrystals, a red filter set (Chroma #49005-ET-DSRed, excitation window: 530−558 nm, emission window: 590−649 nm) was used to observe the emission from $CsPbBr_{3-x}I_3$ nanocrystals during anion exchange. Under these conditions, the background is initially dark as the emission filter cut offs the emission from the $CsPbBr_3$ NCs. The emission of individual $CsPbBr_{3-x}I_3$ NCs shifts to longer wavelengths as they become richer in iodide, leading to an increase in their fluorescence intensity. An Andor iXon 897 electron-

multiplying CCD camera (512 × 512, 16 μm pixels, > 90% quantum efficiency) was used to detect fluorescence signals. The exposure time was set to 50 ms.

Transmission electron microscopy (TEM)

TEM images were acquired by using a JEOL 2100F TEM operated at an acceleration voltage of 200 kV. An aliquot of the solution of $CsPbBr_3$ NCs was diluted approximately 10 times with hexane. Then, 20 μL of the diluted solution was drop cast onto a copper TEM grid in a glovebox and allowed to dry at room temperature.

X-ray Diffraction (XRD)

XRD patterns were measured in air with a Bruker D8 Advance X-ray diffractometer (wavelength = 0.15418 nm using Cu Kα radiation, step size = 0.02 in 2θ, and scan rate = 0.5 seconds/step). For each batch of $CsPbBr_3$ nanocrystals (NCs), the solution was drop cast onto a low-background, silicon diffraction plate for XRD in a nitrogen-filled glovebox. The XRD plate was kept in the glovebox until completely dry and brought to the diffractometer in a nitrogen-filled zip-lock bag. The experimental diffraction patterns were compared to a standard XRD pattern for the orthorhombic phase of $CsPbBr_3$ (PDF card #04-014-9676).

Analysis of fluorescence videos

The intensity changes versus time during anion exchange for individual $CsPbBr_3$ NCs were recorded using fluorescence microscopy. To plot single-particle reaction trajectories, the brightness and contrast of each video were first adjusted automatically by using the built-in look-up tables (LUTs) of the Nikon Analysis software (Version 4.50). Particles exhibiting fluorescence

intermittency with digital "on" and "off" states in their reaction trajectories were considered to be single particles (see **Figure 3.11**). Only these single particles were selected for further analysis while clusters of particles (i.e., multiple emitters within a diffraction-limited spot) that did not show a clear off state were excluded.

To obtain statistical information on anion exchange under different reaction conditions (e.g., different concentrations of trimethylsilyl iodide, TMSI, and difference sizes of NCs), we analyzed the changes in fluorescence intensity of hundreds of single $CsPbBr_3$ NCs undergoing anion exchange within the same field of view of the microscope. To quantify differences in the reaction trajectories for different NCs, we defined a "switching time" for each trajectory, which was obtained by fitting the trajectory with a sigmoidal function:

$$I(\mathrm{t}) = I_{initial} + \frac{\left(I_{final} - I_{initial}\right)}{1 + e^{(b-t/\tau)}} \tag{3.1}$$

$I_{initial}$ and I_{final} are the mean values of fluorescence intensity within a 5-s window (100 data points) at the start and the maximum intensity of a single-particle trajectory, respectively. We extracted two parameters, b and τ, from fitting the trajectories using MATLAB. The value of τ represents the switching time, which indicates the steepness of the intensity rise for a sigmoidal trajectory, while b is the inflection point of the sigmoidal curve. The goodness of fit was evaluated by the correlation coefficient. Only trajectories with a correlation coefficient above 0.75 were used in further analysis.

Monte Carlo simulations

We started with a model developed by Routzahn and Jain, who previously applied Monte Carlo methods to simulate cation exchange between $AgNO_3$ and CdSe NCs to form Ag_2Se NCs.[58] In previous work, we adapted this model to study how the relative miscibility between initial and final crystals affects the kinetics of anion exchange between various pairs of cesium lead halide nanocrystals (e.g., forward and back exchange between $CsPbCl_3$ and $CsPbBr_3$ NCs and between $CsPbBr_3$ and $CsPbI_3$ NCs).[41, 63] In the current work, Monte Carlo simulations were used to model single-particle trajectories for anion exchange of $CsPbBr_3$ NCs with different sizes to $CsPbI_3$. Each simulation included 500 particles, and each particle had 20 sites for exchange events to take place. At each step, a particle was chosen at random to react. If all 20 sites of this particle had already undergone exchange, the trajectory moved to the next time step without exchange. Otherwise, the success or failure for the i^{th} exchange event in the selected particle was determined by the probability p_i. The exchange event occurred only if p_i was larger than a random number between 0 and 1 generated by the simulation. This process was repeated until either the average number of exchanged sites among the 500 particles reached 19.998 or until the total time steps reached 600,000. Cooperativity during the reaction was controlled by how the value of p_i changed with consecutive successful exchange events in a particle during the simulation. The value of p_i was determined by an equilibrium constant k_i and the change in free energy ΔG_i for each exchange event. The relationships among p_i, k_i and ΔG_i are described by the following equations:

$$k_i = \exp(-\Delta G_i) \tag{3.2}$$

$$p_i = \frac{k_i}{1 + k_i} \tag{3.3}$$

The change in free energy for i^{th} exchange event is:

$$\Delta G_i = \Delta G_0 + \Delta g_i \tag{3.4}$$

where ΔG_0 is a constant that depends on the simulated concentration of substitutional ions, and Δg_i determines how the free energy changes with the number of successful events.

To simulate different concentrations of substitutional ions used to induce anion exchange, an empirical factor, k_1, was varied from 0.03 to 0.24; this range of values allows the simulation code to run within a reasonable number of time steps (< 600,000). The values of k_1 were converted to simulated concentrations, k_0, with an empirical scaling factor used to make the range of simulated concentrations within the same order of magnitude as the experimental range of TMSI concentrations. The relationship between k_0 and k_1 is given by the following equation:

$$k_0 = \frac{k_1}{0.03} \tag{3.5}$$

Constant-probability model: In this model, future exchange events are not affected by the number of exchange events that have already occurred in a particle. The value of Δg_i is 0 for all time steps. Consequently, the probability for each exchange event is constant. This model produces switching times that are strongly dependent on the simulated concentration, k_0, similar to what we observed for $CsPbBr_3$ NCs with small sizes (i.e., 5.1 and 6.1 nm).

Exchange-density model: Our previous work used this model for anion exchange from $CsPbCl_3$ to $CsPbBr_3$ NCs and from $CsPbBr_3$ to $CsPbI_3$ NCs.[41, 63] For these exchange pairs, we determined that the concentration dependence of switching times could be reproduced when the value of ΔG_i gradually decreased with the number of successful exchange events (and thus the probability for exchange gradually increased). Thus, we used a quadratic dependence for how the change in free energy, Δg_i, changed with the number of exchanged sites in a particle.

$$\Delta g_i = -\delta i^2 \tag{3.6}$$

where δ is an empirical constant. However, we previously only modeled the exchange of $CsPbBr_3$ NCs with an average size 9.4 nm in which δ was set to 0.005. More recent reports have shown that $CsPbI_3$ NCs exhibit size-dependent surface strain, which changes the lattice constants of the nanocrystals.[16] Thus, we hypothesized that the miscibility between $CsPbBr_3$ and $CsPbI_3$ is size dependent at the nanoscale. To account for this size dependence, we varied the value of δ to change the degree of cooperativity for anion exchange. Simulated changes in the free energy, ΔG_i, and probability, p_i, for anion exchange as the number of exchange events, i, in a particle increases for δ values of 0.0005, 0.001, 0.005, 0.01, 0.02, 0.03, and 0.05 to are shown in **Figure 3.S10** below. When is δ small (i.e., δ = 0.0005), the results reproduce those of the constant-probability model. As δ increases, the probability for further exchange increases more steeply with the number of exchange events.

3.3 Results

We first characterized the structural and ensemble optical properties of colloidal $CsPbBr_3$ nanocrystals (NCs) synthesized by the hot-injection method. Details of the synthesis are provided in the **Experimental section 3.2**. $CsPbBr_3$ NCs with average edge lengths of 5.1, 6.1, 7.8, 9.5, and 13.1 nm were synthesized by adapting procedures from previous literature reports.[28, 67, 68] Representative transmission electron microscopy (TEM) images for each batch of $CsPbBr_3$ NCs are shown in **Figure 3.1**. Histograms of the distribution of edge lengths for each average NC size were fit to a normal distribution and are provided in **Figure 3.6** of the **Appendix B**. The largest size of NCs also contained rectangular particles. The average edge length of the shorter edge was 13.1 nm, while the average edge length of the longer edge was 15.8 nm (for simplicity, this size will be referred to as 13.1-nm NCs as the optical spectra are determined by the shorter dimension). Both the photoluminescence (PL) spectra (**Figure 3.2(a)**) and UV-visible absorption spectra (**Figure 3.7**) show size-dependent spectral shifts consistent with prior reports.[28, 29, 44, 67-69] Due to quantum confinement, both the PL emission maxima and the first-exciton absorption edges shift to shorter wavelengths as the average NC size decreases. **Table 3.1** in the **Appendix B** provides the peak maxima and full widths at half maximum of the PL spectra. X-ray diffraction (XRD) patterns indicate that all batches of $CsPbBr_3$ NCs possess the orthorhombic perovskite structure (**Figure 3.8**). Broadening of the diffraction peaks was also observed as the NC size decreased as expected based on Scherrer broadening. This combined characterization shows we successfully controlled the size of $CsPbBr_3$ NCs by tuning the synthesis conditions and the washing process, which enables us to study the size dependence of anion exchange.

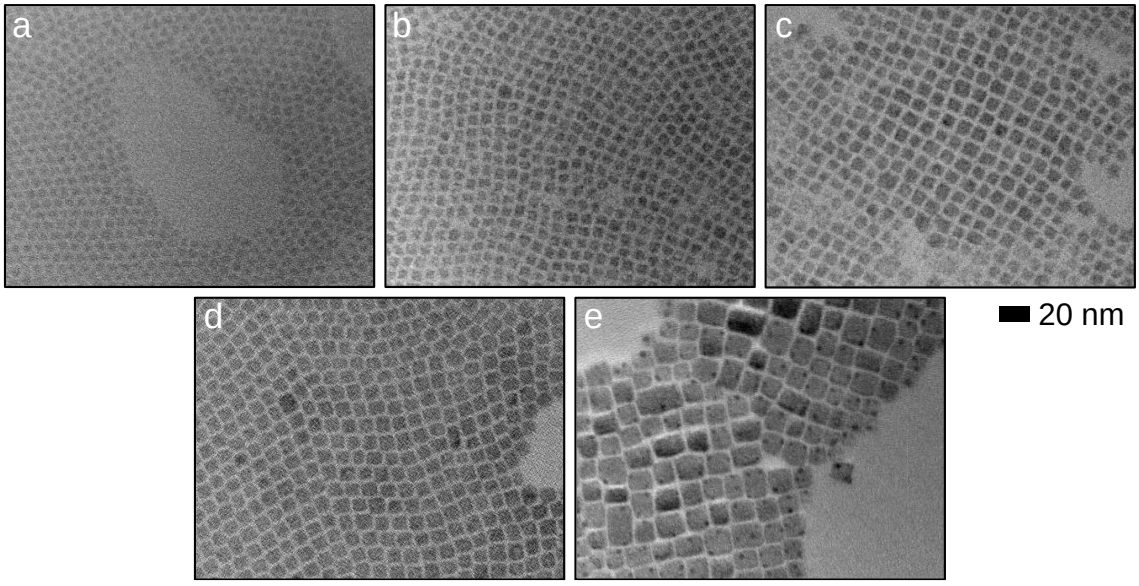

Figure 3.1. (a-e) TEM images of $CsPbBr_3$ NCs with different sizes. The average edge lengths of the NCs are (a) 5.1 ± 0.6 nm, (b) 6.1 ± 0.8 nm, (c) 7.8 ± 1.2 nm, (d) 9.5 ± 1.5 nm, and (e) 13.1 ± 2.0 × 15.8 ± 3.2 nm. Histograms of the size distribution for each batch of NCs are shown in **Figure 3.6**.

We next studied the transformation from $CsPbBr_3$ to $CsPbI_3$ NCs at the ensemble level using fluorescence spectroscopy. Trimethylsilyl iodide (TMSI) was used as a precursor to convert $CsPbBr_3$ nanocrystals to $CsPbI_3$ via anion exchange. While we previously used tetrabutylammonium iodide to perform anion exchange in $CsPbBr_3$ NCs with an average edge length of 9.4 nm,[63] we found that this iodide precursor led to degradation in the smallest NC sizes studied here. TMSI dissolved in anhydrous hexane (i.e., the same solvent used to suspend the NCs) has been previously shown to significantly limit the degradation of $CsPbBr_3$ NCs during anion exchange to $CsPbI_3$.[40] The amount of TMSI added into a cuvette containing a solution of the $CsPbBr_3$ NCs in hexane was sufficient to provide an excess of iodide anions (see the **Experimental section 3.2** and **Figure 3.9** for details). Immediately after the addition of TMSI, the cuvette was

shaken thoroughly, and fluorescence spectra were acquired every 35 seconds (i.e., the time it takes to collect a single spectrum). The time-dependent shifts in PL emission maxima for 5.1-nm $CsPbBr_3$ NCs after the addition of TMSI are shown in **Figure 3.2(b)**. The PL maximum of the initial $CsPbBr_3$ NCs was 486 nm, which shifts to 622 nm during the first 35 seconds of anion exchange. There is little change in the PL maxima after the first 35 seconds indicating that the exchange reaction has reached completion. A slight blue shift of the PL maxima to 615 nm occurred over a period of 315 seconds, which we attribute to etching of the NCs. The changes in PL emission maxima for 13.1-nm $CsPbBr_3$ NCs after TMSI addition are shown in **Figure 3.2(c)**. The emission maxima undergo a more gradual shift towards longer wavelengths compared to smaller NCs. Over a period of 1435, seconds, the maxima shift from 516 nm to 661 nm. While this method of observing the ensemble reaction rate is qualitative, the longer reactions times observed here for anion exchange of larger nanocrystals agree with previous reports using stop-flow techniques to quantitatively measure the ensemble-level reaction kinetics.[44]

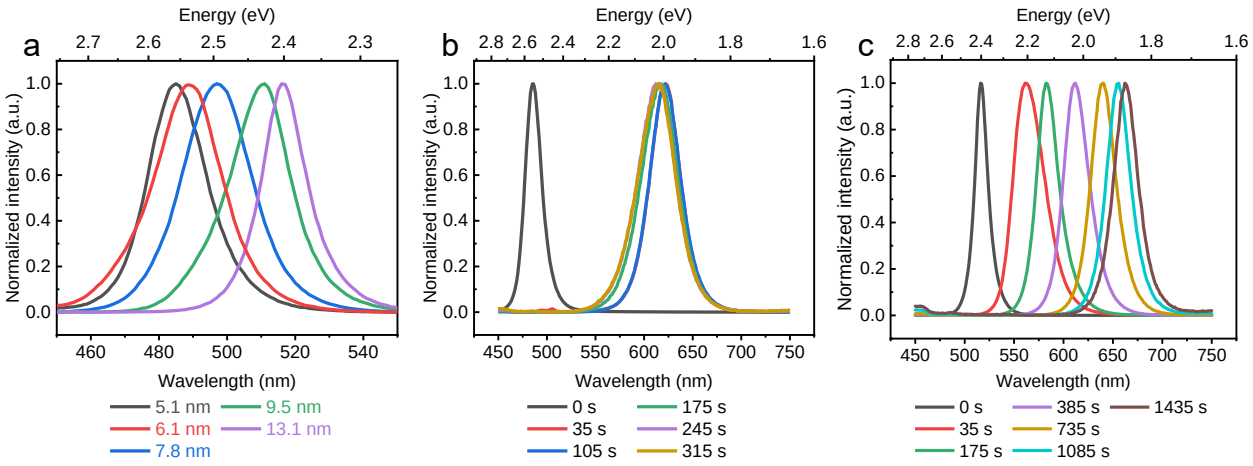

Figure 3.2. (a) PL spectra of different batches of $CsPbBr_3$ NCs showing size-dependent emission maxima. The spectra of the 6.1-nm and 7.8-nm samples were acquired using different batches of $CsPbBr_3$ NCs than those used for single-particle microscopy. They were prepared in the same way and showed nominally the same average edge length in their size histograms obtained by TEM. (b) Time evolution of PL spectra for 5.1-nm $CsPbBr_3$ NCs after the addition of excess TMSI (0.01 M, 100 µL) to induce anion exchange. (c) Time evolution of PL spectra for 13.1-nm $CsPbBr_3$ NCs after the addition of excess TMSI (0.01 M, 100 µL). Only representative spectra are shown in plots (b) and (c) to avoid overlap of the spectra.

To determine how the NC size affects the mechanism of anion exchange, we monitored the transformation of $CsPbBr_3$ NCs to $CsPbI_3$ in situ at single-particle level with fluorescence microcopy. The assembly of flow cells and the setup for single-particle experiments are described in the **Experimental section 3.2** and in our previous work.[41, 62, 63] A flow cell containing $CsPbBr_3$ NCs deposited on a microscope coverslip was placed on top of an inverted optical microscope, and a solution of TMSI was injected into the flow cell to induce anion exchange (**Figure 3.3(a)**). We chose a filter set that blocks emission from the initial $CsPbBr_3$ NCs but collects light emitted from iodide-rich $CsPbBr_xI_{3-x}$ NCs (**Figure 3.10**). As the emission from each NC shifts to longer

wavelengths during anion exchange, they appear as bright spots within the microscope field-of-view (**Figure 3.3(b, c)**). Each reaction trajectory consists of the change in fluorescence intensity for a single particle with time (**Figure 3.4**). To exclude clusters of nanocrystals within a diffraction-limited spot, only fluorescence trajectories with clear "on" (i.e., emissive) and "off" (i.e., dark) states were included for subsequent analysis (see **Figures 3.11** and **3.12** for examples), which is a signature of a single emitter. While time-correlated single-photon counting is needed to conclusively identify single emitters, our method enables us to collect the trajectories of hundreds of nanocrystals undergoing anion exchange at the same time and collect statistics for the reaction.

We define the incubation time as the time difference between when the TSMI solution first flows into the microscope field of view and when the fluorescence intensity starts to rise for the ensemble of NCs. The incubation times when using a TMSI solution with a concentration of 5 μM were 393 s for 5.1-nm, 380 s for 6.1-nm, 393 s for 7.8-nm, 773 s for 9.5-nm and 891 s for 13.1-nm $CsPbBr_3$ NCs. Thus, larger NCs tend to exhibit longer ensemble incubation times for anion exchange consistent with the slower shifts in the maxima of the ensemble PL spectra shown in **Figure 3.2** (as the transforming NCs are not observed under the microscope until their emission wavelength falls within the window of the emission filter). Further analysis of the ensemble trajectories is limited because each single NC turns on at a different time. Thus, the integrated intensities (i.e., over the entire field of view) convolve differences in when the fluorescence trajectory for each NC starts with the steepness of its intensity rise.

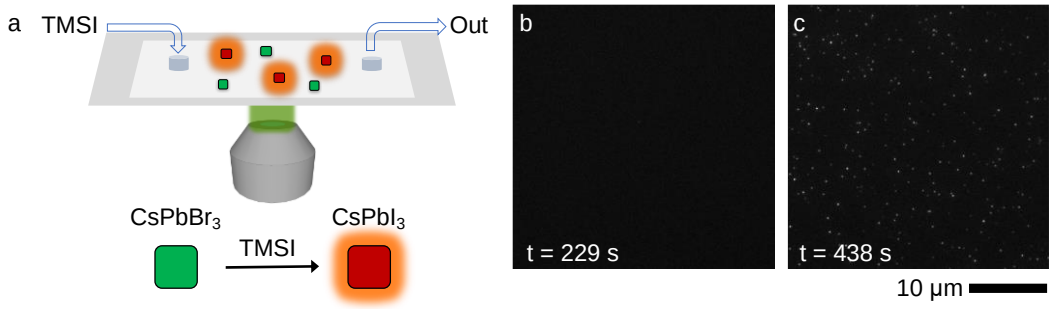

Figure 3.3. (a) Schematic of single-particle imaging of anion exchange using a flow cell placed over an inverted fluorescence microscope. The observation window of the emission filter is 590 – 649 nm (**Figure 3.10**). (b) Snapshot (t = 229 s, measured from when TMSI was injected into the flow cell) from a fluorescence video before the transformation of 13.1-nm $CsPbBr_3$ NCs. (c) Snapshot (t = 438 s) from the same fluorescence video showing the fluorescence intensity after the transformation of the NCs to $CsPbI_3$. The TMSI concentration used to induce the transformation was 12.5 μM. The background brightness of each snapshot was set to same intensity.

Our prior work has shown that the steepness of the fluorescence intensity rise of individual NCs during anion exchange is an important parameter in extracting mechanistic information for the solid-state transformation.[41, 62, 63] We next examined how the concentration of TMSI and the size of the nanocrystals affect this parameter. Representative single-particle reaction trajectories from the batches of $CsPbBr_3$ NCs with the smallest and largest average sizes (i.e., 5.1 and 13.1 nm) and using the lowest and highest TMSI concentrations (i.e., 5 and 50 μM) to induce anion exchange are shown in **Figure 3.4**. For both sizes, the intensity change during the transformation rises more steeply using the higher TMSI concentration. For the same TMSI concentration, smaller NCs undergo a more gradual increase in intensity while the larger NCs exhibit a steeper rise in their intensity trajectory during anion exchange.

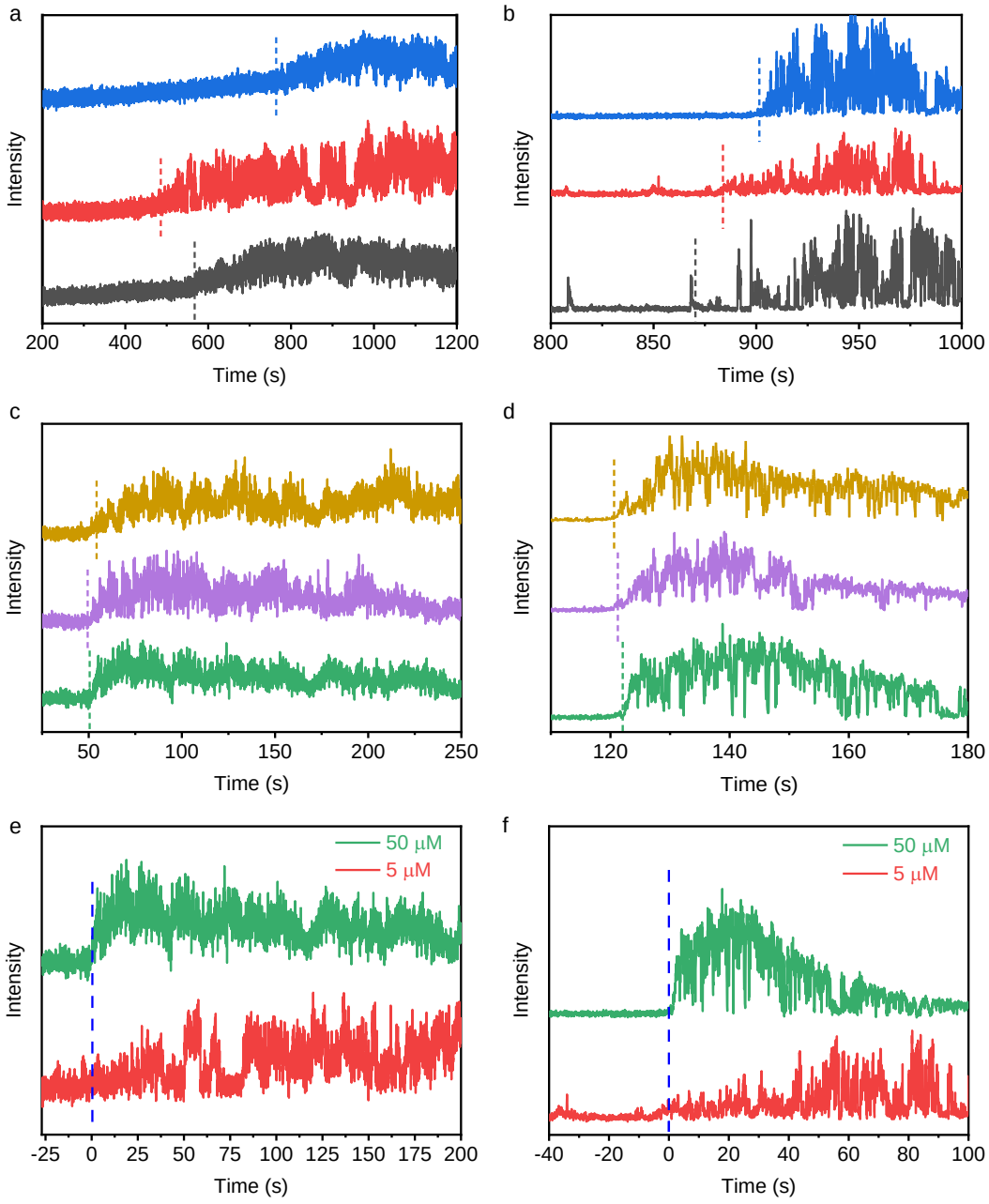

Figure 3.4. Representative single-particle fluorescence trajectories during anion exchange of $CsPbBr_3$ NCs to $CsPbI_3$. (a) Trajectories of 5.1-nm $CsPbBr_3$ NCs transformed using a TMSI solution with a concentration of 5 μM. (b) Trajectories of 13.1-nm $CsPbBr_3$ NCs transformed using a TMSI solution with a concentration of 5 μM. (c) Trajectories of 5.1-nm $CsPbBr_3$ NCs transformed using a TMSI solution with a concentration of 50 μM. (d) Trajectories of 13.1-nm

$CsPbBr_3$ NCs transformed using a TMSI solution with a concentration of 50 µM. Panels (e) and (f) compare trajectories at different TMSI concentrations. (e) Trajectories of 5.1-nm $CsPbBr_3$ NCs transformed using a TMSI solution with a concentration of 5 µM (red, middle trace in panel a) and 50 µM (green, bottom trace in panel c). (f) Trajectories of 13.1-nm $CsPbBr_3$ NCs transformed using a TMSI solution with a concentration of 5 µM (red, middle trace in panel b) and 50 µM (green, bottom trace in panel d). The vertical dashed lines indicate where the single-particle trajectories start to rise (set to 0 in panels e and f for comparison). After reaching their maximum, the PL intensity of the NCs decrease due to degradation when using TMSI with a concentration of 50 µM.

To quantify the steepness of the intensity rise for individual NCs, we fit each reaction trajectory to a sigmoidal function and extracted a switching time based on the fit (see **section 3.4** for details). A shorter switching time indicates a steeper rise in intensity. We performed single-particle microscopy on each batch of NCs with using TMSI concentrations of 5, 7.5, 10, 12.5, 15, 20, 30, and 50 µM to induce anion exchange. For each average size and TMSI concentration, we fit over 250 individual reaction trajectories. At the flow rate used to inject the TMSI solution (20 mL/h), the switching times did not show any dependence on the location of the nanocrystal within the microscope field of view (**Figure 3.13**). The mean switching times for each condition are shown in **Figure 3.5(a)** (see also **Figure 3.14** in the **Appendix B** for an expanded view of the switching times at low TMSI concentrations). For each batch of NCs, the average switching time decreases as the concentration of TMSI increases. We note that the exchange reaction initiates before emission from the $CsPbBr_{3-x}I_x$ NCs comes into view with the filter set used. For the portion of the exchange reaction that we observe, two important trends emerge as can be seen in **Figure 3.5(a)**. 1) Smaller NCs exhibit longer switching times during anion exchange. 2) The switching times of

smaller NCs exhibit a stronger concentration dependence (i.e., the switching times increase more steeply at lower TMSI concentrations). For example, as the concentration of TMSI increases from 5 μM to 50 μM, the mean switching time (± first standard deviation) decreases from 135.6 ± 37.3 s to 18.1 ± 9.4 s for the 5.1-nm NCs. For the 13.1-nm NCs, the mean switching time decreases from 14.1 ± 8.1 s to 2.7 ± 1.8 s over this concentration range. This unexpected behavior indicates that the reaction path for anion exchange is size dependent.

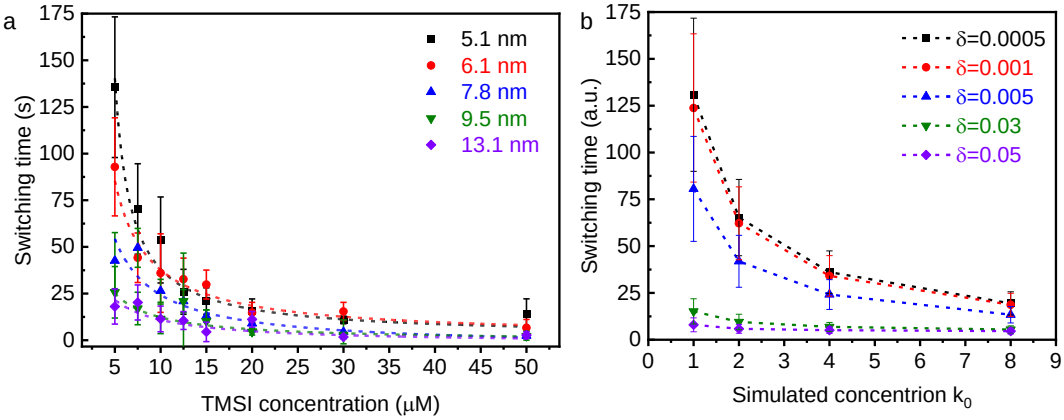

Figure 3.5. Comparison of experimental and simulated switching times for anion exchange of $CsPbBr_3$ NCs. (a) Concentration dependence of experimental switching times for $CsPbBr_3$ NCs with different sizes. Each data point represents the mean switching time from fitting the trajectories of at least 250 NCs. The TMSI concentrations used for each NC size were: 5, 7.5, 10, 12.5, 15, 20, 30, and 50 μM. (b) Simulated switching times for different values of cooperativity, δ, and concentration, k_0. Each data point represents the mean of simulated trajectories from 500 particles. The dashed lines in both panels are guides to the eye. The error bars for each data point in both plots indicate the standard deviation in the experimental/simulated switching times.

3.4 Model for size-dependent reactivity

We used Monte Carlo methods to model differences in the reaction path for particles of different sizes. The main parameter we varied in these simulations is how the reaction barrier changes for consecutive exchange events in a particle during anion exchange (see the **Appendix B** for details of the simulations). Cooperativity in the solid-state transformation was modeled by a change in free energy that decreases with successive exchange events and thus a probability for exchange that increases with successive exchange events. Previous work by us and others has shown that stronger cooperativity leads to sharper transitions and shorter switching times in the simulated trajectories for ion exchange.[41, 58, 62, 63] Stronger cooperativity also makes the switching times relatively insensitive to the concentration of substitutional ions.

In our previous work, we used single-particle fluorescence to monitor anion exchange in $CsPbBr_3$ NCs with an average size of 9.4 nm.[63] A model where the change in free energy for exchange events decreased quadratically with the number of events reproduced the concentration dependence of switching times for this size of NCs.

$$\Delta G_i = \Delta G_0 - \delta i^2 \tag{3.7}$$

Where i is the number of exchange events in a particle, ΔG_i is the change in free energy for the i^{th} exchange event, and ΔG_0 and δ are empirical constants. We adapted this model by varying the value of δ, which determines the degree of cooperativity during the simulation. As δ increases, the degree of cooperativity increases, and the probability for further exchange increases more rapidly as the reaction progresses (**Figure 3.15**). For each value of δ, the value of ΔG_0 was varied to simulate different concentrations of substitutional iodide (see **section 3.2** for details). Simulated reaction trajectories for different values of δ are shown in **Figure 3.16**. As the value of δ increases, the trajectories of individual particles become increasingly sharper relative to the ensemble

trajectory. The mean switching times for the simulations are shown in **Figure 3.5(b)**. Switching times for additional values of δ are shown in **Figure 3.17**. The values of δ shown in **Figure 3.5(b)** were chosen as they exhibit qualitatively similar concentration dependences to the experimental data. Larger values of δ lead to shorter switching times and switching times that are relatively insensitive to the simulated concentration of substitutional iodide. Based on the comparison of these simulations to experimental switching times determined by single-particle fluorescence, we associate stronger cooperativity with the transformation of larger $CsPbBr_3$ NCs.

Our results can be rationalized by a size-dependent miscibility between $CsPbBr_3$ and $CsPbI_3$ crystals at the nanoscale. Calculations using density functional theory indicate that the cubic perovskite phase becomes thermodynamically stable in both $CsPbBr_3$ and $CsPbI_3$ for small crystal sizes (edge lengths ranging from 2.7 to 10 nm for $CsPbI_3$ and from 9.7 to 48.3 nm for $CsPbBr_3$ depending on the calculation).[17, 18] Rather than a distinct phase transition between the cubic and orthorhombic perovskite phases of $CsPbI_3$, Zhao and coworkers have shown that the lattice constants and tilting of PbI_6 octahedra vary continuously for NCs in the size range of 5 to 15 nm;[16] larger NCs have the orthorhombic structure, but they become more cubic like as the size decreases. Such measurements have not been performed on $CsPbBr_3$ NCs. However, due to their different surface energies[18] and anion radii (1.82 Å for Br^- and 2.06 Å for I^-), we hypothesize that the degree of size-dependent octahedral tilting will be different between $CsPbBr_3$ and $CsPbI_3$. Our previous experiments show that switching times observed by single-particle microscopy become shorter and less sensitive to the concentration of substitutional ions as the difference between the structures of the initial and final crystals becomes greater (i.e., as the miscibility between initial and final crystals decreases).[41, 62, 63] Thus, our results are consistent with higher miscibility between $CsPbBr_3$ and $CsPbI_3$ for smaller sizes when their crystal structures are more cubic like. The

miscibility decreases for larger NC sizes due to changes in the tilting patterns of the PbX_6 octahedra that differ for the orthorhombic perovskite phases of these two materials.

A larger difference between the structures of $CsPbBr_3$ and $CsPbI_3$ for larger NC sizes requires more substantial structural reorganization during anion exchange. Smaller $CsPbBr_3$ NCs can maintain a homogeneous structure during anion exchange, consistent with the longer switching times and the stronger concentration dependence of switching times. The higher surface-to-volume ratio and shorter diffusion distances for exchange in smaller NCs also facilitate a homogeneous composition while anions are diffusing in and out.[43, 70] On the other hand, our results indicate that larger $CsPbBr_3$ NCs require nucleation of an iodide-rich phase within the $CsPbBr_3$ NCs. Once the iodide-rich phase has formed, lattice strain between the bromide-rich and iodide-rich regions creates a driving force for the NC to completely transform to $CsPbI_3$ (thus leading to the stronger cooperativity). This mechanism is consistent with the shorter switching times, particularly at low concentrations of TMSI that we observe as the size of the $CsPbBr_3$ NCs increases. This mechanism is also consistent with the Monte Carlo simulations that show a higher degree of cooperativity is associated with a larger amount of structural reorganization. Finally, these results are consistent with previously reported time-correlated, single-photon counting of $CsPbBr_3$ NCs during anion exchange to $CsPbI_3$. Masuo and coworkers showed that $CsPbBr_3$ NCs with an average size of 7.8 nm behaved as single-photon emitters during anion exchange, indicating a homogenous structure throughout the reaction.[64] When this group performed the same studies on $CsPbBr_3$ NCs with an average size of 19.0 nm, they observed a change in the number of emission sites during anion exchange,[66] which they attributed to the presence of distinct iodide-rich and bromide-rich regions within the NC during anion exchange.

3.5 Conclusions

This work demonstrates that the size-dependent structure of lead halide perovskite nanocrystals impacts their chemical reactivity. Through single-particle fluorescence microscopy, we observe shorter switching times during the transformation of larger $CsPbBr_3$ NCs to $CsPbI_3$ via anion exchange. Monte Carlo simulations support a more abrupt change in structure after the anion exchange reaction initiates for larger NCs, which requires nucleation of a new phase. On the other hand, smaller NCs can maintain a homogenous composition and structure during the exchange reaction leading to longer switching times at lower concentrations of substitutional halide ions. While our results show that batches of colloidal nanocrystals with different average sizes exhibit different reactivity, there is significant heterogeneity within each batch in the switching times of individual nanocrystals (the vertical lines in **Figure 3.5(a)** show the standard deviation in mean switching times). Our results suggest that the variations in switching times for anion exchange within a sample are due in part to the dispersity in size of the nanocrystals. This heterogeneity is important to consider when scaling up the production of cesium lead halide nanocrystals for incorporation into optoelectronic devices. Variations in the size of the nanocrystals can not only broaden the range of emission wavelengths due to quantum-confinement effects, but they can also lead to different reactivity (and thus variations in composition) for individual nanocrystals when targeting a specific composition and emission wavelength through anion exchange. Future work includes understanding how the size-dependent miscibility and switching times affect the presence and distribution of defects introduced during anion exchange.

3.6 Appendix B

3.6.1 Tables

Table 3.1. Maxima in the PL spectra and their full width at half-maximum (FWHM) for $CsPbBr_3$ NCs with different sizes.

Size (nm)	PL max (nm)	PL max (eV)	FWHM (nm)	FWHM (eV)
5.1 ± 0.6	485	2.56	20.20	0.11
6.1 ± 0.8	489	2.54	23.62	0.12
7.8 ± 1.2	502	2.47	32.06	0.16
9.5 ± 1.5	511	2.43	21.27	0.10
13.1 ± 2.0	516	2.40	15.68	0.07

3.6.2 Figures

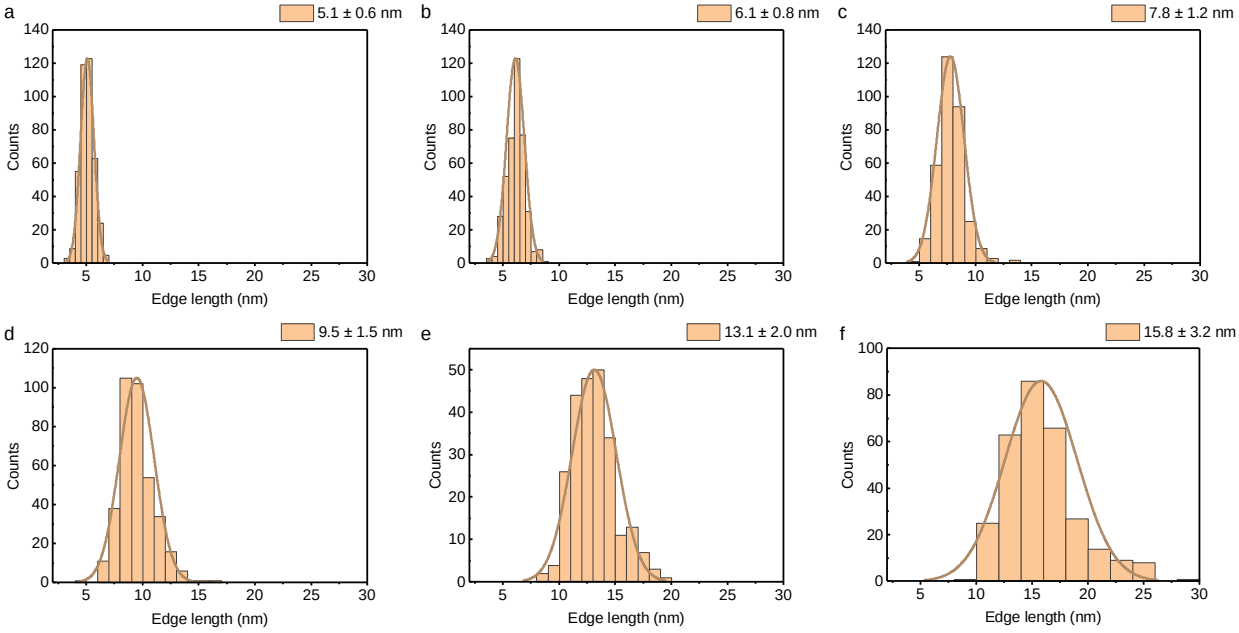

Figure 3.6. Size distributions of the $CsPbBr_3$ NCs shown in **Figure 3.1**. The average edge length and first standard deviation in the edge length for four batches of NCs are (a) 5.1 ± 0.6 nm, (b) 6.1 ± 0.8 nm, (c) 7.8 ± 1.2 nm, and (d) 9.5 ± 1.5 nm. For the largest batch of NCs, which includes rectangular particles, the shorter edge is (e) 13.1 ± 2.0 nm, and the longer edge (f) is 15.8 ± 3.2 nm.

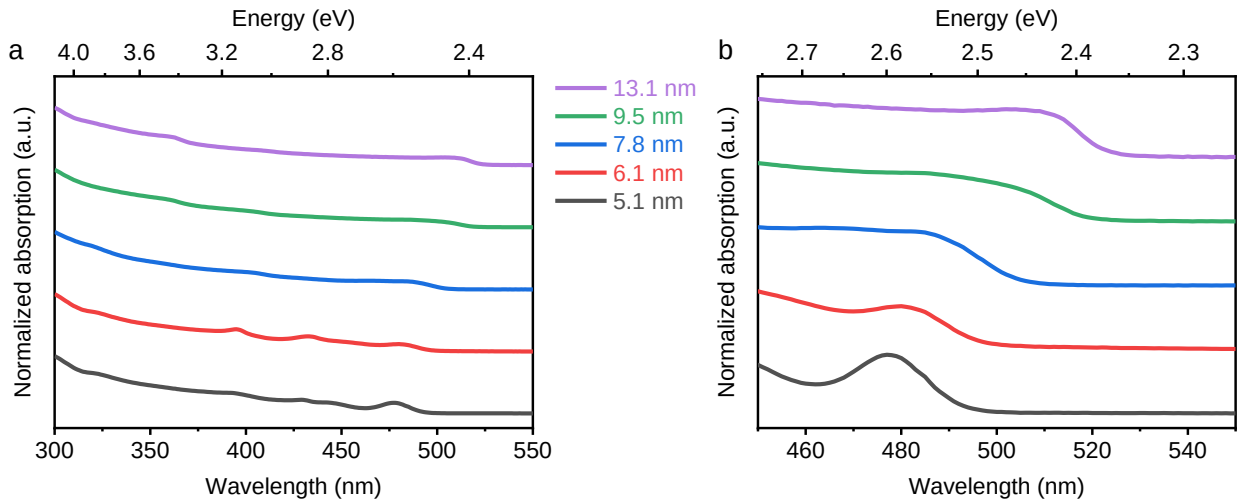

Figure 3.7. (a) UV-visible absorption spectra of $CsPbBr_3$ NCs with different sizes. (b) Magnified view of the absorption spectra showing the change in the energy of the first exciton absorption with NC size. The spectra have been vertically offset for clarity.

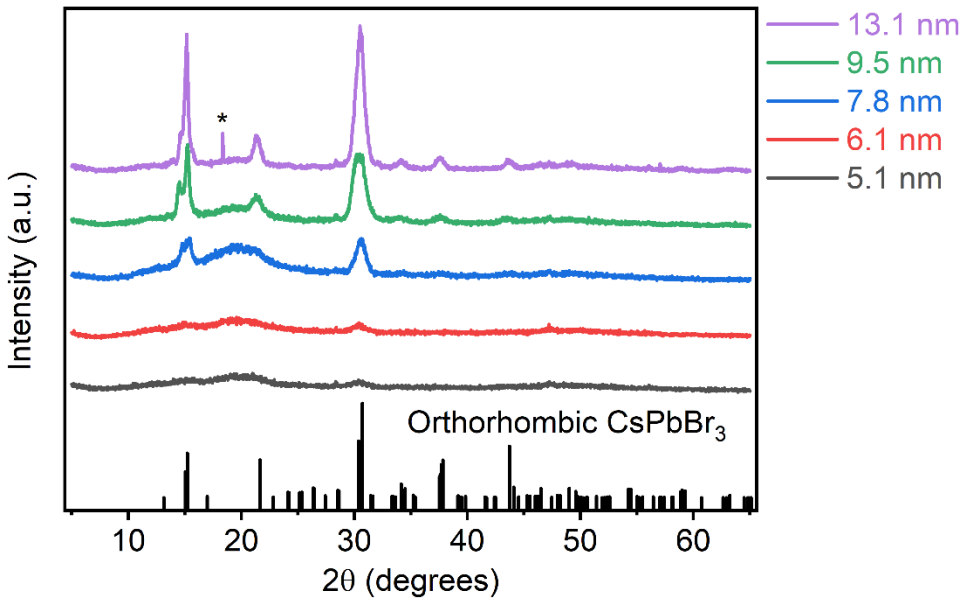

Figure 3.8. XRD patterns of $CsPbBr_3$ NCs with different sizes. The diffraction peaks broaden and decrease in intensity as the average size of the NCs decreases as a result of Scherrer broadening due to the finite size of the crystals. The impurity peak marked with an asterisk in the purple pattern (13.1 nm) is attributed to $PbBr_2$ from degradation of the $CsPbBr_3$ NCs. The vertical black lines at the bottom of the plot provide the standard pattern for orthorhombic $CsPbBr_3$ (PDF card # 04-014-9676).

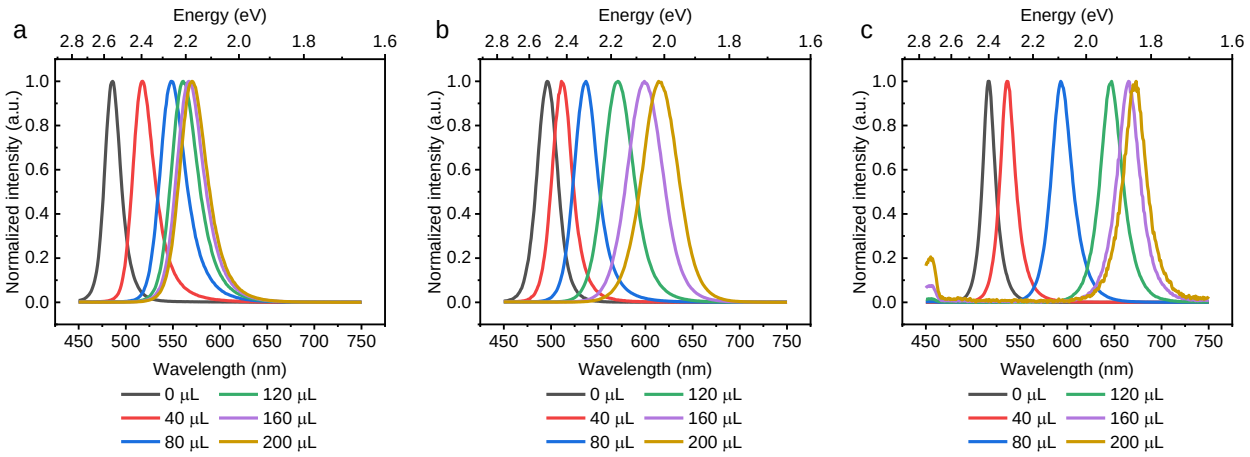

Figure 3.9. (a) Photoluminescence (PL) spectra of 5.1-nm $CsPbBr_3$ NCs after the addition of increasing amounts of a 0.001 M solution of TMSI in hexane. (b) PL spectra of 7.8-nm $CsPbBr_3$ NCs after the addition of increasing amounts of a 0.001 M solution of TMSI. (c) PL spectra of 13.1-nm $CsPbBr_3$ NCs after the addition of increasing amounts of a 0.001 M solution of TMSI. Aliquots (20 μL) of the TMSI solution were sequentially added to the cuvette containing the solution of $CsPbBr_3$ NCs. The total volume of the TMSI solution added before each spectrum was obtained is provided in the legend. All PL spectra were normalized to same maximum intensity.

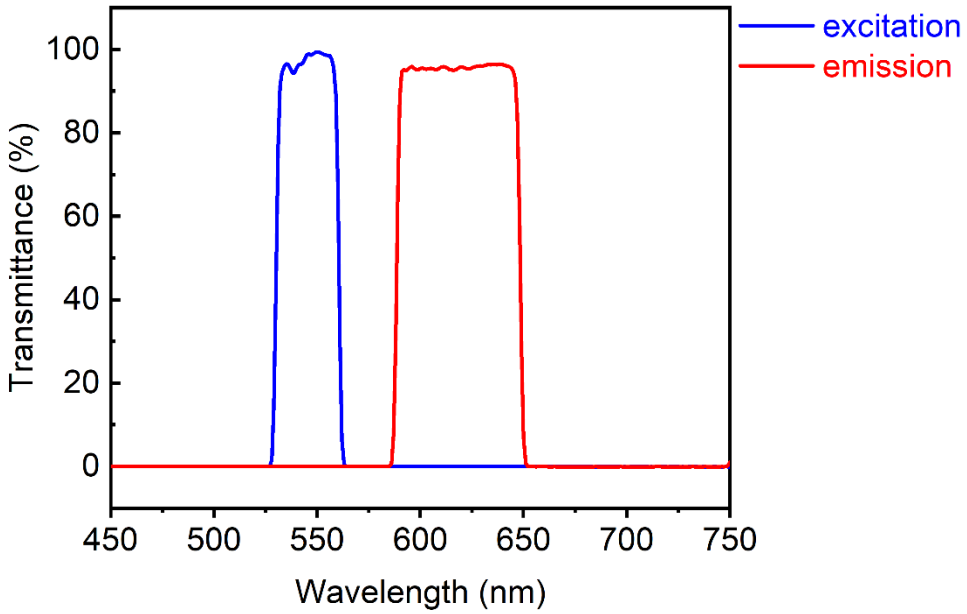

Figure 3.10. Transmittance spectra of the excitation filter (blue trace) and the combination of the emission filter and dichroic mirror (red trace) using to image anion exchange through single-particle fluorescence microscopy.

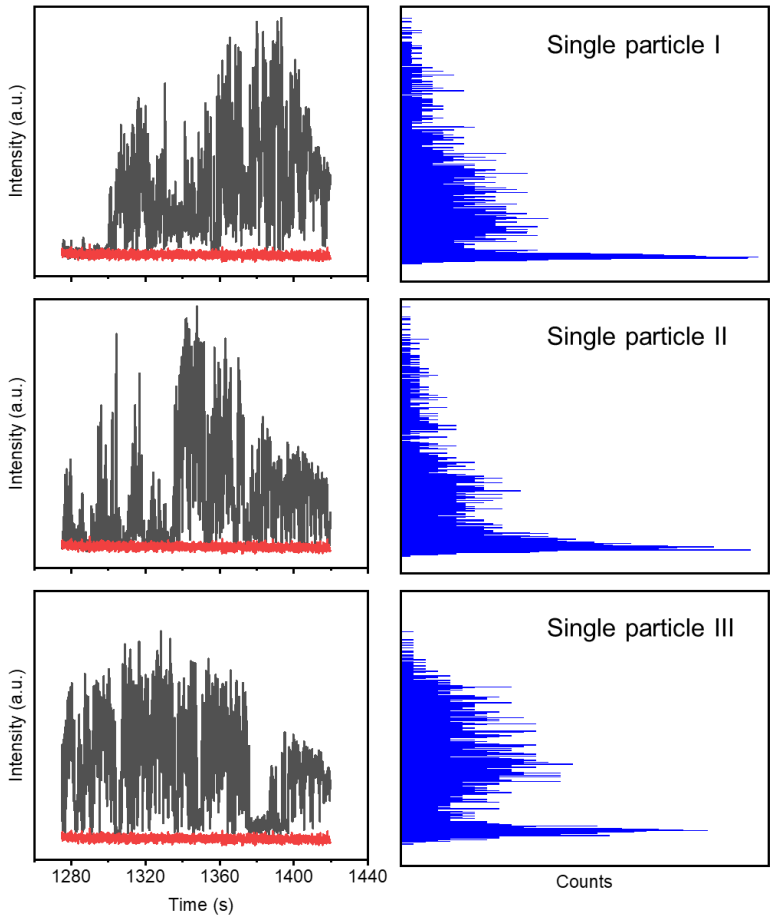

Figure 3.11. Representative intensity trajectories for single iodide-rich $CsPbBr_{3-x}I_x$ NCs following the transformation of $CsPbBr_3$ NCs with a size of 9.5 nm and using a TMSI concentration of 5 μM. Each of the black traces on the left-hand side is a segment of the trajectory after the intensity stopped increasing (i.e., following the exchange reaction). Each of the red traces shows the background intensity in a nearby region not containing any particles. The blue histograms on the right-hand side show the intensity distributions of the black traces. Intensity trajectories that exhibit fluorescence intermittency with clear off states are indicative of single particles.

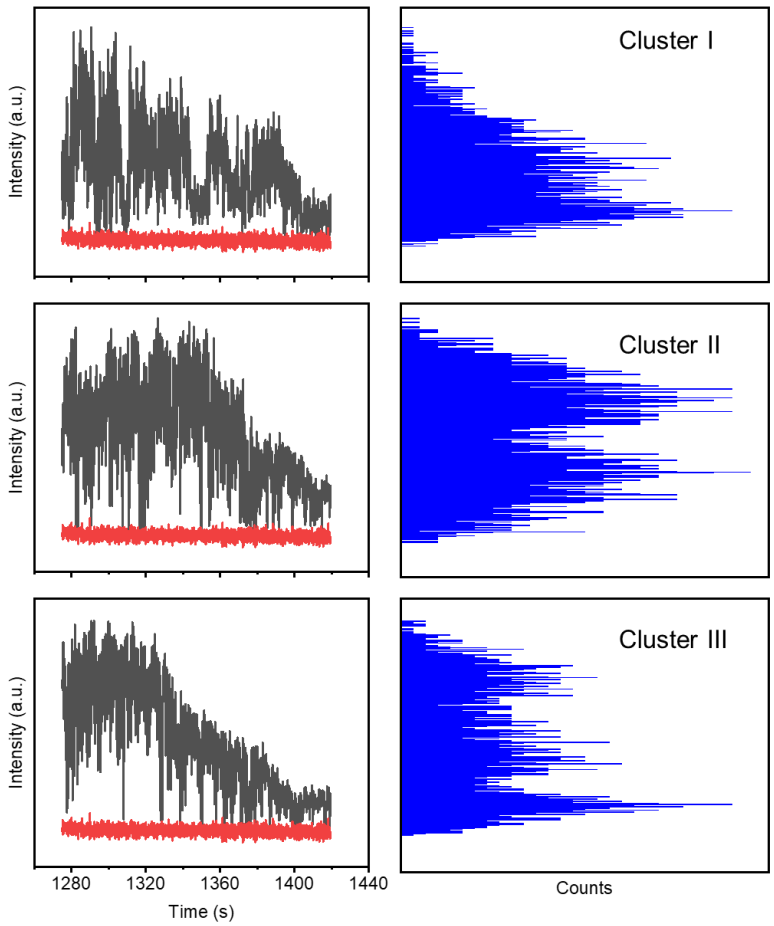

Figure 3.12. Representative intensity trajectories of clusters of $CsPbBr_{3-x}I_x$ NCs following the transformation $CsPbBr_3$ NCs with a size of 9.5 nm and using a TMSI concentration of 5 μM. Each of the black traces on the left-hand side is a segment of the trajectory after the intensity stopped increasing (i.e., following the exchange reaction). Each of the red traces shows the background intensity in a nearby region not containing any particles. The blue histograms on the right-hand side show the intensity distributions of the black traces. Unlike the trajectories for single particles shown in **Figure 3.11** above, clusters of particles do not show clear off states as each particle in the cluster blinks independently. Clusters of particles were not used in further analysis of the switching times.

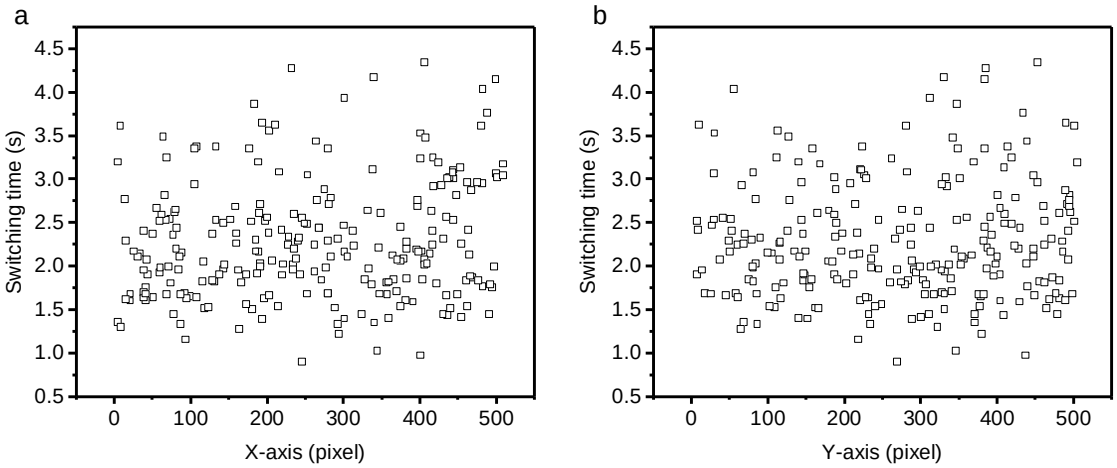

Figure 3.13. Representative switching times for different NCs as a function of position along the (a) x-axis and (b) y-axis of the microscope field of view. The sample consisted of $CsPbBr_3$ NCs with an average size of 9.5 nm. A TMSI solution with a concentration of 50 μM was used to induce anion exchange. This representative example shows that switching times are independent of where the NC is located within the microscope field of view.

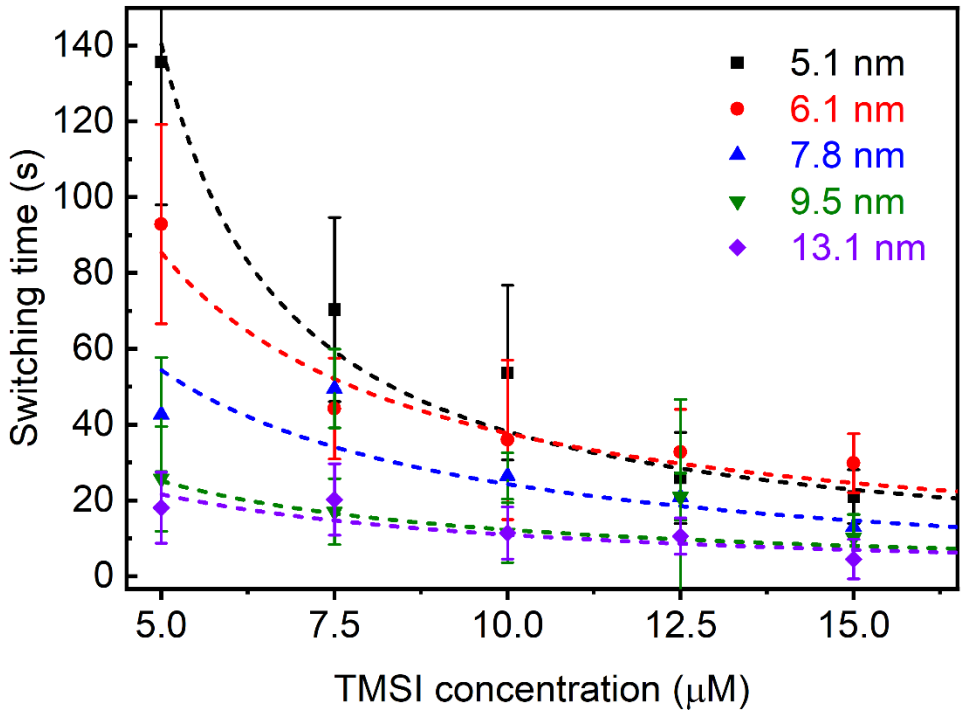

Figure 3.14. Concentration dependence of switching times for $CsPbBr_3$ NCs with different average sizes. The TMSI concentrations used for each NC size were: 5, 7.5, 10, 12.5, and 15 μM. These data are the same as those in **Figure 3.5(a)**; the plot is expanded here to show the switching times at low TMSI concentrations.

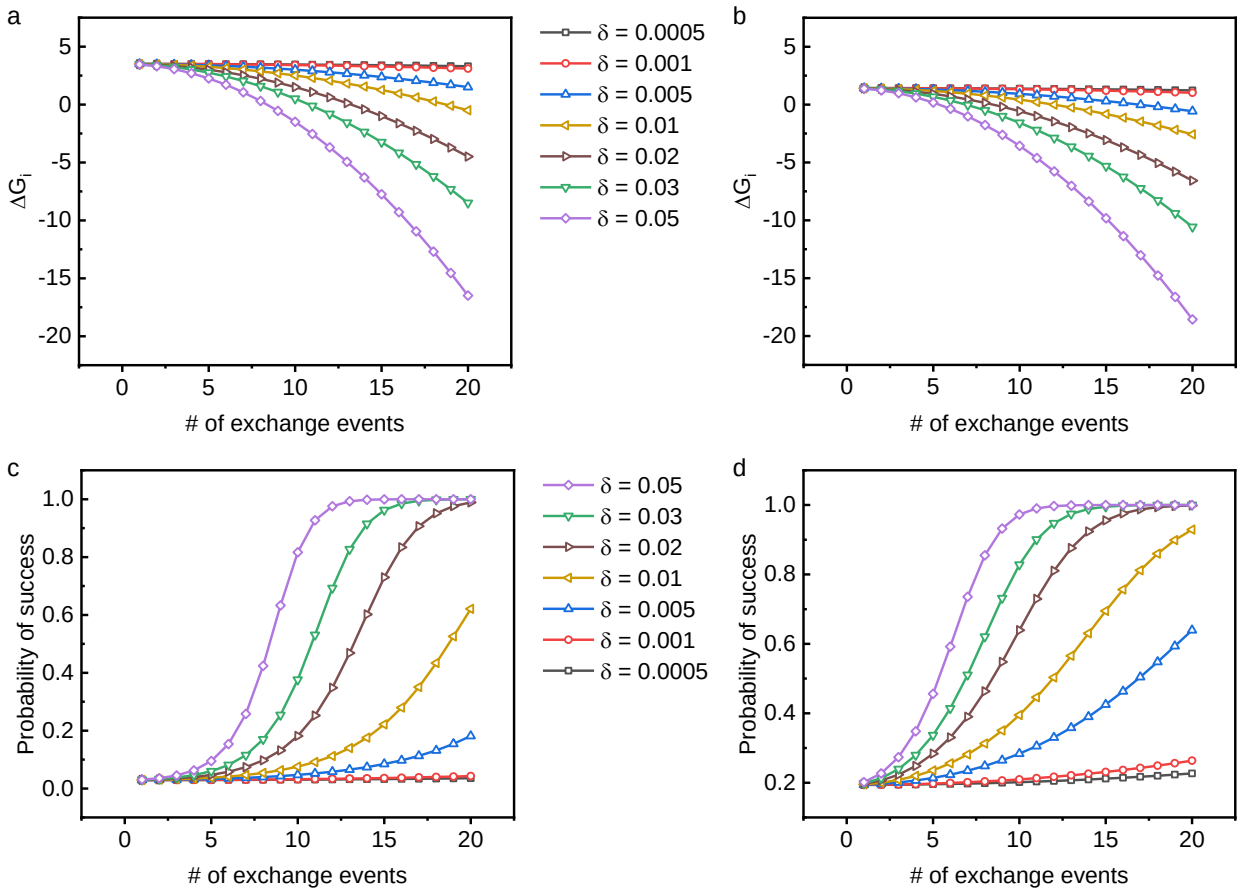

Figure 3.15. (a, b) Simulated changes in the free energy, ΔG_i, for anion exchange as the number of exchange events, i, in a particle increases. Increasing values of δ for the different curves represent increasing cooperativity for anion exchange. (a) ΔG_i for the lowest simulated concentration ($k_0 = 1$). (b) ΔG_i for the highest simulated concentration ($k_0 = 8$). (c, d) Simulated probabilities for anion exchange as i increases. (c) Probability for the lowest simulated concentration ($k_0 = 1$). (d) Probability for the highest simulated concentration ($k_0 = 8$).

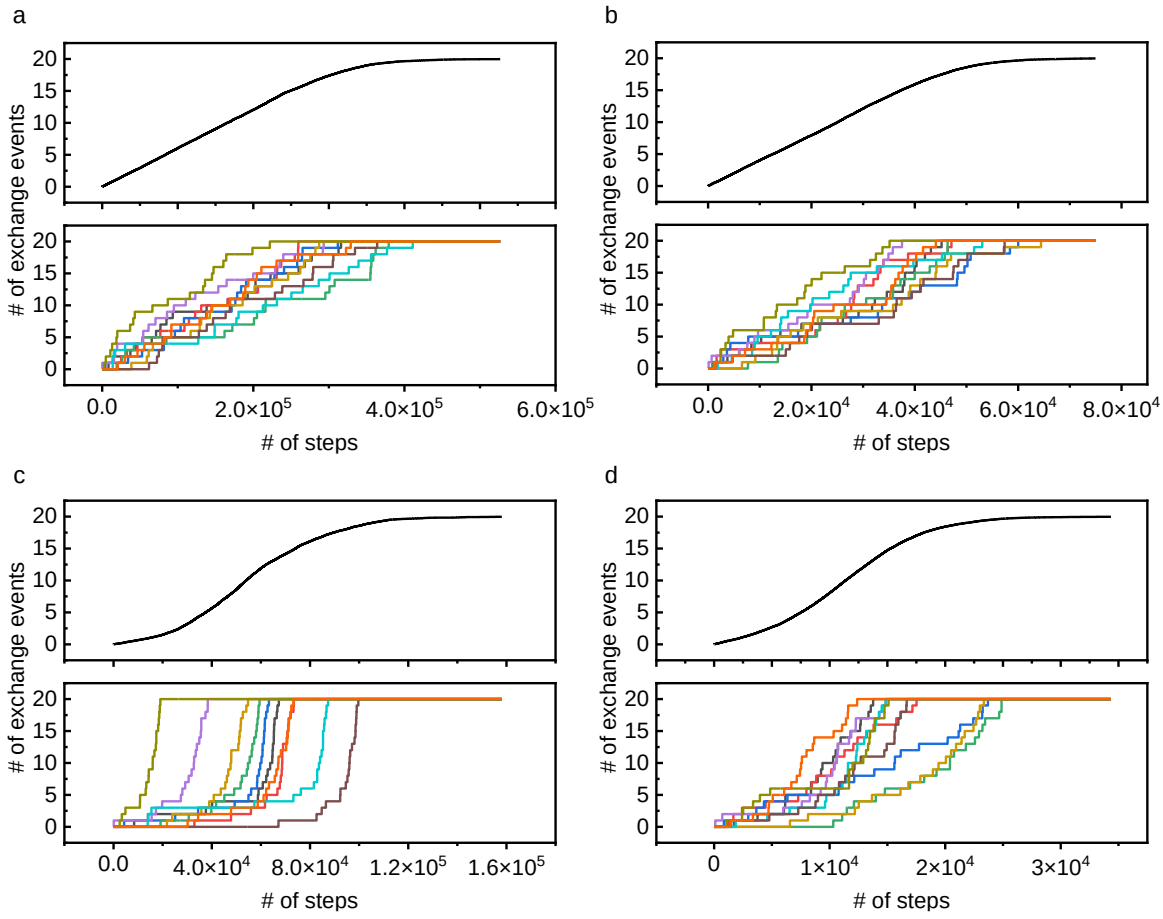

Figure 3.16. Simulated trajectories for anion exchange. For each panel, the top plot shows the average reaction trajectory for an ensemble of 500 particles, and the bottom plot shows representative trajectories for single particles. (a) Simulated trajectories using the smallest degree of cooperativity ($\delta = 0.0005$) and the lowest concentration ($k_0 = 1$). (b) Simulated trajectories using the smallest degree of cooperativity ($\delta = 0.0005$) and the highest concentration ($k_0 = 8$). (c) Simulated trajectories using the largest degree of cooperativity ($\delta = 0.05$) and the lowest concentration ($k_0 = 1$). (b) Simulated trajectories using the largest degree of cooperativity ($\delta = 0.05$) and the highest concentration ($k_0 = 8$).

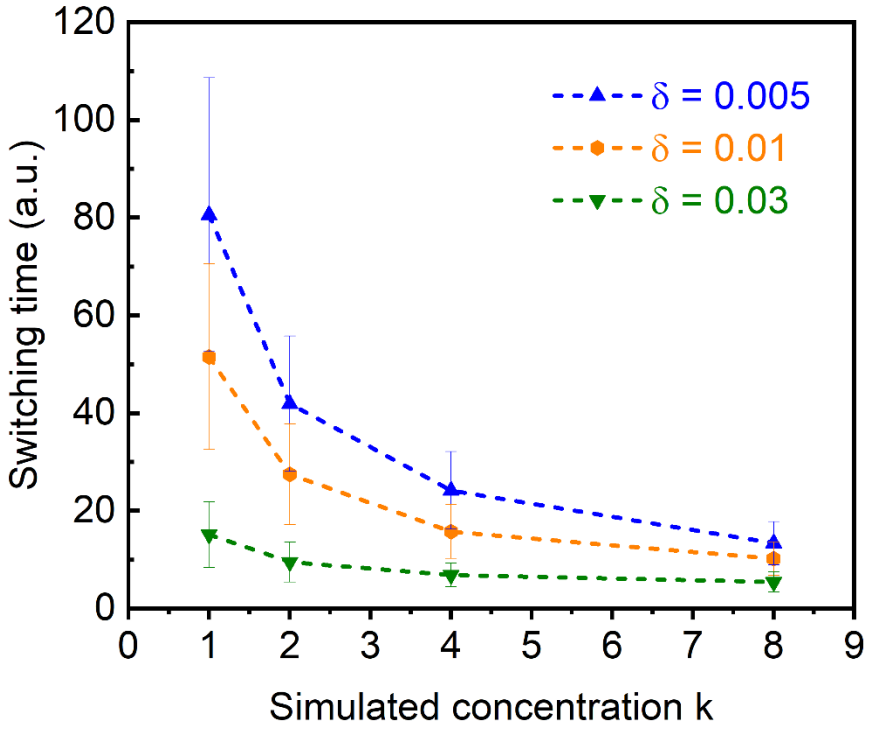

Figure 3.17. Simulated switching times for different values of δ and k_0. This plot shows the switching times for additional values of δ that are not shown in **Figure 3.5(b)**. The dashed lines are guides to the eye. The error bars for each data point indicate the standard deviation in the simulated switching times.

3.7 References

1. Rossetti, R.; Nakahara, S.; Brus, L. E., Quantum size effects in the redox potentials, resonance Raman spectra, and electronic spectra of CdS crystallites in aqueous solution. *The Journal of Chemical Physics* **1983,** *79* (2), 1086-1088.

2. Goldstein, A. N.; Echer, C. M.; Alivisatos, A. P., Melting in Semiconductor Nanocrystals. *Science* **1992,** *256* (5062), 1425-1427.

3. Murray, C. B.; Norris, D. J.; Bawendi, M. G., Synthesis and characterization of nearly monodisperse CdE (E = sulfur, selenium, tellurium) semiconductor nanocrystallites. *Journal of the American Chemical Society* **1993,** *115* (19), 8706-8715.

4. Dabbousi, B. O.; Rodriguez-Viejo, J.; Mikulec, F. V.; Heine, J. R.; Mattoussi, H.; Ober, R.; Jensen, K. F.; Bawendi, M. G., (CdSe)ZnS Core−Shell Quantum Dots: Synthesis and Characterization of a Size Series of Highly Luminescent Nanocrystallites. *The Journal of Physical Chemistry B* **1997,** *101* (46), 9463-9475.

5. Tolbert, S. H.; Alivisatos, A. P., Size Dependence of a First Order Solid-Solid Phase Transition: The Wurtzite to Rock Salt Transformation in CdSe Nanocrystals. *Science* **1994,** *265* (5170), 373-376.

6. Tolbert, S. H.; Alivisatos, A. P., The wurtzite to rock salt structural transformation in CdSe nanocrystals under high pressure. *The Journal of Chemical Physics* **1995,** *102* (11), 4642-4656.

7. Alivisatos, A. P., Perspectives on the Physical Chemistry of Semiconductor Nanocrystals. *The Journal of Physical Chemistry* **1996,** *100* (31), 13226-13239.

8. Chen, C.-C.; Herhold, A. B.; Johnson, C. S.; Alivisatos, A. P., Size Dependence of Structural Metastability in Semiconductor Nanocrystals. *Science* **1997,** *276* (5311), 398-401.

9. Jacobs, K.; Zaziski, D.; Scher, E. C.; Herhold, A. B.; Paul Alivisatos, A., Activation Volumes for Solid-Solid Transformations in Nanocrystals. *Science* **2001,** *293* (5536), 1803-1806.

10. Yu, W. W.; Wang, Y. A.; Peng, X., Formation and Stability of Size-, Shape-, and Structure-Controlled CdTe Nanocrystals: Ligand Effects on Monomers and Nanocrystals. *Chemistry of Materials* **2003,** *15* (22), 4300-4308.

11. Hines, M. A.; Scholes, G. D., Colloidal PbS Nanocrystals with Size-Tunable Near-Infrared Emission: Observation of Post-Synthesis Self-Narrowing of the Particle Size Distribution. *Advanced Materials* **2003,** *15* (21), 1844-1849.

12. Mclaren, A.; Valdes-Solis, T.; Li, G.; Tsang, S. C., Shape and size effects of ZnO nanocrystals on photocatalytic activity. *Journal of the American Chemical Society* **2009,** *131* (35), 12540-12541.

13. Mastronardi, M. L.; Maier-Flaig, F.; Faulkner, D.; Henderson, E. J.; Kübel, C.; Lemmer, U.; Ozin, G. A., Size-Dependent Absolute Quantum Yields for Size-Separated Colloidally-Stable Silicon Nanocrystals. *Nano Letters* **2012,** *12* (1), 337-342.

14. Yu, Y.; Fan, G.; Fermi, A.; Mazzaro, R.; Morandi, V.; Ceroni, P.; Smilgies, D.-M.; Korgel, B. A., Size-Dependent Photoluminescence Efficiency of Silicon Nanocrystal Quantum Dots. *The Journal of Physical Chemistry C* **2017,** *121* (41), 23240-23248.

15. Liu, C.; Zheng, L.; Song, Q.; Xue, Z.; Huang, C.; Liu, L.; Qiao, X.; Li, X.; Liu, K.; Wang, T., A Metastable Crystalline Phase in Two-Dimensional Metallic Oxide Nanoplates. *Angewandte Chemie International Edition* **2019,** *58* (7), 2055-2059.

16. Zhao, Q.; Hazarika, A.; Schelhas, L. T.; Liu, J.; Gaulding, E. A.; Li, G.; Zhang, M.; Toney, M. F.; Sercel, P. C.; Luther, J. M., Size-Dependent Lattice Structure and Confinement Properties in $CsPbI_3$ Perovskite Nanocrystals: Negative Surface Energy for Stabilization. *ACS Energy Letters* **2020,** *5* (1), 238-247.

17. Feng Yang, C. W., Yuhao Pan, Xieyu Zhou, Xianghua Kong, Wei Ji, Surface stabilized cubic phase of $CsPbI_3$ and $CsPbBr_3$ at room temperature. *Chinese Physics B* **2019,** *28* (5), 56402-056402.

18. Yang, R. X.; Tan, L. Z., Understanding size dependence of phase stability and band gap in $CsPbI_3$ perovskite nanocrystals. *The Journal of Chemical Physics* **2020,** *152* (3), 034702.

19. Burschka, J.; Pellet, N.; Moon, S.-J.; Humphry-Baker, R.; Gao, P.; Nazeeruddin, M. K.; Grätzel, M., Sequential deposition as a route to high-performance perovskite-sensitized solar cells. *Nature* **2013,** *499*, 316-319.

20. Chen, Q.; Zhou, H.; Hong, Z.; Luo, S.; Duan, H.-S.; Wang, H.-H.; Liu, Y.; Li, G.; Yang, Y., Planar Heterojunction Perovskite Solar Cells via Vapor-Assisted Solution Process. *Journal of the American Chemical Society* **2014,** *136* (2), 622-625.

21. Green, M. A.; Ho-Baillie, A.; Snaith, H. J., The emergence of perovskite solar cells. *Nature Photonics* **2014,** *8* (7), 506-514.

22. Lin, Q.; Armin, A.; Nagiri, R. C. R.; Burn, P. L.; Meredith, P., Electro-optics of perovskite solar cells. *Nature Photonics* **2014,** *9*, 106.

23. Jeon, N. J.; Noh, J. H.; Yang, W. S.; Kim, Y. C.; Ryu, S.; Seo, J.; Seok, S. I., Compositional engineering of perovskite materials for high-performance solar cells. *Nature* **2015,** *517*, 476-480.

24. Swarnkar, A.; Marshall, A. R.; Sanehira, E. M.; Chernomordik, B. D.; Moore, D. T.; Christians, J. A.; Chakrabarti, T.; Luther, J. M., Quantum dot–induced phase stabilization of α-$CsPbI_3$ perovskite for high-efficiency photovoltaics. *Science* **2016,** *354* (6308), 92-95.

25. Xiao, Z.; Kerner, R. A.; Zhao, L.; Tran, N. L.; Lee, K. M.; Koh, T.-W.; Scholes, G. D.; Rand, B. P., Efficient perovskite light-emitting diodes featuring nanometre-sized crystallites.

Nature Photonics **2017,** *11* (2), 108-115.

26. Zhao, L.; Yeh, Y.-W.; Tran, N. L.; Wu, F.; Xiao, Z.; Kerner, R. A.; Lin, Y. L.; Scholes, G. D.; Yao, N.; Rand, B. P., In Situ Preparation of Metal Halide Perovskite Nanocrystal Thin Films for Improved Light-Emitting Devices. *ACS Nano* **2017,** *11* (4), 3957-3964.

27. Lee, S.; Park, J. H.; Nam, Y. S.; Lee, B. R.; Zhao, B.; Di Nuzzo, D.; Jung, E. D.; Jeon, H.; Kim, J.-Y.; Jeong, H. Y.; Friend, R. H.; Song, M. H., Growth of Nanosized Single Crystals for Efficient Perovskite Light-Emitting Diodes. *ACS Nano* **2018,** *12* (4), 3417-3423.

28. Protesescu, L.; Yakunin, S.; Bodnarchuk, M. I.; Krieg, F.; Caputo, R.; Hendon, C. H.; Yang, R. X.; Walsh, A.; Kovalenko, M. V., Nanocrystals of Cesium Lead Halide Perovskites ($CsPbX_3$, X = Cl, Br, and I): Novel Optoelectronic Materials Showing Bright Emission with Wide Color Gamut. *Nano Letters* **2015,** *15* (6), 3692-3696.

29. Bekenstein, Y.; Koscher, B. A.; Eaton, S. W.; Yang, P.; Alivisatos, A. P., Highly Luminescent Colloidal Nanoplates of Perovskite Cesium Lead Halide and Their Oriented Assemblies. *Journal of the American Chemical Society* **2015,** *137* (51), 16008-16011.

30. Zhu, F.; Men, L.; Guo, Y.; Zhu, Q.; Bhattacharjee, U.; Goodwin, P. M.; Petrich, J. W.; Smith, E. A.; Vela, J., Shape Evolution and Single Particle Luminescence of Organometal Halide Perovskite Nanocrystals. *ACS Nano* **2015,** *9* (3), 2948-2959.

31. Di Stasio, F.; Christodoulou, S.; Huo, N.; Konstantatos, G., Near-Unity Photoluminescence Quantum Yield in $CsPbBr_3$ Nanocrystal Solid-State Films via Postsynthesis Treatment with Lead Bromide. *Chemistry of Materials* **2017,** *29* (18), 7663-7667.

32. Rainò, G.; Becker, M. A.; Bodnarchuk, M. I.; Mahrt, R. F.; Kovalenko, M. V.; Stöferle, T., Superfluorescence from lead halide perovskite quantum dot superlattices. *Nature* **2018,** *563* (7733), 671-675.

33. Akkerman, Q. A.; Abdelhady, A. L.; Manna, L., Zero-Dimensional Cesium Lead Halides: History, Properties, and Challenges. *The Journal of Physical Chemistry Letters* **2018,** *9* (9), 2326-2337.

34. Utzat, H.; Sun, W.; Kaplan, A. E. K.; Krieg, F.; Ginterseder, M.; Spokoyny, B.; Klein, N. D.; Shulenberger, K. E.; Perkinson, C. F.; Kovalenko, M. V.; Bawendi, M. G., Coherent single-photon emission from colloidal lead halide perovskite quantum dots. *Science* **2019,** *363* (6431), 1068-1072.

35. Nedelcu, G.; Protesescu, L.; Yakunin, S.; Bodnarchuk, M. I.; Grotevent, M. J.; Kovalenko, M. V., Fast Anion-Exchange in Highly Luminescent Nanocrystals of Cesium Lead Halide Perovskites ($CsPbX_3$, X = Cl, Br, I). *Nano Letters* **2015,** *15* (8), 5635-5640.

36. Pellet, N.; Teuscher, J.; Maier, J.; Grätzel, M., Transforming Hybrid Organic Inorganic Perovskites by Rapid Halide Exchange. *Chemistry of Materials* **2015,** *27* (6), 2181-2188.

37. Jang, D. M.; Park, K.; Kim, D. H.; Park, J.; Shojaei, F.; Kang, H. S.; Ahn, J.-P.; Lee, J.

W.; Song, J. K., Reversible Halide Exchange Reaction of Organometal Trihalide Perovskite Colloidal Nanocrystals for Full-Range Band Gap Tuning. *Nano Letters* **2015,** *15* (8), 5191-5199.

38. Akkerman, Q. A.; D'Innocenzo, V.; Accornero, S.; Scarpellini, A.; Petrozza, A.; Prato, M.; Manna, L., Tuning the Optical Properties of Cesium Lead Halide Perovskite Nanocrystals by Anion Exchange Reactions. *Journal of the American Chemical Society* **2015,** *137* (32), 10276-10281.

39. Li, M.; Zhang, X.; Lu, S.; Yang, P., Phase transformation, morphology control, and luminescence evolution of cesium lead halide nanocrystals in the anion exchange process. *RSC Advances* **2016,** *6* (105), 103382-103389.

40. Creutz, S. E.; Crites, E. N.; De Siena, M. C.; Gamelin, D. R., Anion Exchange in Cesium Lead Halide Perovskite Nanocrystals and Thin Films Using Trimethylsilyl Halide Reagents. *Chemistry of Materials* **2018,** *30* (15), 4887-4891.

41. Wang, D.; Cavin, J.; Yin, B.; Thind, A. S.; Borisevich, A. Y.; Mishra, R.; Sadtler, B., Role of Solid-State Miscibility during Anion Exchange in Cesium Lead Halide Nanocrystals Probed by Single-Particle Fluorescence. *The Journal of Physical Chemistry Letters* **2020,** *11* (3), 952-959.

42. Cottingham, P.; Brutchey, R. L., Compositionally Dependent Phase Identity of Colloidal $CsPbBr_{3-x}I_x$ Quantum Dots. *Chemistry of Materials* **2016,** *28* (21), 7574-7577.

43. Haque, A.; Ravi, V. K.; Shanker, G. S.; Sarkar, I.; Nag, A.; Santra, P. K., Internal Heterostructure of Anion-Exchanged Cesium Lead Halide Nanocubes. *The Journal of Physical Chemistry C* **2018,** *122* (25), 13399-13406.

44. Koscher, B. A.; Bronstein, N. D.; Olshansky, J. H.; Bekenstein, Y.; Alivisatos, A. P., Surface- vs Diffusion-Limited Mechanisms of Anion Exchange in $CsPbBr_3$ Nanocrystal Cubes Revealed through Kinetic Studies. *Journal of the American Chemical Society* **2016,** *138* (37), 12065-12068.

45. Loiudice, A.; Strach, M.; Saris, S.; Chernyshov, D.; Buonsanti, R., Universal Oxide Shell Growth Enables in Situ Structural Studies of Perovskite Nanocrystals during the Anion Exchange Reaction. *Journal of the American Chemical Society* **2019,** *141* (20), 8254-8263.

46. Empedocles, S.; Bawendi, M., Spectroscopy of Single CdSe Nanocrystallites. *Accounts of Chemical Research* **1999,** *32* (5), 389-396.

47. Park, Y.-S.; Guo, S.; Makarov, N. S.; Klimov, V. I., Room Temperature Single-Photon Emission from Individual Perovskite Quantum Dots. *ACS Nano* **2015,** *9* (10), 10386-10393.

48. Orfield, N. J.; McBride, J. R.; Keene, J. D.; Davis, L. M.; Rosenthal, S. J., Correlation of Atomic Structure and Photoluminescence of the Same Quantum Dot: Pinpointing Surface and Internal Defects That Inhibit Photoluminescence. *ACS Nano* **2015,** *9* (1), 831-839.

49. Orfield, N. J.; McBride, J. R.; Wang, F.; Buck, M. R.; Keene, J. D.; Reid, K. R.; Htoon,

H.; Hollingsworth, J. A.; Rosenthal, S. J., Quantum Yield Heterogeneity among Single Nonblinking Quantum Dots Revealed by Atomic Structure-Quantum Optics Correlation. *ACS Nano* **2016,** *10* (2), 1960-1968.

50. Rainò, G.; Nedelcu, G.; Protesescu, L.; Bodnarchuk, M. I.; Kovalenko, M. V.; Mahrt, R. F.; Stöferle, T., Single Cesium Lead Halide Perovskite Nanocrystals at Low Temperature: Fast Single-Photon Emission, Reduced Blinking, and Exciton Fine Structure. *ACS Nano* **2016,** *10* (2), 2485-2490.

51. Merdasa, A.; Tian, Y.; Camacho, R.; Dobrovolsky, A.; Debroye, E.; Unger, E. L.; Hofkens, J.; Sundström, V.; Scheblykin, I. G., "Supertrap" at Work: Extremely Efficient Nonradiative Recombination Channels in MAPbI3 Perovskites Revealed by Luminescence Super-Resolution Imaging and Spectroscopy. *ACS Nano* **2017,** *11* (6), 5391-5404.

52. Gibson, N. A.; Koscher, B. A.; Alivisatos, A. P.; Leone, S. R., Excitation Intensity Dependence of Photoluminescence Blinking in $CsPbBr_3$ Perovskite Nanocrystals. *The Journal of Physical Chemistry C* **2018,** *122* (22), 12106-12113.

53. Freppon, D. J.; Men, L.; Burkhow, S. J.; Petrich, J. W.; Vela, J.; Smith, E. A., Photophysical properties of wavelength-tunable methylammonium lead halide perovskite nanocrystals. *Journal of Materials Chemistry C* **2017,** *5* (1), 118-126.

54. Yuan, G.; Ritchie, C.; Ritter, M.; Murphy, S.; Gómez, D. E.; Mulvaney, P., The Degradation and Blinking of Single $CsPbI_3$ Perovskite Quantum Dots. *The Journal of Physical Chemistry C* **2018,** *122* (25), 13407-13415.

55. Seth, S.; Ahmed, T.; Samanta, A., Photoluminescence Flickering and Blinking of Single $CsPbBr_3$ Perovskite Nanocrystals: Revealing Explicit Carrier Recombination Dynamics. *The journal of physical chemistry letters* **2018,** *9* (24), 7007-7014.

56. Boote, B. W.; Andaraarachchi, H. P.; Rosales, B. A.; Blome-Fernández, R.; Zhu, F.; Reichert, M. D.; Santra, K.; Li, J.; Petrich, J. W.; Vela, J.; Smith, E. A., Unveiling the Photo- and Thermal-Stability of Cesium Lead Halide Perovskite Nanocrystals. *ChemPhysChem* **2019,** *20* (20), 2647-2656.

57. Rainò, G.; Landuyt, A.; Krieg, F.; Bernasconi, C.; Ochsenbein, S. T.; Dirin, D. N.; Bodnarchuk, M. I.; Kovalenko, M. V., Underestimated Effect of a Polymer Matrix on the Light Emission of Single $CsPbBr_3$ Nanocrystals. *Nano Letters* **2019,** *19* (6), 3648-3653.

58. Routzahn, A. L.; Jain, P. K., Single-Nanocrystal Reaction Trajectories Reveal Sharp Cooperative Transitions. *Nano Letters* **2014,** *14* (2), 987-992.

59. Routzahn, A. L.; Jain, P. K., Luminescence Blinking of a Reacting Quantum Dot. *Nano Letters* **2015,** *15* (4), 2504-2509.

60. Brenner, T. M.; Rakita, Y.; Orr, Y.; Klein, E.; Feldman, I.; Elbaum, M.; Cahen, D.; Hodes, G., Conversion of Single Crystalline PbI_2 to $CH_3NH_3PbI_3$: Structural Relations and

Transformation Dynamics. *Chemistry of Materials* **2016,** *28* (18), 6501-6510.

61. Karimata, I.; Kobori, Y.; Tachikawa, T., Direct Observation of Charge Collection at Nanometer-Scale Iodide-Rich Perovskites during Halide Exchange Reaction on $CH_3NH_3PbBr_3$. *The Journal of Physical Chemistry Letters* **2017,** *8* (8), 1724-1728.

62. Yin, B.; Cavin, J.; Wang, D.; Khan, D.; Shen, M.; Laing, C.; Mishra, R.; Sadtler, B., Fluorescence microscopy of single lead bromide nanocrystals reveals sharp transitions during their transformation to methylammonium lead bromide. *Journal of Materials Chemistry C* **2019,** *7* (12), 3486-3495.

63. Wang, D.; Zhang, D.; Sadtler, B., Irreversibility in Anion Exchange Between Cesium Lead Bromide and Iodide Nanocrystals Imaged by Single-Particle Fluorescence. *The Journal of Physical Chemistry C* **2020,** *124* (49), 27158-27168.

64. Yoshimura, H.; Yamauchi, M.; Masuo, S., In Situ Observation of Emission Behavior during Anion-Exchange Reaction of a Cesium Lead Halide Perovskite Nanocrystal at the Single-Nanocrystal Level. *The Journal of Physical Chemistry Letters* **2020,** *11* (2), 530-535.

65. Karimata, I.; Tachikawa, T., In Situ Exploration of the Structural Transition during Morphology- and Efficiency-Conserving Halide Exchange on a Single Perovskite Nanocrystal. *Angewandte Chemie International Edition* **2021,** *60* (5), 2548-2553.

66. Darmawan, Y. A.; Yamauchi, M.; Masuo, S., In Situ Observation of Emission Sites during the Halide Exchange Reaction in Single Cesium Lead Halide Perovskite Nanocrystals. *The Journal of Physical Chemistry C* **2022,** *126* (5), 2627-2633.

67. Dong, Y.; Qiao, T.; Kim, D.; Parobek, D.; Rossi, D.; Son, D. H., Precise control of quantum confinement in cesium lead halide perovskite quantum dots via thermodynamic equilibrium. *Nano letters* **2018,** *18* (6), 3716-3722.

68. Peng, L.; Dutta, A.; Xie, R.; Yang, W.; Pradhan, N., Dot–wire–platelet–cube: step growth and structural transformations in CsPbBr3 perovskite nanocrystals. *ACS Energy Letters* **2018,** *3* (8), 2014-2020.

69. Maes, J.; Balcaen, L.; Drijvers, E.; Zhao, Q.; De Roo, J.; Vantomme, A.; Vanhaecke, F.; Geiregat, P.; Hens, Z., Light Absorption Coefficient of $CsPbBr_3$ Perovskite Nanocrystals. *The Journal of Physical Chemistry Letters* **2018,** *9* (11), 3093-3097.

70. Son, D. H.; Hughes, S. M.; Yin, Y.; Paul Alivisatos, A., Cation Exchange Reactions in Ionic Nanocrystals. *Science* **2004,** *306* (5698), 1009-1012.

Chapter 4: Conclusions and Perspectives

4.1 Conclusions

Using single-particle fluorescence microscopy, we demonstrate that individual $CsPbX_3$ NCs exhibit heterogeneous reactivity during anion exchange, which is averaged out during ensemble measurements. This reaction involves different degrees of structural changes within the NCs, depending on the relative miscibility between the initial and final structures. Specifically, the reaction times during anion exchange of $CsPbBr_3$ NCs to $CsPbI_3$ are longer and exhibit a stronger dependence on the concentration of substitutional halide anions compared to the reverse transformation of $CsPbI_3$ NCs to $CsPbBr_3$. We attribute this difference to the more abrupt change in the structure of $CsPbX_3$ NCs when anion exchange starts from $CsPbI_3$ NCs, relative to when the transformation starts from $CsPbBr_3$ NCs, indicating that the exchange reaction is not reversible.

While the results of **Chapter 2** indicated that $CsPbBr_3$ nanocrystals undergo a smooth transition to $CsPbI_3$, we further investigated size effects during anion exchange of $CsPbBr_3$ NCs to $CsPbI_3$. We observe that smaller NCs (< 8 nm) exhibit longer reaction times which depend more strongly on the concentration of substitutional halide anions compared with larger NCs (> 8 nm). To rationalize this size-dependent chemical reactivity, we propose a mechanism in which size-dependent miscibility controls the reaction kinetics. While smaller NCs maintain a homogenous structure throughout anion exchange, an iodide-rich region with a different structure from $CsPbBr_3$ must nucleate within larger NCs.

The mechanistic insights developed through this research can provide more precise control of post-synthetic anion exchange to reduce the heterogeneities in composition and defects in the crystal structure. Relatively large NCs (> 10 nm) and a high concentration of substitutional anions

surrounding each NC may provide a method to minimize the compositional variations. Furthermore, the study of anion exchange of single $CsPbX_3$ NCs can also provide insights into the mechanism of other chemical reactions in NCs. For example, lead halide NCs are sensitive to water and will degrade fast if exposed to moisture. The relationship between the degradation rate and humidity could be studied by quantitively measuring emission intensity and blinking statistics with the technique of single-particle fluorescence imaging.

4.2 Perspectives

We observe the asymmetric reactivity during anion exchange of $CsPbI_3$ NCs to $CsPbBr_3$ compared with that of $CsPbBr_3$ NCs to $CsPbI_3$. We also find the chemical reactivity of anion exchange from $CsPbBr_3$ NCs to $CsPbI_3$ is size-dependent. A logical extension of the work described in this dissertation will be to study the size dependence of the transformation of $CsPbI_3$ NCs to $CsPbBr_3$. Since the cubic phase of $CsPbI_3$ NCs is more stable at smaller sizes, smaller $CsPbI_3$ NCs may undergo different degrees of structural change compared to the larger $CsPbI_3$ NCs. With the results of this future work, we may have a clear understanding of how the structure changes step by step during anion exchange between $CsPbBr_3$ and $CsPbI_3$ NCs. Furthermore, while surface strain and phase stability are size dependent in $CsPbX_3$ NCs, how size affects defects within NCs is not clear. As the fraction of on and off states during single-particle fluorescence imaging reflects the concentration of defects, single-particle imaging provide a method to study the size dependence of defects by analyzing blinking statistics of single NCs.

Currently, the reagent used for halide substitution must be non-polar, so it is compatible with a non-polar solvent (e.g., hexane) used to disperse the $CsPbX_3$ NCs during anion exchange. Especially for smaller NCs (< 8 nm), a reagent for anion substitution with large steric hindrance (e.g., a long-chain group connected to halide anion) may cause collapse of NC structure, as it induces a lot of surface strain when halide anions intercalate NCs. More suitable reagents to induce anion exchange with less degradation at mild conditions are desired in future research.

Synthetic methods to achieve a narrow size distribution of NCs still have a long way to go. The synthesis of $CsPbX_3$ NCs via the hydrothermal method or co-precipitation method involves rapid crystal growth, which makes the control of size distribution more difficult. Proper ligands, relatively low temperature and single-phase reaction may be possible factors leading to better

control of size distribution during synthesis.[1-3] Additionally, smaller $CsPbX_3$ NCs are less stable during storage. Even the application of large $CsPbX_3$ NCs is limited by the stability problem. Thus, new methodologies to stabilize $CsPbX_3$ NCs are desired. My colleague Dr. Dong Wang and I studied the feasibility of the protecting $CsPbBr_3$ NCs by coating them with a silicon dioxide (SiO_2) shell. While SiO_2 shells show a possible solution to improve the thermostability of $CsPbBr_3$ NCs, we need more work to figure out if they can stabilize the cores during chemical reactions. Our ultimate goal is to reduce inhomogeneities in $CsPbX_3$ NCs and enhance the performance of this light emitting material with high color purity and a long lifetime.

4.3 References

1. Dirin, D. N.; Cherniukh, I.; Yakunin, S.; Shynkarenko, Y.; Kovalenko, M. V., Solution-grown $CsPbBr_3$ perovskite single crystals for photon detection. *Chemistry of Materials* **2016,** *28* (23), 8470-8474.

2. Akkerman, Q. A.; Nguyen, T. P.; Boehme, S. C.; Montanarella, F.; Dirin, D. N.; Wechsler, P.; Beiglböck, F.; Rainò, G.; Erni, R.; Katan, C., Controlling the nucleation and growth kinetics of lead halide perovskite quantum dots. *Science* **2022,** *377* (6613), 1406-1412.

3. Montanarella, F.; Akkerman, Q. A.; Bonatz, D.; van der Sluijs, M. M.; van der Bok, J. C.; Prins, P. T.; Aebli, M.; Mews, A.; Vanmaekelbergh, D.; Kovalenko, M. V., Growth and Self-Assembly of $CsPbBr_3$ Nanocrystals in the TOPO/$PbBr_2$ Synthesis as Seen with X-ray Scattering. *Nano Letters* **2023**.